Equilibrium and Stability of Brillouin Flow in Planar, Conventional, and Inverted Magnetrons

by

David Henry Simon

A dissertation submitted in partial fulfillment
of the requirements for the degree of
Doctor of Philosophy
(Nuclear Engineering and Radiological Sciences)
in the University of Michigan
2016

Doctoral Committee:

Professor Yue Y. Lau, Chair
Professor John E. Foster
Professor Ronald M. Gilgenbach
Professor Mark J. Kushner

ACKNOWLEDGEMENTS

My time in graduate school has been shaped by the department, the places I interned, my friends, and my family, without all of whom, this thesis would not have been possible. The department as a whole has been very supportive, providing me with engaging classes, guidance toward graduation, and, occasionally, free food. Professor Lau has guided not just my graduate studies, but my whole approach to science. Even the happy hours were informative! Professor Gilgenbach provided experimental knowledge that brought the theories into the physical realm. There's simply no substitute for spending time in the lab. As a TA for Professor Foster, I gained some insight into what it would be like to teach, and a new appreciation for some of the finer points of experimental plasma physics. The MIPSE seminars that Professor Kushner has provided have always been a great source of knowledge about the whole field of plasmas (and of snacks). Thank you to everyone involved.

I had internships at L-3, AFRL, and NRL during my time in grad school. I learned so much as these internships and met so many great people. I want to thank everybody, especially my supervisors and fellow interns, for the experiences I had at these places and the knowledge I gained. I also need to thank Professor Lau again, for setting up each of the internships.

For all my friends, thank you for the nights out, the tailgates, the board games, and everything else. You're a large part of why I've enjoyed my time in grad school so much. A special thanks to my travel partners, we had so many unique experiences!

I would like to thank my parents for their encouragement and love, which is of course not limited to my time in grad school, but has held true every day of my life. I look forward to the talks we have, even if I haven't always shown it. I appreciate all the advice, especially when I call out of the blue. I always look forward to the care packages. I don't think I've told you this, but the food gets eaten within a day or two, tops. Anyway, thank you both, for everything.

This thesis work was supported by Air Force Office of Scientific Research Awards No. FA9550-10-1-0104, FA9550-15-1-0097, Office of Naval Research Award No. N00014-13-1-0566, and L-3 Communications Electron Device Division.

TABLE OF CONTENTS

TABLE OF FIGURES

LIST OF ACRONYMS

AK gap	Anode-cathode gap
B-H	Buneman-Hartree
BHL	Buneman-Hartree-like
CFA	Crossed-field amplifiers
DC	Direct current
HCL	Hull Cutoff-like
KH	Kelvin-Helmholtz
MELBA	Michigan Electron Long Beam Accelerator
PIC	Particle-in-cell
RF	Radio frequency
RPM	Recirculating Planar Magnetron
SLC	Space-charge limit
SWS	Slow-wave structure
UM	University of Michigan

LIST OF SYMBOLS

A	Vector potential
B	Magnetic field
c	Speed of light in a vacuum
$D, (D^*)$	Anode-cathode gap separation (normalized)
e	Charge of an electron
E	Electric field
h	Ratio of electric force to centripetal force for a rotating electron beam
k	Wavenumber in radians per meter
l	Azimuthal mode number
m_0, m	Rest mass of an electron, mass of non-relativistic electron
m_{eff}	Effective mass for electrons within a rotating electron beam
n	Electron density
q	Ratio of plasma frequency to cyclotron frequency
r_b, x_b	Coordinates of top of Brillouin hub for cylindrical, Cartesian
v	velocity
V	Voltage
β	Velocity divided by speed of light
γ	Relativistic mass factor
κ	Proportional to electron density at the cathode
ϕ	Scalar electric potential (up to Section 3.4). Proportional to perturbation electric field parallel to equilibrium electron velocity (from Section 3.4 on).
ω	Frequency in radians per second
ω_c	Non-relativistic electron cyclotron frequency
ω_p	Non-relativistic electron plasma frequency

ABSTRACT

The Brillouin flow is considered to be the prevalent state in many electron devices that operate with a crossed electric and magnetic field, including magnetrons. An investigation of equilibrium and stability of the Brillouin flow is undertaken in this thesis, motivated by simulations of the novel magnetron device, the Recirculating Planar Magnetron (RPM). These simulations showed faster startup in the inverted configuration (cathode on outside, anode on inside) when compared to the conventional configuration (cathode on inside, anode on outside). This thesis first examines the equilibrium properties of the Brillouin flow for both planar and cylindrical geometries, and discovers new relations between the vector potential, scalar potential and electron velocity that mirror the Buneman-Hartree (B-H) and Hull Cutoff conditions. Additionally, the difference in the B-H condition in cylindrical magnetrons between the single particle orbit model and the Brillouin flow model is also discovered. The B-H condition derived from the Brillouin flow model shows a better match to simulation and experiment of relativistic magnetrons than the single particle model B-H condition.

The stability of the equilibrium Brillouin flow is next studied by perturbation analysis. The perturbation fields are matched to the vacuum field solution to find the complex eigenvalue frequency. The first focus is on smooth-bore magnetrons. Analysis of a planar magnetron recovers the familiar diocotron-like instability growth. The Brillouin flow instability growth rate is found, for the first time, to be enhanced in the inverted cylindrical magnetron and decreased in the conventional cylindrical magnetron, relative to the planar magnetron. This shows that the negative mass effect on a thin electron beam in a cylindrical crossed-field device is not eliminated by the significant intrinsic velocity spread associated with the velocity shear in the Brillouin flow. A slow-wave structure (SWS) is then added to the anode, which introduces a resonance between the wave on the slow-wave circuit and electrons. The space harmonics in the vacuum electromagnetic fields and within the flow are included in the analysis, also for the first time. The result is that the real part of the eigenvalue frequency closely matches the cold tube circuit frequency. The growth

of the instability is slightly higher for the conventional magnetron, compared to the inverted magnetron, unlike the smooth-bore anode. The resonant instability appears to be dominant over the negative mass instability when a SWS is added to the anode.

CHAPTER 1

Introduction

1.1 Overview of magnetrons

Radio wave detection of vehicles, commonly known as radar, arose as a military concept in the 1930s [1]. Radar was initially implemented using linear beam devices, such as klystrons, which were limited in current by the need to focus an electron beam down a drift tube [2]. A crossed-field device, which operates with an electric field and magnetic field orthogonal to each other, such as the split-anode magnetron in the early days, did not require this precision focusing. However, it suffered from low efficiency and power [3], [4]. Research focused on merging the desirable properties of the magnetron and the klystron led to the development of the cavity magnetron shortly before the outbreak of World War II. This device produced significantly more power than its contemporary competitors, and was quickly incorporated into radar systems for the war [2]. Magnetrons have been a staple of microwave production ever since.

At its most basic, the magnetron is a highly efficient vacuum electronic device that converts potential energy into radio frequency (RF) energy. In practice, it is considerably more complex. Magnetrons are much more difficult to analyze than linear beam devices, which utilize a well-characterized injected beam [5], [6]. One of the fundamental difficulties in analyzing magnetrons is that the cathode is part of the interaction circuit. The electron orbits in the interaction region cannot be well characterized due to presence of other electrons in the interaction region, which have a highly irregular space charge distribution. In contrast, the electron beam in linear beam devices such as klystrons and traveling wave tubes can be analyzed with or without the effects of space charge, to a high degree of accuracy. Magnetrons typically operate in the space-charge limited regime, where electron orbits show strong positional dependence in their velocity. The multitude of velocities in the electrons that exist within the magnetron interaction region gives rise to the ability to produce RF power at multiple modes based on the interaction circuit. As if that

were not enough, much work on magnetrons and their close relatives, the crossed-field amplifiers, is done by commercial entities or the military, making open, public literature scarce.

Despite the hurdles in their analysis, magnetrons are widely used. The initial properties that made magnetrons the focus of research in the 1940s, namely high power and high efficiency, continue to hold true today [7]. Radar detection for national defense is a major application of magnetrons. The high efficiency of non-relativistic magnetrons, whose operating voltage is far lower than the relativistic regime, has led to consumer use as well. The magnetron within the household microwave oven operates at ~70% efficiency [7]. In the industrial scale, large magnetron microwaves pre-cook foods like bacon at an even higher efficiency, almost 90% [7]. Magnetrons are always an option for microwave production for anything requiring RF power, such as weather radar, medical devices, plasma processing, and non-intrusive scanning. The usage of a magnetron over other vacuum electronics or solid state devices depends on factors like cost, weight, efficiency and required power.

1.1.1 Basic Operation of Magnetrons

The process for conversion of direct current (DC) power into RF power can be visualized using a single electron. The electron is emitted from the cathode of a magnetron and accelerated toward the anode due to the applied potential between the anode and cathode as shown in Figure 1.1. The region between the anode and cathode is called the AK gap. The external magnetic field B_0, pointing out of the plane of the paper, deflects the electron and prevents it from reaching the anode. This process is referred to as magnetic insulation. The condition for magnetic insulation is called the Hull cutoff condition. There are two models for electron motion in crossed electric and magnetic fields in the limit that electrons are emitted until the electric field at the cathode is zero (the space-charge limit). The first is the single particle orbit model, in which an electron executes a cycloidal orbit as shown in Figure 1.1. It is also known as the "multi-stream" model because of the crossing of cycloidal orbits, and will be used for this section. The second is the Brillouin flow model, which is a laminar shear flow without orbital crossing. It is also called the "single-stream" model. Both will be discussed in more detail in Section 1.2.

In Figure 1.1, the magnetron has not started to produce RF so it is said to be non-oscillating. Magnetrons may operate as microwave oscillators which produce RF at a specific frequency without any external signal. In the non-oscillating magnetron (Figure 1.1), the electron executes cycloidal orbits due to the crossed electric and magnetic fields, without any perturbation due to the

RF fields. The transition from a non-oscillating state to an oscillating state is known as startup, a process that is still not fully understood to this day. This thesis in part addresses this problem.

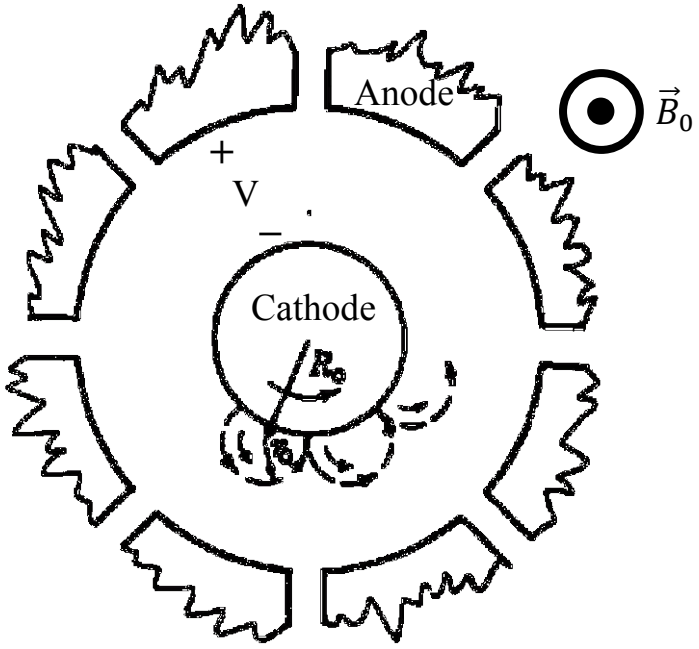

Figure 1.1: An electron in a non-oscillating magnetron, demonstrating magnetic insulation [8].

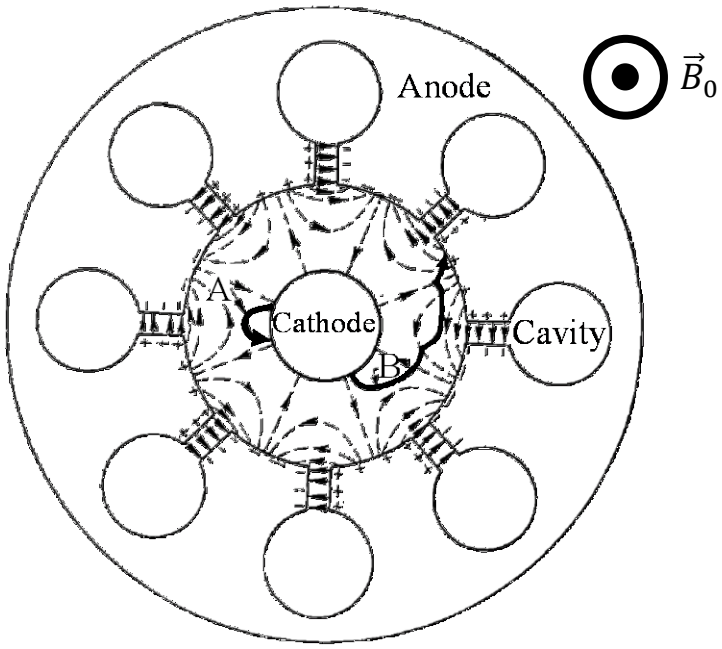

Figure 1.2: Two test electrons, A and B, in an oscillating magnetron, demonstrating synchronous interaction [8]. The RF electric field is shown as dashed lines.

Figure 1.2 shows an oscillating magnetron, with the electric field of the RF shown as dashed lines with arrows to indicate direction. The eight cavities in the diagram each support a

mode. They communicate with each other by means of a propagating wave along the anode. The phase advance of the RF electric field from one cavity to another (in radians) is used to designate the operating mode. Figure 1.2 shows the π-mode where the phase of the RF field advances by π per cavity. The azimuthal mode number is the number of 2π phase shifts, or RF wavelengths, that occur across the anode. For π-mode, the azimuthal mode number is the number of cavities divided by 2, which is 4 in the example here. The purpose of the cavities is to slow down the phase velocity of the RF wave, so that it can be matched to the velocity of the electrons in the magnetron to ensure continuous synchronous interaction between the electrons and the circuit wave. A structure that results in a slower RF phase velocity is a slow-wave structure (SWS), while the absence of a SWS is referred to as a smooth-bore anode. The matching of velocities results in synchronous interaction between the electron and the RF, which is known as the Buneman-Hartree (B-H) condition.

Two electrons are shown in Figure 1.2. Electron B is synchronous with the favorable phase of the slowed RF wave. This electron is slowed by the electric field of the RF, which transfers energy from the electron to the RF wave. The decrease in velocity also decreases the Lorentz force, and electron B is unable to return to the cathode. The electron and the RF are co-moving, so the process continues until the electron reaches the anode, which will occur despite magnetic insulation (in the DC state). By the time electron B reaches the anode, the difference between the applied potential energy and the electron's final kinetic energy has been transferred to the RF. Electron A in the unfavorable phase of the RF wave. It is accelerated by the RF electric field, which results in increased velocity. The Lorentz force increases, and electron A is returned to the cathode. Overall, the electrons that would take energy from the RF (electron A) are quickly removed, while electrons that would give energy to the RF (electron B) remain in the system for longer, leading to a net gain of RF energy from the initially applied DC voltage. Since electrons like A, which are in the (unfavorable) accelerating phase of the RF electric field, are removed, electron spokes are formed in every other cavity for the π-mode. A simulation of an oscillating magnetron in the π-mode is shown in Figure 1.3, where spokes in every other cavity can be seen. This simulation was performed using MAGIC, which is a fully electromagnetic particle-in-cell (PIC) finite-difference, time-domain code.

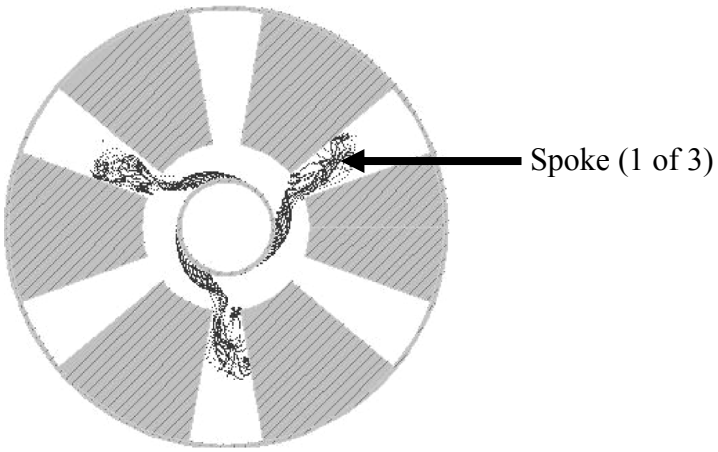

Figure 1.3: 2D simulation of oscillating magnetron in the π-mode of a 6-cavity magnetron, performed using MAGIC particle-in-cell (PIC) code [9]. Note the irregularities of an electron orbit.

In addition to producing microwaves from oscillation, the basic design of a magnetron also lends itself to amplifying an external signal. These devices are known as crossed-field amplifiers (CFAs), the first of which was a modified magnetron [7]. CFAs tend to have low gain, usually not more than 15 dB, which is low compared with traveling wave tube amplifiers and klystron amplifiers, but they retain the high efficiency and high power characteristic of magnetrons [10].

1.1.2 Types of Magnetrons

The magnetrons shown in Figure 1.1 through Figure 1.3 are conventional magnetrons. The convention, followed by the vast majority of magnetrons, is that the cathode is in the center of the device and the anode is on the outside, as shown in Figure 1.4a. A few of the many reasons that this geometry is the convention are as follows. This design places the grounded anode on the outside, instead of the negatively biased cathode. For thermionic cathodes, which operate at very high temperatures, the cathode is smaller and easier to heat, in addition to being shielded from the rest of the assembly by the anode. External cooling of the anode is also more readily achieved due to the large anode volume and ease of access. Extraction of RF happens at the cavities, which are more accessible with the anode on the outside.

The inverted magnetron (Figure 1.4b) has the cathode on the outside and the anode in the center, in an inversion of the conventional magnetron design and is thus named. This design allows for higher current, due to the larger cathode area. It also requires less magnetic field for magnetic insulation, since the centrifugal force aids in returning electrons to the cathode. The planar magnetron is shown in Figure 1.4c. This design lacks the recirculation of electrons that can make

the cylindrical devices efficient. For all geometries, there is an external magnetic field and an applied voltage between the anode and cathode, as shown by the electric field. Virtually all deployed magnetrons are in the conventional magnetron configuration (Figure 1.4a).

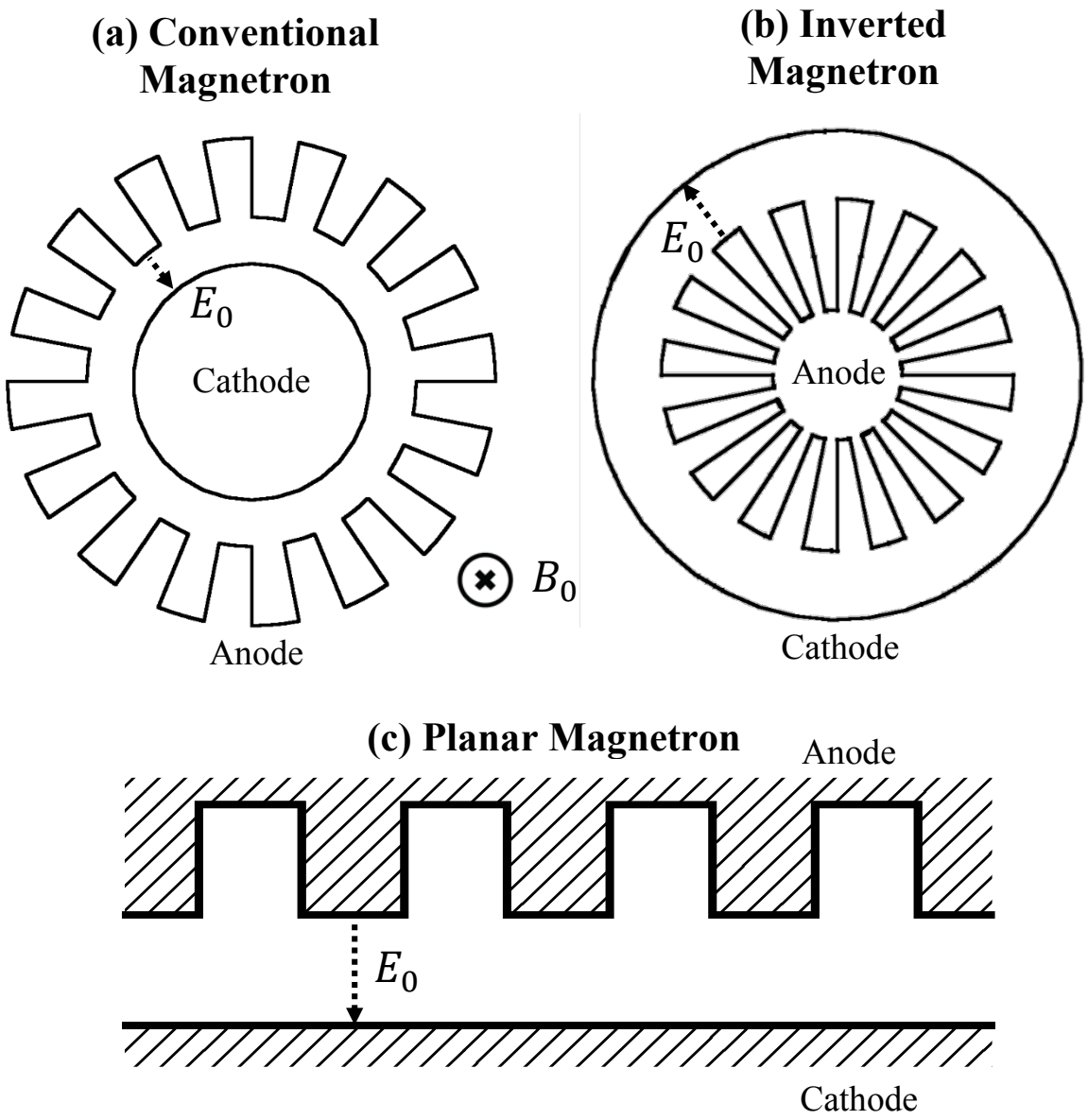

Figure 1.4: The geometry of (a) conventional magnetron, (b) inverted magnetron, and (c) planar magnetron. All include a slow-wave structure on the anode.

A new device, the recirculating planar magnetron (RPM) has been recently conceived, designed, and tested at the University of Michigan [11]–[14]. This device consists of two planar magnetron sections joined together by cylindrical drift regions as shown and labeled in Figure 1.5.

The RPM has two major advantages over traditional magnetrons. It has a much larger cathode surface area, allowing for higher current and better thermal management. The volume of the device increases linearly with the number of cavities, instead of to the squared power in conventional magnetrons, reducing the magnetic field requirement [11], [14]. Work is also underway at UM to make a CFA based on the RPM design [15], [16].

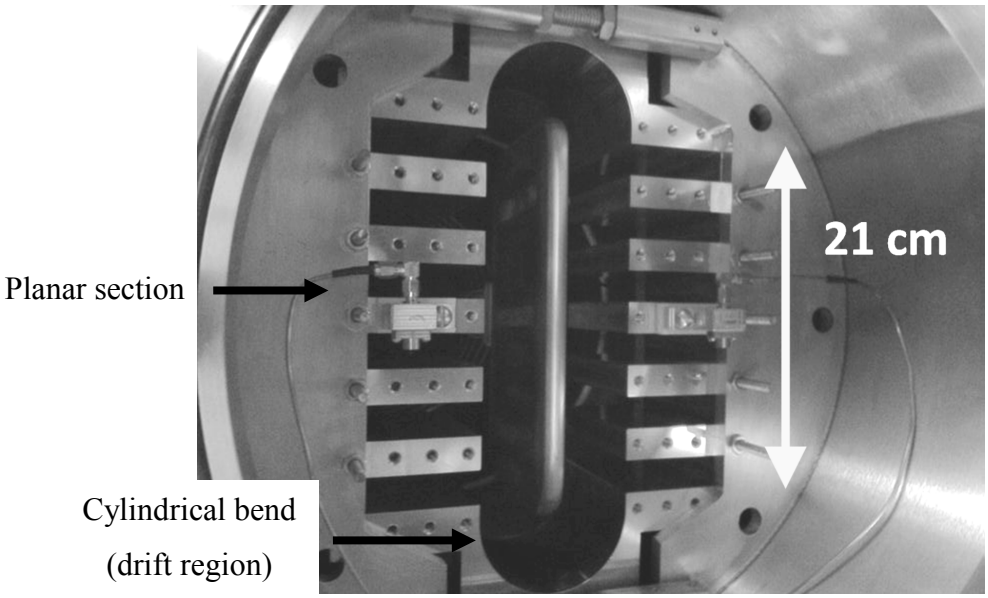

Figure 1.5: The recirculating planar magnetron prototype (RPM-12a) at the University of Michigan [14]

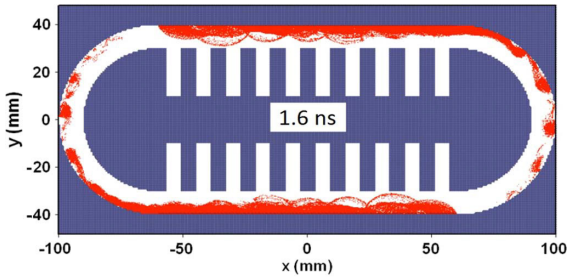

Figure 1.6: PIC simulation of the RPM in the inverted configuration performed using MAGIC (PIC code) [12]

Early simulations of the RPM were performed with both conventional magnetron (cathode on the inside, anode on the outside) and inverted magnetron (anode on the inside, cathode on the outside) configurations, using the PIC code MAGIC. Faster magnetron startup was observed for the inverted configuration, which exhibited distinct bunching in the cylindrical sections very early in simulation time as shown in Figure 1.6 [11], [12]. The negative mass effect, which will be discussed in Section 1.3, was identified as a possible source of instability that could lead to faster

startup. To date there has been no existing literature on the negative mass effect in cylindrical Brillouin flow (discussed in Section 1.2.2), which is a laminar shear electron flow with no orbital crossing, and is considered as the prevalent flow in crossed-field devices [17], [18]. This prompted the research that forms the basis for this thesis. Contained herein is a comprehensive analysis of the steady state equilibria and their small signal instabilities in the Brillouin flow for conventional, inverted and planar geometry with both smooth-bore and slow-wave structure anodes.

1.2 Electron motion in a crossed-field device

Electron motion in a crossed-field device is traditionally described by one of two basic models of orbits. The first is a "multi-stream model" where electrons undergo cycloidal orbits (which cross each other). The second is the "single stream model" where the electrons form a laminar flow, known as Brillouin flow. The model that is closest to the motion of electrons within real, physical crossed-field devices has been a source of controversy for many years [5], which still yields new, unexpected results as shown in this thesis.

1.2.1 Single particle cycloidal orbit

In the absence of space charge, individual electrons will undergo cycloidal orbits in crossed-field devices as long as the applied magnetic field is large enough to insulate them from the anode (Figure 1.7). These orbits provide basic information about the operation of magnetrons, which will be discussed in section 1.2.3.

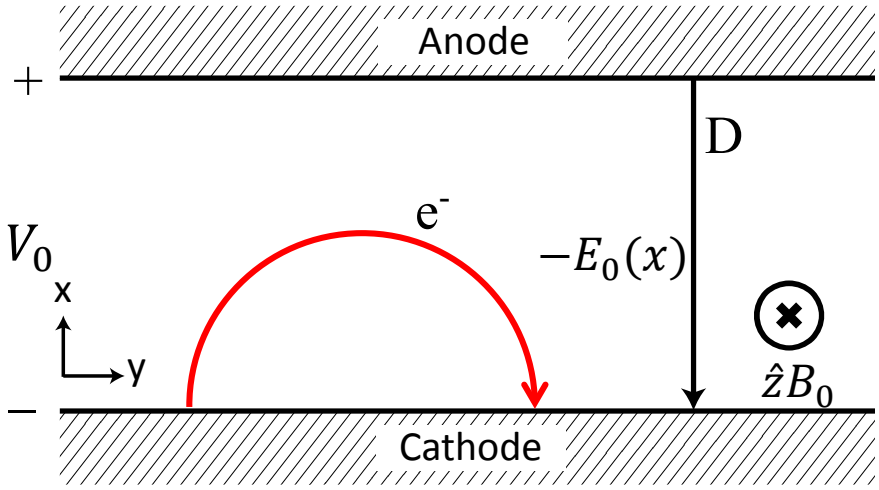

Figure 1.7: Diagram of single particle orbit in a crossed-field device.

An electron emitted from the cathode is accelerated toward the anode by electric field due to the applied voltage differential between the anode and cathode. The electron velocity is

perpendicular to the constant external magnetic field, $\hat{z}B_0$, so the Lorentz force also acts upon the electron. The result is a cycloidal orbit, shown in red in Figure 1.7, where V_0 is the applied voltage, E_0 is the electric field due to V_0, B_0 is the external magnetic field, and D is the distance between the anode and cathode (AK gap width). In a non-relativistic description, the electron motion is described in general by the Lorentz force equation, broken into $\hat{x}$ and $\hat{y}$ components,

$$m\frac{\partial v_y}{\partial t} = e[v_x B_0], \tag{1.1}$$

$$m\frac{\partial v_x}{\partial t} = -e\left[E_0 + v_y B_0\right], \tag{1.2}$$

where e is the magnitude of the charge on one electron, and m is the electron mass. In the case pictured in Figure 1.7, and for all magnetrons analyzed in this thesis, the electrons emitted from the cathode are assumed to have no initial kinetic energy because the energy of the electrons due to the applied DC potential is much greater than the initial electron energy that results from emission (such as thermal). With this assumption, we can start the electrons at $x = 0$ and $y = 0$ at $t = 0$ and find their position as a function of time,

$$y(t) = \frac{E_0}{\omega_c B_0}[\sin(\omega_c t) - \omega_c t], \tag{1.3}$$

$$x(t) = \frac{E_0}{\omega_c B_0}[\cos(\omega_c t) - 1], \tag{1.4}$$

where $\omega_c = eB_0/m$ is the electron cyclotron frequency and E_0 is negative (Figure 1.7). These equations show that an electron emitted from the cathode will return to the cathode (if it does not reach the anode) with a period of $T = 2\pi/\omega_c$ seconds. The average velocity over one period for the electron in the $\hat{y}$ direction is simply $\langle v_y \rangle = |E_0|/B_0$, the $E \times B$ drift velocity.

1.2.2 Brillouin flow

Brillouin flow is a laminar electron flow, shown schematically in Figure 1.8. The region of Brillouin flow within a magnetron is referred to as the Brillouin hub, extending from the cathode to a "hub height," x_b. Electrons within the Brillouin hub are assumed to be traveling parallel to the cathode. The electrons are emitted from the cathode with zero net energy, which is assumed to be true for all electrons in the Brillouin flow. These two requirements, along with the space-charge limited nature of the flow (electric field goes to zero on the cathode surface), are sufficient to determine all of its properties. In Figure 1.8 W is the height of the vacuum region (no electrons present), beyond the Brillouin hub.

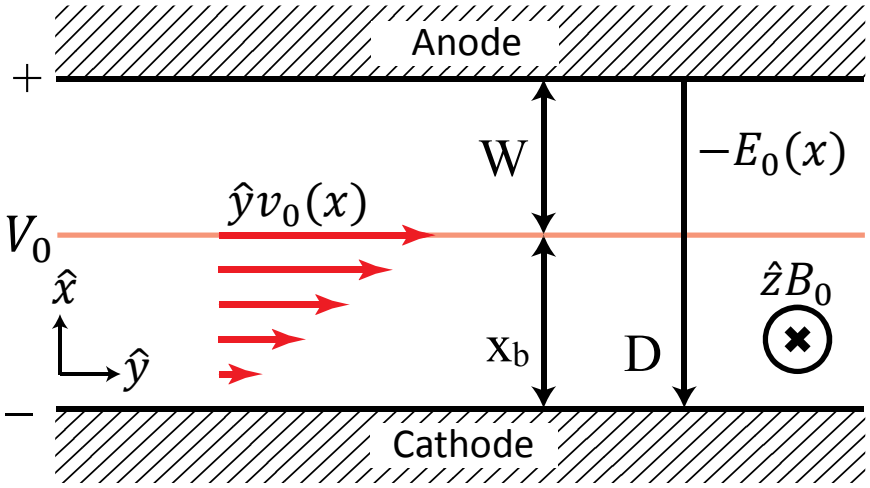

Figure 1.8: Diagram of Brillouin flow in a crossed-field device

Brillouin flow is an equilibrium steady state, so there is no net force on any electron. For non-relativistic flow, in which the self-magnetic field is negligible, the Lorentz force equations simply becomes

$$v_y(x) = -E_0(x)/B_0. \tag{1.5}$$

The conservation of energy equation gives,

$$\frac{1}{2}mv_y^2 = e\phi(x), \tag{1.6}$$

where $\partial\phi(x)/\partial x = -E_0$. Gauss's law is used, where n_0 is the electron density and ϵ_0 is the permittivity of free space,

$$\frac{\partial E_0}{\partial x} = -\frac{en_0}{\epsilon_0}. \tag{1.7}$$

These equations can be solved to yield the Brillouin flow solutions,

$$\omega_p^2 = \omega_c^2, \qquad v_y(x) = \omega_c x, \qquad x_b = D\left(1 - \sqrt{1 - 2V_0/\omega_c B_0 D^2}\right). \tag{1.8a,b,c}$$

The plasma frequency (for the non-neutral Brillouin flow) is defined as $\omega_p^2 = e^2 n_0/\epsilon_0 m$. From Eq. (1.8b), we can see that velocity increases linearly throughout the Brillouin hub, and that density is constant, determined solely by the external magnetic field by Eq. (1.8a). Thus, once B_0, V_0, and D are fixed, the Brillouin flow is completely specified: the electron density is given by Eq. (1.8a), the velocity profile by Eq. (1.8b), and the spatial extent of the Brillouin hub x_b by Eq. (1.8c). Chapter 2 of this thesis contains a more comprehensive derivation of the planar Brillouin flow and the cylindrical Brillouin flow, including fully relativistic treatment.

The relationship between the cycloidal orbit model and the Brillouin flow model was examined by Slater [17] in the space-charge limited regime, where the cathode surface electric field is zero. These cycloidal orbits are known as Slater orbits and they have multiple forms. When an electron released from the cathode executes N cycloidal hops in its journey to the maximum excursion (when not hitting the anode) before returning to the cathode, this orbit is called the N^{th} Slater orbit (N = 1, 2, 3…). At the top of each cycloidal hop, virtually all the electron's velocity is tangent to the cathode. All N^{th} order Slater orbits reach the same maximum excursion into the AK gap, and the N = 1 Slater orbit resembles that shown in Figure 1.7. The Brillouin flow is the collection of N^{th} Slater orbits with $N \rightarrow \infty$. Slater also made the important and far-sighted claim (before any particle-in-cell simulations) that the most likely state in space-charge limited crossed-field flows is the Brillouin flow, corresponding to $N \rightarrow \infty$, in which the electrons have only velocity tangential to the cathode.

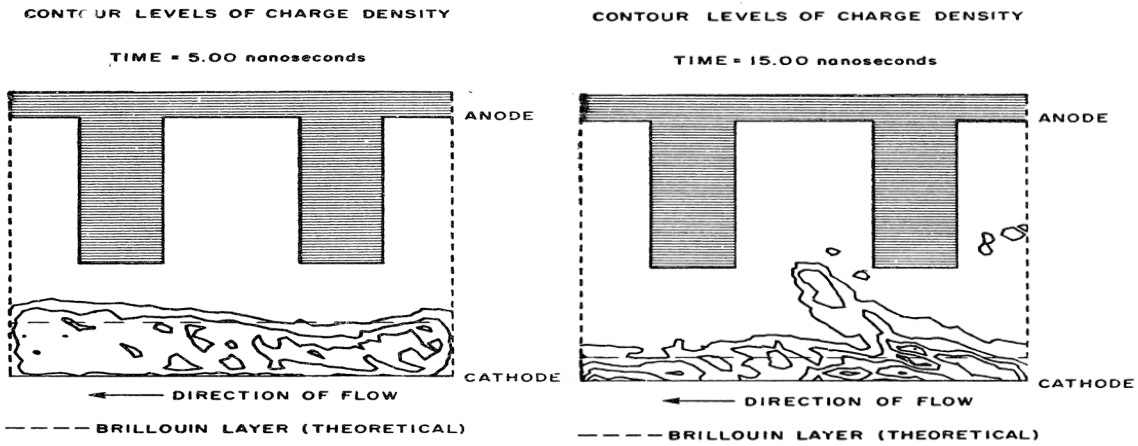

Figure 1.9: The first particle-in-cell simulation results of a magnetron [19], [20]. Brillouin flow is demonstrated at the early time on the left, spoke formation is shown at the later time on the right.

Palevski's magnetron simulation work, using a particle-in-cell (PIC) code, [19], [20] , shown in Figure 1.9, was the first to demonstrate that the Brillouin flow was the preferred state for electrons. The image on the left shows a relatively constant density at 5ns, which corresponds to Brillouin flow in an equilibrium state. The image on the right shows bunching and spoke formation at 15ns. Spokes consist of electrons that are in phase and synchronous with the RF. The electrons within the spoke reach the anode and give up energy to the RF (the same mechanism illustrated by electron B in Figure 1.2). Christenson further showed that, in simulation, the cycloidal orbits would collapse from a small resistivity in the external circuit or a minute AC perturbation on the DC

applied voltage [18], [21], [22]. The resulting electrons were deemed to be in a near-Brillouin state; Brillouin flow with a mild turbulent background superimposed.

1.2.3 Operating conditions for magnetrons

Magnetrons require two conditions to operate [7], [17]. The first is magnetic insulation, meaning that the electrons emitted from the cathode are turned back by the magnetic field before they reach the anode (the electron in Figure 1.7 is magnetically insulated). The relation between the magnetic field and voltage at which electrons just graze the anode is called the Hull cutoff condition [23]. The second condition is synchronism of the electron velocity and the RF phase velocity of the circuit mode, which was described in Section 1.1.1. The electrons must be able to interact with the RF wave in order to give up energy to it. The operating parameters at which synchronism starts to occur are known as the Buneman-Hartree condition [17], [24].

For both planar and cylindrical geometry, the Hull cutoff and Buneman-Hartree condition are most easily visualized in normalized units,

$$\bar{V} = \frac{eV}{mc^2}, \qquad \bar{B} = \frac{eBD^*}{mc}, \qquad D^* = \frac{|r_a^2 - r_c^2|}{2r_a}, \qquad \beta = \frac{v_{ph}}{c}, \tag{1.9}$$

where m is the rest mass of electrons, c is the speed of light in a vacuum, D^* is the normalized AK gap separation, r_c is the cathode radius, r_a is the anode radius, and v_{ph} is the RF circuit phase velocity at the anode. The planar limit is obtained by letting $r_a \to \infty, r_c \to \infty$ but $|r_a - r_c| = D$ is a constant, and D^* becomes D, the AK gap separation. In these units, the single particle Hull cutoff for both planar and cylindrical geometry is given by, in the relativistically correct theory [25],

$$\bar{B} = (2\bar{V} + \bar{V}^2)^{\frac{1}{2}}. \tag{1.10}$$

The Hull cutoff expresses the required normalized magnetic field in terms of the applied voltage. The single particle Buneman-Hartree condition is, in the relativistically correct theory [25],

$$\bar{V} = \bar{B}\beta - 1 + (1 - \beta^2)^{\frac{1}{2}}. \tag{1.11}$$

The Buneman-Hartree condition depends on the mode of magnetron operation, which has a normalized RF circuit velocity β at the anode. Both these conditions are shown in Figure 1.10. The Hull cutoff is the upper line, the Buneman-Hartree condition is the lower line, and the region between them is where magnetrons operate. The Buneman-Hartree curve in Figure 1.10 is a straight line, always tangent to the Hull cutoff curve. The point of tangency is $(\bar{B}, \bar{V}) = (\beta\gamma, \gamma - 1)$

where $\gamma = (1-\beta^2)^{-1/2}$ [25]. Note that Figure 1.10 applies to all operating modes of a magnetron. Different operating modes will have different normalized circuit velocity β.

The above results are obtained by the single particle orbit model (Figure 1.7). For the Brillouin flow model, the Hull cutoff condition is $x_b = D$, i.e. the Brillouin hub just barely touches the anode surface. The Buneman-Hartree condition becomes $v_0(x_b) = v_{ph}$, i.e., the circuit wave's phase velocity and the electron flow velocity are synchronized at the top of the Brillouin hub.

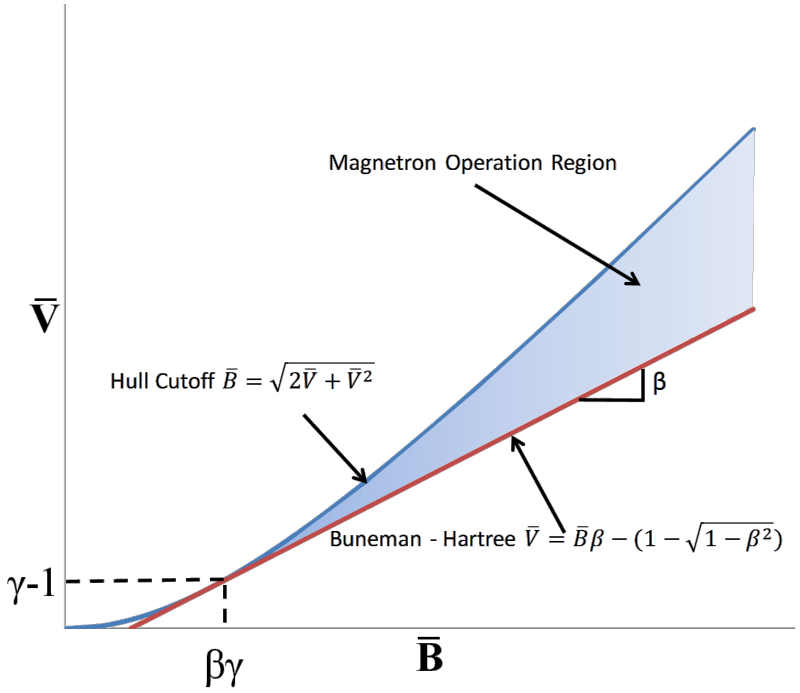

Figure 1.10: The Hull cutoff, Buneman-Hartree condition, and magnetron operation region according to the single particle orbit model, in normalized units.

In the planar geometry, both the single particle orbit and Brillouin models yield the same Hull cutoff and Buneman-Hartree conditions. The Hull cutoff remains the same for the two models for cylindrical geometries as well. For the Buneman-Hartree condition, the Brillouin flow model produces a different parameter space of operation than the single particle model for the cylindrical magnetrons [25]. In the Brillouin flow model, conventional magnetrons show a larger parameter space of operation and inverted magnetrons show a more restricted parameter space of operations when compared to the single particle orbit model, whose geometry effect is minimal (Figure 1.10). This effect will be covered in detail in the latter half of Chapter 2, where it is shown to provide an interpretation of anomalies observed in experiments and simulations on relativistic magnetrons.

1.3 Prior studies of instabilities in crossed-field devices

The stability of crossed-field flows has been studied extensively. It has also been compared with electron beam instabilities in other vacuum electronic devices such as the gyrotron and orbitron and particle accelerators such as the cyclotron and synchrotron. The investigation of instabilities has been a fundamental part of crossed-field research as they are closely related to electron crossed-field transport in general and to the starting mechanism for the magnetron oscillator in particular. Many of the studies were restricted to the planar geometry in which the important "negative mass effect" described in Section 1.3.2 below is absent. The stability of cylindrical Brillouin flow was rather insufficiently studied and this thesis focuses on this task.

This section reviews the two basic instabilities in crossed-field flows, the diocotron instability [26]–[28] and the negative mass instability [29], [30]. The negative mass instability is also known as the cyclotron maser instability in the presence of synchronous interaction with a waveguide mode [5]. Both types can be accounted for by the same small signal theory, although the physical mechanisms behind them are quite different [31]. The diocotron instability has been previously shown in planar Brillouin flow, while this thesis will show the negative mass effect in cylindrical Brillouin flow, including the important effects of the slow-wave structure.

1.3.1 Diocotron instability

The diocotron instability is one of the most prevalent instabilities in non-neutral plasmas, and was the first to be discovered from early magnetron research. The diocotron instability has long been considered as the mechanism for magnetron startup (i.e., from the non-oscillating state to full oscillation which generates RF), and as a possible cause for magnetron noise. It dominates in low density and low voltage situations, but can be stabilized by relativistic effects [32]. The diocotron instability is caused by DC space charge. The self-fields of electrons within an equilibrium electron flow cause a velocity gradient in the $E \times B$ drift. This velocity gradient, or shear, is a fundamental characteristic of the diocotron instability. For this reason, it has been compared to the Kelvin-Helmholtz instability in hydrodynamics [33]. An analysis of a thin, but finite, electron beam in equilibrium $E \times B$ drift will show that the diocotron and Kelvin-Helmholtz instabilities (KH) have the same growth rate, as follows.

The growth rate ω_i for KH in a thin sheet across which there is a flow velocity difference of Δv is given by [5], [33]

$$\omega_i = \frac{1}{2} k \Delta v, \tag{1.12}$$

where k is the wavenumber in the direction of the flow. In equilibrium, the $E \times B$ drift velocity of an electron in an electron sheet is simply E/B. Because of the beam's space charge, there is a velocity differential given by $\Delta v = \Delta \mathrm{E}/B = (\sigma/\epsilon_0)/B$ where σ is the surface charge density of the electron sheet (in C/m^2). Using this Δv in Eq. (1.12), the KH growth rate becomes

$$\omega_i = \frac{1}{2} k \tau \frac{\omega_p^2}{\omega_c} \tag{1.13}$$

where τ is the beam thickness (assuming $k\tau \ll 1$) and ω_p is the electron plasma frequency associated with the beam density n_0 ($en_0\tau = \sigma$). This growth rate is identical to the long wavelength limit of the diocotron instability on an electron sheet [5], [28].

The diocotron instability is also present in thick electron beams, which occupy a significant fraction of the AK gap (Figure 1.8). Buneman, Levy and Linson covered this topic in their 1966 paper [34]. They found that the strength of the diocotron instability in the non-relativistic regime is dependent on the factor $q \equiv \omega_p^2/\omega_c^2$. The dispersion relationship for an electron beam in contact with the cathode is given by

$$\frac{(\omega - k v_0)}{\omega_c} \cong \left(-\frac{q}{2} - \frac{q^2}{4} + 0.2q^3 \right) + i \left(\frac{q\pi}{2e} - 0.13q^2 \right) e^{-2/q}. \tag{1.14}$$

where ω is the complex eigenfrequency, v_0 is the maximum electron velocity in the shear flow, and e = 2.718. Brillouin flow occurs at $q = 1$, as described in Eq. (1.8a). In this limit, Eq. (1.14) becomes

$$\frac{(\omega - k v_0)}{\omega_c} \cong -0.55 + 0.06i. \tag{1.15}$$

The addition of relativistic effects causes a decrease in growth rate of the diocotron instability with increasing relativistic energy [32], [35]. Instability in planar Brillouin flow will be covered in more detail in Chapter 3.

1.3.2 Negative mass instability

The negative mass instability is a cylindrical effect wherein an azimuthal force applied to an object causes a change in azimuthal velocity in the opposite direction of the force, as though the mass were negative in the force equation. This term was first used by Maxwell to explain why the rings around Saturn stayed in equilibrium instead of coalescing as a result of gravitational

attraction [36], [37]. For a ring of electrons experiencing Coulomb repulsion due to a perturbation, the negative mass instability causes azimuthal bunching and a growth of the initial perturbation. The negative mass instability was predicted in circular accelerators [29], [30]. For a rotating electron beam subject to a radial electric field (E_0) and axial magnetic field (B_0), the ratio of the electric force to the centripetal force governs whether the effective mass of an electron is negative or positive. This term will be defined through [38]

$$h = \frac{erE_0}{m_0\gamma^3 v_0^2}, \qquad (e > 0) \tag{1.16}$$

where $\gamma = 1/\sqrt{1 - v_0^2/c^2}$ is the relativistic mass factor associated with the electron rotation speed v_0, m_0 is the electron rest mass, and r is the radius of the electron. Note from Eq. (1.16) that $\gamma^2 h$ is the ratio of the radial electric field force to the total centripetal force. Therefore h measures the radial electric field, including its direction. A negative (positive) h means that the cathode is inside (outside) of the anode and represents a conventional (inverted) magnetron configuration. The effective mass is related to h by [5], [38], [39]

$$m_{eff} = -m_0\gamma\left(\frac{1+\gamma^2 h^2}{v_0^2/c^2 + 2h}\right). \tag{1.17}$$

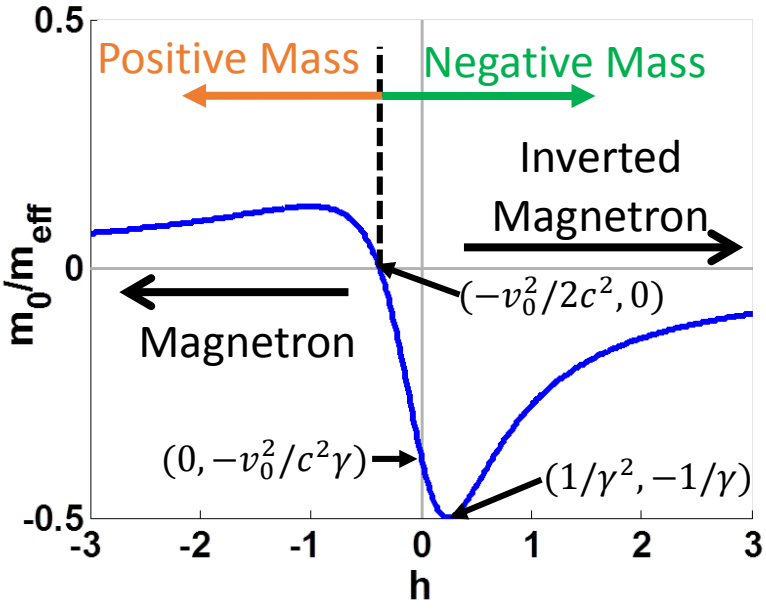

Figure 1.11: The inverse of the effective mass of a thin electron beam with γ = 2 as a function of h. The minimum occurs at $h = 1/\gamma^2$. At $h = -v_0^2/2c^2$, $m_0/m_{eff} = 0$, i.e., $m_{eff} = \infty$.

Figure 1.11 shows the values of h that correspond to positive and negative mass for a *thin electron beam* with $\gamma = 2$. At $h = 0$, the electric field is zero and the rotating electrons are in equilibrium due solely to the magnetic field, which corresponds to a large orbit gyrotrons in which the electron cyclotron motion encircles the axis of a cylindrical waveguide [5], [38]. The lowest value of m_0/m_{eff}, which is always negative, occurs at $h = 1/\gamma^2$, which is where there is no external magnetic field, like an orbitron configuration. There is infinite effective mass ($m_{eff} = \infty$) at $h = -v_0^2/2c^2$, so any perturbations on the electron beam remain constant, neither growing nor decaying [39]. The inverted magnetron occupies the positive h space to the right in Figure 1.11, while the conventional magnetron occupies the negative h space to the left, due to the direction of the radial electric field (positive for inverted, negative for conventional). A thin beam with an initial density perturbation undergoing instability due to the negative mass effect is shown in Figure 1.12. The growth rate of the perturbation matches closely to the predicted growth rate based on the analytical formulation [39]. The same simulation [39] also shows stable "positive mass" oscillations at $h = -2$, consistent with Figure 1.11. The negative mass effect seems to be present in the circular bends of the RPM in Figure 1.6.

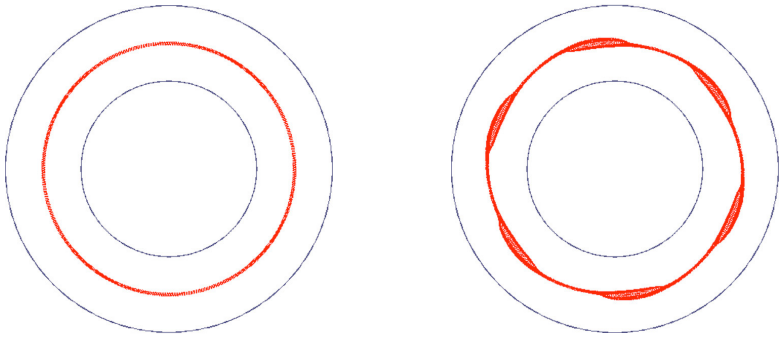

Figure 1.12: Electron beam in inverted magnetron configuration at start of a PIC simulation (left) and 11.5ns later (right) for $h = 2$, from [39]

For thin beam devices such as the large orbit gyrotron, h is effectively constant for the entire electron beam. A constant h allows for an analytical solution to the dispersion relation [38], which has been proven accurate in comparisons with particle-in-cell simulations [39]. The diocotron instability appears as a second order residual instability in the analytical negative mass formulation for a thin beam [38], [31]. When the system is brought to the planar limit, the negative mass instability disappears and only the diocotron instability remains. Interestingly, finite thickness of the electron beam, specifically an increase in the velocity gradient across the beam,

leads to decreased perturbation growth and even stabilization of the negative mass instability [40], [41], and of the diocotron instability [42], [43].

Cylindrical Brillouin flow has large gradients in both the electric field and electron velocity, leading to a substantial radial dependence of h. The interaction between the negative mass behavior and the effect of the large velocity shear within the Brillouin flow with and without a slow wave structure on the anode are questions central to this thesis, and will be covered in Chapters 3 and 4.

1.4 Thesis organization

The focus of this thesis is instabilities within the Brillouin flow. No previous studies have included a slow-wave structure, nor the positive/negative mass effect in rotating Brillouin flow. This thesis will provide a systematic study of Brillouin flow so as to understand magnetron stability and startup, as well as the nature of mode competition. These are known, unsolved issues in magnetron research.

To that end, Chapter 2 will first cover properties of equilibrium Brillouin flow, both non-relativistic and relativistic and both planar and cylindrical. One such property is the existence of a relation between the vector magnetic potential and scalar electric potential that mirrors the forms of the Hull cutoff and Buneman-Hartree conditions. Also in Chapter 2 is a reexamination of the Buneman-Hartree condition for cylindrical Brillouin flow, including, for the first time, inverted magnetrons. The Brillouin flow Buneman-Hartree condition compares favorably to both experimental and simulation data on relativistic magnetrons. In addition, analytic Brillouin flow and particle-in-cell simulation profiles are shown to be close matches for electric and magnetic field strength and electron density and velocity. Taken together, these two studies corroborate the notion that Brillouin flow is the dominant state before spoke formation in an operating magnetron.

Chapter 3 contains a comprehensive examination of instabilities on the Brillouin flow in smooth-bore magnetron. A comparison of growth rates between conventional, inverted and planar magnetrons confirms the existence of the negative mass effect. The analysis in this chapter is electrostatic and non-relativistic, but is shown to transition into the fully electromagnetic and relativistic regime smoothly. Chapter 4 extends the investigation into magnetrons with slow wave structures. Multiple space harmonics are taken into account, and the interaction of the Brillouin

flow instabilities and the synchronous mode of the circuit in the slow wave structure is found to be dominant. Finally, Chapter 5 summarizes this thesis and provides direction for future work.

CHAPTER 2

Equilibrium Properties of Brillouin Flow

2.1 Introduction to Brillouin Flow

The physicist Léon Brillouin, in the process of developing a theory on the operation of magnetrons, described equilibrium electron motion around the cathode of a cylindrical magnetron as concentric orbits, instead of the typical cycloidal orbits normally undergone by a single charged particle in crossed electric and magnetic fields [44]. His proposal resulted in a space-charge limited laminar flow around the cathode. In this system, electrons have a velocity that is parallel to the cathode (and orthogonal to both the electric field and magnetic field) and axisymmetric. Each electron is assumed to have been emitted from the cathode with zero velocity and energy so that the total energy (kinetic and potential) of each electron in the Brillouin flow is equal to zero. The resulting equilibrium, in both cylindrical and planar [45] geometry, is now known as Brillouin flow. Figure 2.1 shows the Brillouin flow for both geometries, which is directly comparable to the single particle orbit in Figure 1.7 and planar Brillouin flow in Figure 1.8. The two models are in direct contention over which best describes electron behavior within a magnetron. J.C. Slater, a contemporary of Brillouin, hypothesized that the cycloidal orbits are unstable, and that a perturbation would cause them to collapse to a near-Brillouin flow state [17]. Modern particle-in-cell (PIC) simulations of magnetrons show this to be true, at least for the time period before spokes form [20]. The resulting electron flow is termed near-Brillouin flow because it exhibits a mild background turbulence superimposed over the laminar Brillouin flow. Extensive work has been performed using PIC simulations to quantify this behavior [18], [21]. The cycloidal orbits have been shown to collapse in response to a small AC voltage applied to the AK gap [22], a resistive external circuit element [18], or small misalignments in the external magnetic field [46]. The ease of destabilization for cycloidal orbits has led to the hypothesis that near-Brillouin flow is the default state for all magnetrons and any crossed-field devices in which electrons are emitted within

the interaction region [17], [18], [20]–[22], [46]. See the last two paragraphs of Section 1.2.2 for the relationship between cycloidal orbits and Brillouin flow.

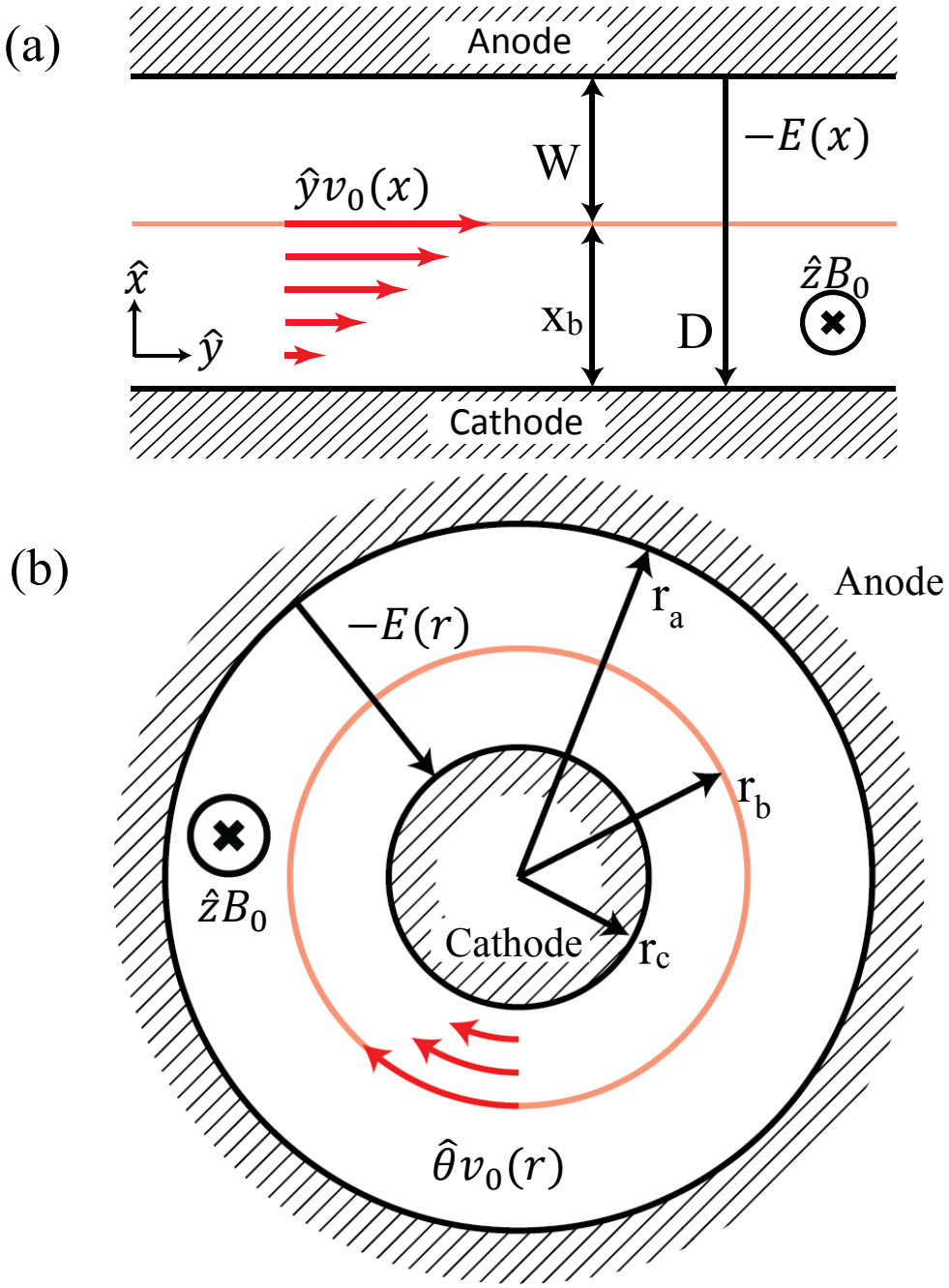

Figure 2.1: Brillouin flow in planar (a) and cylindrical (b) smooth-bore magnetrons. The electron velocities and electric field are both zero at the cathode. In the non-relativistic approximation, the magnetic field is constant.

This chapter will cover the formulation of equilibrium Brillouin flow in both the non-relativistic and fully relativistic limits, and for both planar and cylindrical magnetrons. The

magnetrons will be treated as though they have a smooth anode, which is known as "smooth-bore." The solution to the cylindrical, relativistic case will be explored in greater detail, and will include parallels to the single particle operating conditions outlined in Chapter 1. Example profiles based on real, experimental devices will be presented in Section 2.4. The main purpose of this chapter is to establish the equilibrium Brillouin flows for the perturbation stability analysis in the following chapters. The non-relativistic flows will have electrostatic perturbations applied to them, while the relativistic flows will have fully electromagnetic perturbations. The equilibrium flow solutions yield the two conditions, the Hull cutoff condition and the Buneman-Hartree condition. They will be applied to recent experimental data and simulation results on relativistic magnetrons in Section 2.5.

2.2 Non-Relativistic Brillouin Flow

The most basic form of Brillion flow is derived under the assumption that the electron velocities are non-relativistic. As a consequence, the magnetic field caused by the electron current is ignored, and only the constant, externally applied magnetic field is considered. Commercial microwave oven magnetrons operate within this region. It allows for very high efficiency, although the overall power that can be produced from non-relativistic magnetrons is limited.

2.2.1 Planar

The planar Brillouin flow is shown in Figure 2.1a. The derivation will be covered below, and the end result will be a set of simple equations for electric field and electron density and velocity within the Brillouin flow, along with the relationship between the externally applied voltage, magnetic field, the Brillouin hub height, and the electron velocity at the top of the hub. The Brillouin hub height marks the location of the electrons that are farthest from the cathode, x_b in Figure 2.1a, and is designated within this thesis by a subscript *b*. The hub height is the same as the maximum excursion by a single particle into a vacuum AK gap of the same voltage and magnetic field, and both represent the degree of magnetic insulation in the system.

The following equations represent the conditions for the planar Brillouin flow shown in Figure 2.1a,

$$\boldsymbol{v}(x,y) = \hat{y}v_0(x), \tag{2.1}$$

where **v** is the electron velocity which is parallel to the cathode and uniform in the direction of motion. Zero net electron energy is represented by setting sum of potential and kinetic energy in the conservation of energy equation to zero,

$$\frac{1}{2}mv_0^2 - e\phi(x) = 0, \tag{2.2}$$

where -*e* is the charge of an electron, *m* is the mass of an electron, and ϕ is the scalar electric potential, which is related to the electric field by $\boldsymbol{E} = -\nabla\phi$. The total potential over the AK gap, D, as shown in Figure 2.1(a), is $\phi(D) = V$ where V is the externally applied voltage. At the cathode, x = 0, the boundary conditions are

$$v_0(0) = 0, \qquad \phi(0) = 0. \tag{2.3}$$

The electric field is defined as $\boldsymbol{E} = E_0(x)\hat{x}$ and the magnetic field is $\boldsymbol{B} = B_0\hat{z}$ where B_0 is constant. The Lorentz force equation has no acceleration term in this steady state equilibrium, so the electric and magnetic forces are balanced,

$$-e[E_0 + v_0B_0] = 0. \tag{2.4}$$

As a result, the electron velocity is simply

$$v_0 = -E_0/B_0, \tag{2.5}$$

which is the familiar velocity for the E×B drift of an electron in crossed fields ($-E_0$ is in the –x direction in Figure 2.1a). Differentiating Eq. (2.2) with respect to x and using Eqs. (2.3) and (2.5), we obtain,

$$v_0(x) = \hat{y}\omega_c x, \tag{2.6}$$

where $\omega_c = |eB_0|/m$ is the cyclotron frequency for electrons. Equations (2.2) and (2.6) imply that $\phi(x) = \frac{1}{2}m(\omega_c x)^2$ and with Poisson's equation give

$$\omega_c^2 = \omega_p^2, \tag{2.7}$$

where ω_p is the plasma frequency $\omega_p^2 = e^2n_0/\epsilon_0 m$ in this (non-neutral) Brillouin flow, n_0 is the electron density, and ϵ_0 is the free space vacuum permittivity. The B field, and thus ω_c, is constant in planar non-relativistic flow, so Eq. (2.7) shows that density is constant across the entire Brillouin flow. The last piece of information needed to fully define the Brillouin flow is the Brillouin hub height. The hub height in the planar case comes from an integration of the electric field over the AK gap to find the total applied voltage,

$$x_b = D - \sqrt{D^2 - \frac{2V}{\omega_c B_0}}, \tag{2.8}$$

where x_b is the Brillouin hub height. Equation (2.8) may also be written as

$$\frac{x_b}{D} = 1 - \sqrt{1 - \frac{V}{V_H}} = 1 - \sqrt{1 - \left(\frac{B_H}{B}\right)^2}, \tag{2.9}$$

where $V_H = eD^2B_0^2/2m$ is called the "Hull cutoff voltage" and $B_H = (2mV/eD^2)^{1/2}$ is called the "Hull cutoff magnetic field." If $V > V_H$ or $B_0 < B_H$, there is no magnetic insulation in the crossed-field diode.

The non-relativistic planar Brillouin flow is fully defined by Eqs. (2.3), (2.6), (2.7), and (2.8) or (2.9). The magnetic field and electron density are constant, the electron velocity and electric field within the flow are linearly increasing away from the cathode. The applied voltage, the magnetic field, and the gap spacing completely specify the Brillouin flow.

2.2.2 Cylindrical

The cylindrical geometry (Figure 2.1b) is somewhat more complex than the planar case, due mostly to the addition of the centrifugal force term in the force equation,

$$\frac{mv_\theta^2}{r} = -e[E_0 + v_\theta B_0]. \tag{2.10}$$

In the cylindrical geometry, the velocity is defined as $\boldsymbol{v}(r,\theta) = \hat{\theta} v_\theta(r)$. The derivation follows the same steps as the planar case and is presented in the Appendix.

$$v_\theta(r) = \frac{1}{2}\,\omega_c \frac{r^2 - r_c^2}{r}, \tag{2.11}$$

$$E_0(r) = -B_0\omega_c \frac{r^4 - r_c^4}{4r^3}, \tag{2.12}$$

$$\omega_p^2 = \omega_c^2\left[1 - \frac{1}{2}\frac{r^4 - r_c^4}{r^4}\right], \tag{2.13}$$

$$V = \frac{1}{2}B_0\omega_c \frac{(r_b^2 - r_c^2)^2}{2r_b^2} + \frac{1}{4}B_0\omega_c \frac{r_b^4 - r_c^4}{r_b^2}\ln\left(\frac{r_a}{r_b}\right). \tag{2.14}$$

In these equations r_c is the cathode radius, r_a is the anode radius, and r_b is the radius at the top of the Brillouin hub (Figure 2.1b). The Brillouin hub radius, r_b, needs to be solved numerically from Eq. (2.14), given V, B_0, r_a and r_c. Equations (2.11), (2.12), and (2.13) apply to the Brillouin flow region: $|r_b - r_c| > |r - r_c| \geq 0$. This change from the derivations in the literature [26], [44] means

that Eqs. (2.11) through (2.14) are valid for both the conventional ($r_c < r_a$) and the inverted ($r_c > r_a$) geometry. Unlike the planar case, the cylindrical magnetrons have the property that $\omega_p^2 = \omega_c^2$ only at the cathode. The cylindrical equations reduce to the planar equations in the limit that all radii go to infinity, but the AK gap separation, $|r_c - r_a|$, stays constant.

2.3 Relativistic Brillouin Flow

This section will cover the form of planar Brillouin flow and the process of finding solutions for the cylindrical Brillouin flow. Theses fully relativistic formulations include the effects of self-magnetic fields, which were negligible in the non-relativistic versions in Section 2.2. The magnetrons that operate in the relativistic regime are high-power devices. The high power comes from increased applied voltage and magnetic fields (required for magnetic insulation), which cause the electrons to gain velocity. This can be seen from the scaling of the planar non-relativistic flow equations. For a fixed Brillouin hub height, Eq. (2.8) shows that the applied voltage must increase with the square of the magnetic field. Equation (2.6) shows that the velocity is directly proportional to B_0 for a constant hub height. An increased voltage and magnetic field that result in a constant Brillouin hub height are accompanied by an increase in velocity of electrons at the Brillouin hub.

2.3.1 Planar

The relativistic planar formulation is cleanly laid out in Section 8.3.3 in Davidson's book [26]. This section summarizes those results.

As with the non-relativistic planar flow, the cyclotron and plasma frequencies are related at all points across the hub, (Figure 2.1a)

$$\frac{\omega_c^2(x)}{\gamma_0^2} = \frac{\omega_p^2(x)}{\gamma_0} \tag{2.15}$$

In Eq. (2.15), $\omega_c(x)$ and $\omega_p(x)$ are the non-relativistic cyclotron frequency and plasma frequency, respectively, and $\gamma_0(x) = [1 - \beta_0^2(x)]^{-1/2}$ and $\beta_0(x) = v_0(x)/c$ are the relativistic factors. The properties within the hub are given by

$$B_z = \frac{B_0 \cosh(\kappa x)}{\cosh(\kappa x_b)}, \tag{2.16}$$

$$E_x(x) = -\frac{B_0 \sinh(\kappa x)}{\cosh(\kappa x_b)}, \tag{2.17}$$

$$v(x) = c\tanh(\kappa x), \tag{2.18}$$

$$\gamma_0(x) = \cosh(\kappa x), \tag{2.19}$$

$$n(x) = \frac{n_0 \cosh(\kappa x)}{\cosh(\kappa x_b)}, \tag{2.20}$$

where $B_0/\cosh(\kappa x_b)$ is the magnetic field at the cathode, $n_0/\cosh(\kappa x_b)$ is the density at the cathode, and κ is a constant, defined as the value of ω_c/c (or ω_p/c) evaluated on the cathode surface. Equations (2.16) and (2.19) then imply that ω_c/γ_0 is also a constant. These values are plotted later, in Figure 2.6. The total voltage across the AK gap is given by

$$\frac{eV}{m_0c^2} = \cosh(\kappa x_b) - 1 + \kappa(D - x_b)\sinh(\kappa x_b), \tag{2.21}$$

in which the first two terms on the right-hand side are the potential at the top of the hub, and the third term is the potential across the vacuum region. The initial magnetic fill field, B_f, is

$$\frac{eB_fD}{m_0c^2} = \sinh(\kappa x_b) + \kappa(D - x_b)\cosh(\kappa x_b). \tag{2.22}$$

The magnetic fill field is the initial constant magnetic field applied to the vacuum region before the electrons are introduced. It is assumed that the magnetic flux is conserved within the system, so the flux from the magnetic fill and the flux after the Brillouin flow is established are the same. This constant magnetic flux relates B_f and B_0 by

$$B_fD = \frac{B_0}{\kappa}\tanh(\kappa x_b) + B_0(D - x_b). \tag{2.23}$$

From the set of applied AK gap voltage, magnetic fill field, and gap separation, the two quantities κx_b, and κ, must be numerically solved for from (2.21) and (2.22). The ratio of these two quantities gives x_b, and B_0 is then obtained from Eq. (2.23). The rest of the quantities are given by Eq. (2.16) through (2.20).

2.3.2 Cylindrical

Relativistic cylindrical magnetrons are popular choices for frontier research into high-power magnetrons [10], [47], [48]. They are also the most complicated devices to analyze. For this reason, this section will go into detail for the derivation.

The relativistic, cylindrical Brillouin flow satisfies the following equations within the hub,

$$-e\phi(r) + [\gamma_0(r) - 1]m_0c^2 = 0, \tag{2.24}$$

$$\frac{\gamma_0 m_0 v_0^2}{r} = -e(E + v_0B). \tag{2.25}$$

The axial magnetic field $\mathbf{B} = \hat{z}B_z(r)$ is related to the vector potential $\mathbf{A} = \hat{\theta}A$, by $\mathbf{B} = \nabla \times \mathbf{A}$. Since $v_0(r_c) = 0$ for the Brillouin flow, together with $A(r_c) = 0$, Eqs. (2.24) and (2.25) imply that the total canonical angular momentum is conserved [25],

$$-eA(r) + m_0\gamma_0(r)v_0(r) = 0. \tag{2.26}$$

In fact, any two of Eqs. (2.24), (2.25), and (2.26) imply the third, upon using the definitions of the electric and magnetic fields,

$$E(r) = -\frac{d\phi(r)}{dr}, \tag{2.27}$$

$$B(r) = \frac{1}{r}\frac{d}{dr}[rA(r)]. \tag{2.28}$$

We shall show below that Eqs. (2.24) and (2.26), together with the boundary conditions of the Brillouin flow on the cathode surface,

$$E(r_c) = 0, \qquad v_0(r_c) = 0, \qquad \phi(r_c) = 0, \qquad A(r_c) = 0, \tag{2.29}$$

yield a Buneman-Hartree-like (BHL) condition and a Hull Cutoff-like (HCL) condition that relate $\phi(r)$ and $A(r)$ *everywhere* within the Brillouin hub [49]. We shall also show that these solutions of $\phi(r)$ and $A(r)$ constructed from Eqs. (2.24) and (2.26) also imply Eq. (2.25). Note that both $\phi(r)$ and $A(r)$ still need to be solved self-consistently, taking into account the space charge density, $-en_0(r)$, and the azimuthal current density $-en_0(r)v_0(r)$, of the Brillouin flow. Such solutions were obtained by Davidson *et al.*[50].

Equations (2.24)–(2.28) are valid even if there is an arbitrary distribution of ions that is axisymmetric, and even if the electric field on the cathode is nonzero. It would then appear that the Buneman-Hartree-like condition and the Hull Cutoff-like condition derived from them (mentioned in the preceding paragraph) are valid in the presence of an axisymmetric ion distribution in the crossed-field gap, under non-space-charge limited conditions. This "naïve" generalization of the Brillouin flows turns out NOT to be the case, and we shall postpone the discussion of this rather subtle point in the concluding section of this chapter, Sec. 2.6. For the remaining parts, we shall restrict mainly to the conventional Brillouin flow model where there are no ions, and the electric field on the cathode surface is zero.

We find it convenient to normalize the electrostatic potential ϕ by m_0c^2/e, the vector potential A by m_0c/e, and all linear dimensions by the anode radius, r_a. These normalized quantities are denoted with a bar,

$$\bar{\phi} = \frac{e\phi}{m_0 c^2}, \qquad \bar{A} = \frac{eA}{m_0 c}, \qquad \bar{r} = \frac{r}{r_a}, \qquad \beta_0 = \frac{v_0}{c}, \qquad \gamma_0 = (1-\beta_0^2)^{-\frac{1}{2}}. \tag{2.30}$$

Equations (2.24)–(2.26) are then non-dimensionalized,

$$\bar{\phi} = \gamma_0 - 1, \tag{2.31}$$

$$\gamma_0 \beta_0^2 = -\bar{r}(\bar{E} + \beta_o \bar{B}), \tag{2.32}$$

$$\bar{A}(\bar{r}) = \gamma_0(\bar{r})\beta_0(\bar{r}), \tag{2.33}$$

where the normalized electric and magnetic fields in Eqs. (2.27) and (2.28) become,

$$\bar{E} = -\frac{d\bar{\phi}}{d\bar{r}} = \frac{eEr_a}{m_0 c^2}, \qquad \bar{B} = \left(\frac{1}{\bar{r}}\right)\frac{d(\bar{r}\bar{A})}{d\bar{r}} = \frac{eBr_a}{m_0 c}. \tag{2.34}$$

It is convenient to introduce the function, χ, to represent the Brillouin flow velocity, where [26], [50], [51]

$$\beta_0(\bar{r}) = \tanh \chi(\bar{r}). \tag{2.35}$$

The relativistic mass factor then reads,

$$\gamma_0(\bar{r}) = \cosh \chi(\bar{r}). \tag{2.36}$$

The normalized scalar and vector potential become [cf. Eqs. (2.31) and (2.33)],

$$\bar{\phi}(\bar{r}) = \cosh \chi(\bar{r}) - 1, \tag{2.37}$$

$$\bar{A}(\bar{r}) = \sinh \chi(\bar{r}). \tag{2.38}$$

From Eqs. (2.37) and (2.38), it is easy to verify that $\bar{\phi}$ and $\bar{A}$ satisfy the Hull cutoff like (HCL) condition *everywhere* within the Brillouin hub,

$$\bar{A}(\bar{r}) = \sqrt{2\bar{\phi}(\bar{r}) + [\bar{\phi}(\bar{r})]^2} \quad \text{(Hull cutoff like)}. \tag{2.39}$$

It is equally easy to verify from Eqs. (2.35), (2.37) and (2.38) that $\bar{\phi}$ and $\bar{A}$ also satisfy the Buneman-Hartree like (BHL) condition *everywhere* within the Brillouin hub,

$$\bar{\phi}(\bar{r}) = \bar{A}(\bar{r})\beta_0(\bar{r}) - \left[1 - \sqrt{1-\beta_0^2(\bar{r})}\right] \quad \text{(Buneman-Hartree like)}. \tag{2.40}$$

Compare Eq. (2.39) with Eq. (1.10), which is the Hull cutoff condition, and Eq. (2.40) with Eq. (1.11), which is the Buneman-Hartree condition. We stress that Eqs. (2.39) and (2.40) include the effects of the space charge and of the space current in the cylindrical, relativistic Brillouin flow. Finally, using Eqs. (2.37) and (2.38) into Eq. (2.34), together with Eqs. (2.35) and (2.36), one may easily verify that the force law, Eq. (2.32), is satisfied. This demonstrates that Eqs. (2.24) and (2.26) imply Eq. (2.25), everywhere within the Brillouin flow.

From Eqs. (2.37) and (2.38), we can see that knowledge of the function $\chi(r)$ will give both $\bar{\phi}$ and $\bar{A}$, and that Eq. (2.35) gives β_0. The remaining piece of the puzzle is the form of $\chi(\bar{r})$, and the process of obtaining it starts with Maxwell's equations, the Lorentz force equation, and conservation of energy. The normalized force equation is Eq. (2.32), the normalized conservation of energy is Eq. (2.31), and the normalized Maxwell equations of interest are

$$\nabla \cdot \bar{E} = \frac{1}{\bar{r}} \frac{\partial}{\partial \bar{r}} (\bar{r}\bar{E}) = -\bar{n}, \tag{2.41}$$

$$\nabla \times \bar{B} = -\frac{\partial \bar{B}}{\partial \bar{r}} = -\bar{n}\beta_0, \tag{2.42}$$

where $\bar{n}(r) = \omega_p^2(r) r_a^2 / c^2$ and ω_p^2 does not include the relativistic mass factor. The derivative of Eq. (2.31) is

$$\bar{E} = -\frac{\partial \gamma_0}{\partial \bar{r}}. \tag{2.43}$$

The next step is to arrive at an equation that is only a function of velocity (β and γ) and radius. First, the electric field from Eq. (2.43) is substituted into the force law, Eq. (2.32), which is then solved for $\bar{B}$. The resulting equation for $\bar{B}$ is plugged into Eq. (2.42). The equation for the electric field, (2.43), is used in Eq. (2.41) to find $\bar{n}$, which is then also plugged into Eq. (2.42). The final equation relates velocity and radius,

$$\frac{\beta_0}{\bar{r}} \frac{\partial}{\partial \bar{r}} \left(\bar{r} \frac{\partial \gamma_0}{\partial \bar{r}} \right) = \frac{\partial}{\partial \bar{r}} \left[\frac{\gamma_0 \beta_0^2 + \bar{r} \frac{\partial \gamma_0}{\partial \bar{r}}}{\bar{r}\beta_0} \right]. \tag{2.44}$$

The definitions of β_0 and γ_0 in terms of χ from Eqs. (2.35) and (2.36) can be used to greatly simplify Eq. (2.44), [50],

$$\frac{\partial}{\partial \bar{r}} \left(\bar{r} \frac{\partial \chi}{\partial \bar{r}} \right) = \frac{\sinh \chi \cosh \chi}{\bar{r}}. \tag{2.45}$$

Taking into account the boundary conditions, [$\bar{E} = \beta = 0,$ and $\partial \bar{E} / \partial \bar{r} = -\bar{n}$ at $\bar{r} = \bar{r}_c$], we have

$$\chi(\bar{r}_c) = 0, \qquad \frac{\partial \chi}{\partial \bar{r}} = \sqrt{\bar{n}(\bar{r}_c)} = \bar{\kappa}. \tag{2.46}$$

Two integrations of (2.45) yield

$$\ln \frac{\bar{r}}{\bar{r}_c} = \int_0^{\chi} \frac{d\chi}{\sqrt{\bar{\kappa}^2 \bar{r}_c^2 + \sinh^2 \chi}}. \tag{2.47}$$

Two more equations are needed. The first is the total voltage,

$$\bar{V} = \cosh\chi(\bar{r}_b) - 1 + \sinh\chi(\bar{r}_b)\ln\frac{\bar{r}_c}{\bar{r}_b}\sqrt{\bar{\kappa}^2\bar{r}_c^2 + \sinh^2\chi(\bar{r}_b)}, \tag{2.48}$$

where the first two terms account for the voltage drop across the Brillouin hub [c.f. (Eq. (2.37)] and the third term accounts for the voltage drop in the vacuum region. The second equation is the magnetic flux,

$$\bar{B} = \frac{1}{\bar{r}_b(1-\bar{r}_c^2)}\Big[(1+\bar{r}_b^2)\sinh\chi(\bar{r}_b) + (1-\bar{r}_b^2)\cosh\chi(\bar{r}_b)\sqrt{\bar{\kappa}^2\bar{r}_c^2 + \sinh^2\chi(\bar{r}_b)}\Big]. \tag{2.49}$$

Given the gap voltage $\bar{V}$, the total magnetic flux $\bar{B}$, and the geometry $\bar{r}_c$, the three quantities $\bar{\kappa}, \bar{r}_b$ and $\bar{\chi}(r_b)$ can be found from Eqs. (2.47), (2.48) and (2.49) as outlined in Appendix B of [25]. The value of $\bar{\kappa}$ allows Eq. (2.47) to be solved numerically for $\bar{r}$ as a function of χ, whose inverse gives $\chi(\bar{r})$ within the Brillouin hub, e.g., by rotating the χ and $\bar{r}$ axes in a graphical representation. Once χ as a function of radius is obtained, all properties within the profile are known. The velocity is immediately defined by Eq. (2.35), and with this, the scalar and vector potentials from Eqs. (2.37) and (2.38), the electric field from Eq. (2.43), and the density from Eq. (2.41). As with the non-relativistic case, these equations are valid for the inverted magnetron configuration.

2.4 Example Profiles

The previous two sections outline the methods for finding the equilibrium solution to Brillouin flow. These solution can be applied to existing experimental setups in order to visualize density, velocity, and electric and magnetic field strengths. Two experimental magnetrons have been chosen, both operated at the University of Michigan's Plasma, Pulsed Power, and Microwave Laboratory and powered by the Michigan Electron Long Beam Accelerator (MELBA). Typical MELBA pulses for the relativistic magnetrons are on the order of 0.5μs -1μs and have voltage in the range of 300-400kV and magnetic field from 0.1-0.3T [10], [14], [52]–[54]. These parameters mean that MELBA operates in a relativistic regime, so the relativistic formulations will be needed. The first experiment is the RPM-12a [11]–[14]. RPM stands for recirculating planar magnetron and consists of two parallel planar interaction regions, with circular bends to allow electrons to travel between them. It is illustrated in Figure 2.2. The geometry of the planar section will be used for an example of relativistic planar profiles. The second experiment is a six vane cylindrical magnetron [52], [53], which will also be used for an example of conventional relativistic

magnetron profiles. This magnetron was used for multiple experiments, with different cathodes and one is shown in Figure 2.3, extracted from Brad Hoff's thesis [54]. Both of these devices are intended to operate at 1GHz. Both magnetrons will be approximated as smooth-bore in order to satisfy the uniformity assumption on Brillouin flow (As will be shown in Section 4.2 below, this assumption is well satisfied even with a vane structure on the anode). Additionally, the Brillouin hub height will be set to 50% of the AK gap, even if it would normally be lower at the MELBA operating conditions. The larger hub height better demonstrates the effect of cylindrical geometry on the flow profiles.

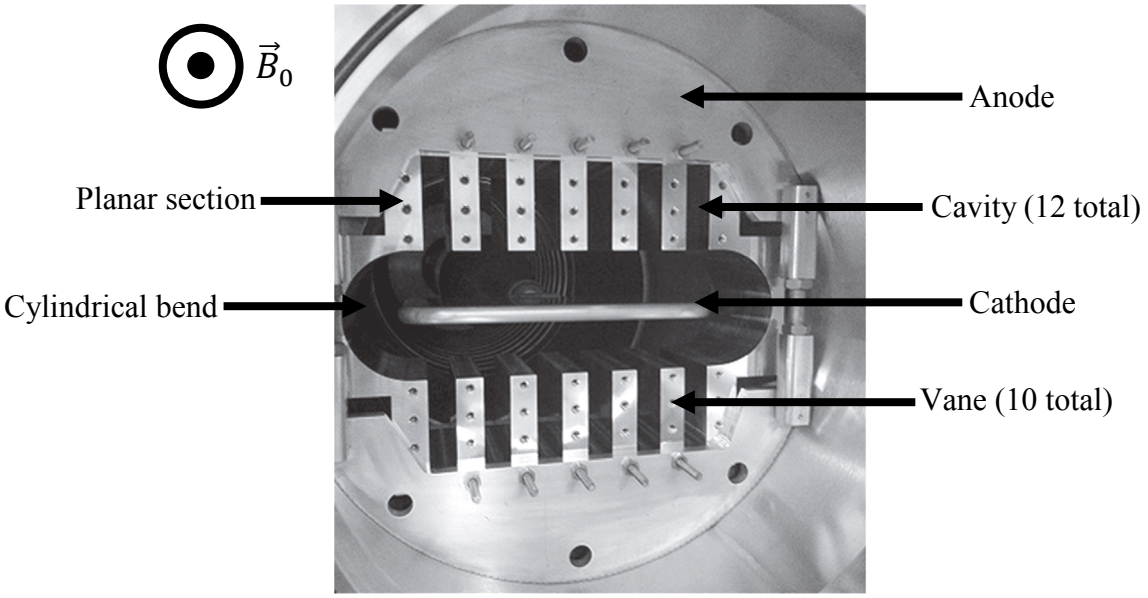

Figure 2.2: The RPM-12a inside the MELBA vacuum chamber [13].

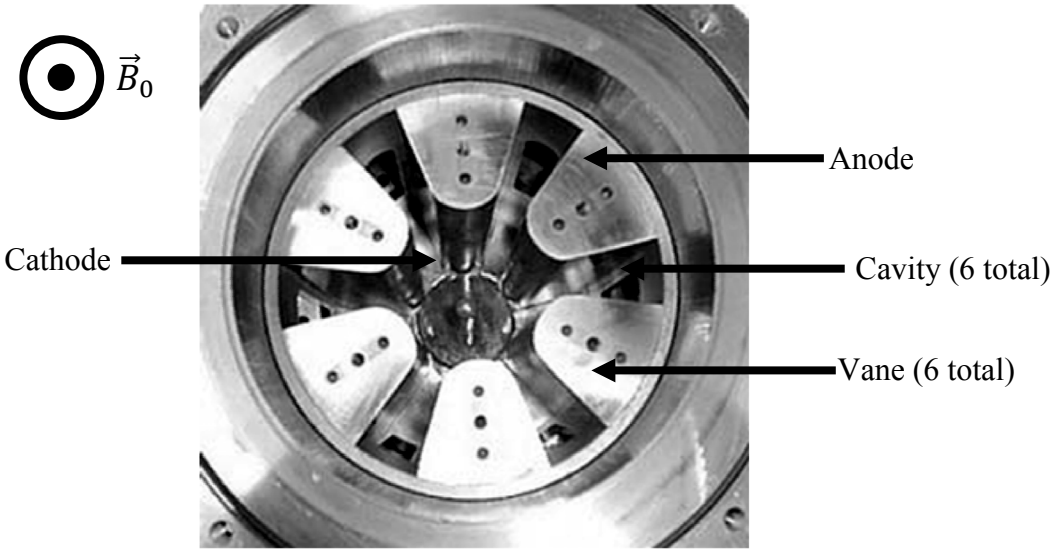

Figure 2.3: The 6-vane UM/L-3 relativistic magnetron block [54].

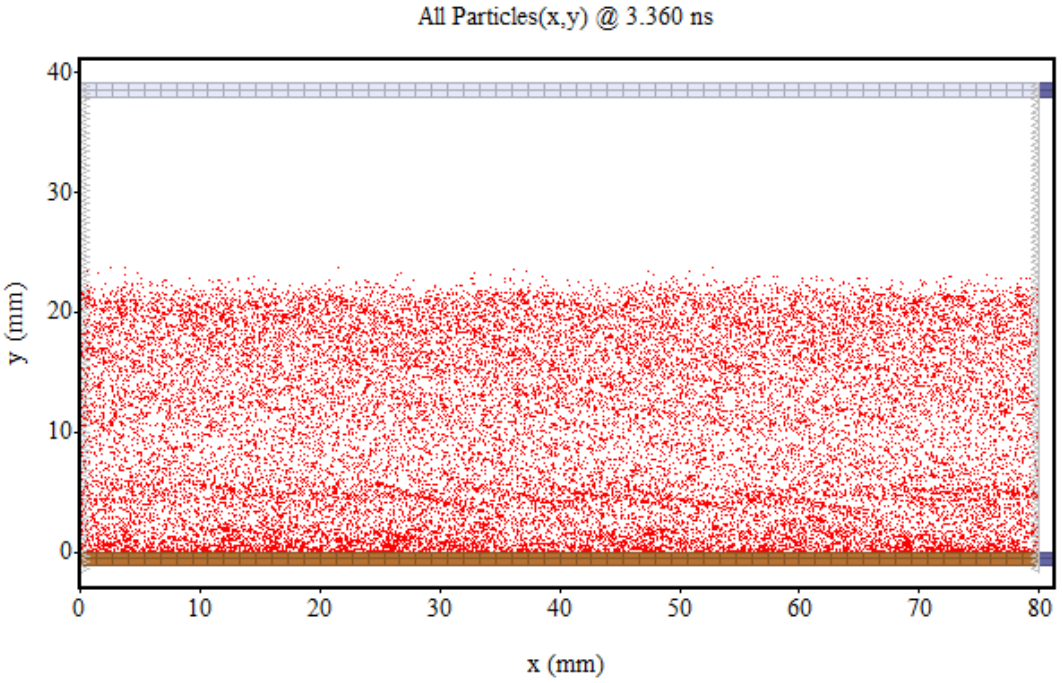

Figure 2.4: An example of near-Brillouin flow in the particle-in-cell (PIC) code MAGIC for a planar magnetron based on the representative parameters of UM magnetron (300kV, 0.06T).

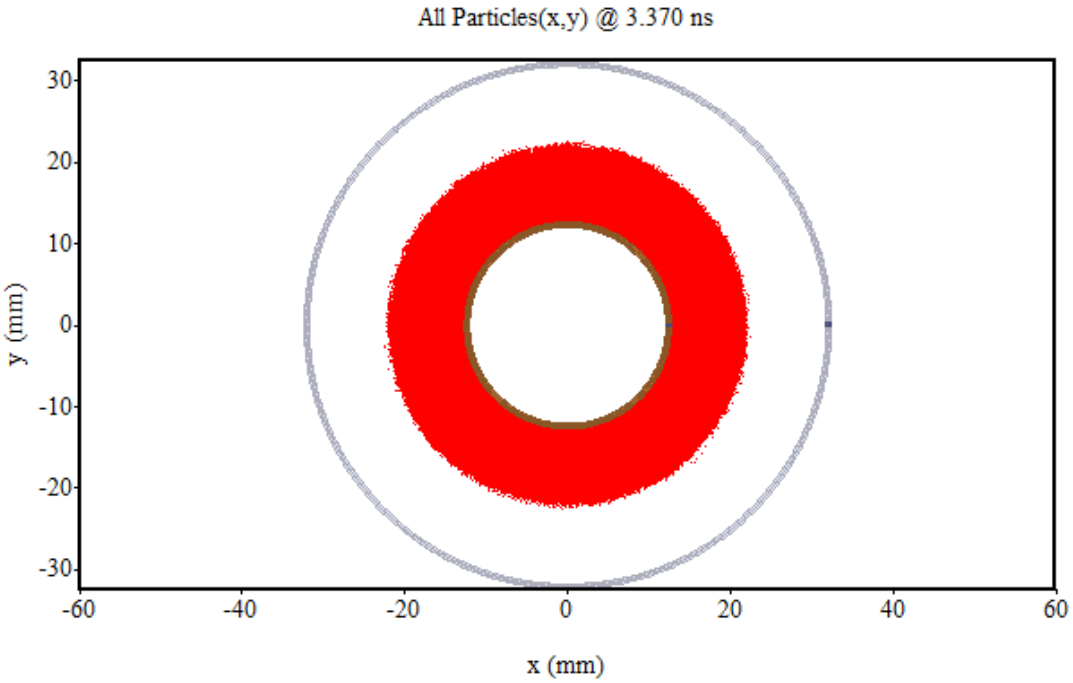

Figure 2.5: An example of near-Brillouin flow in the particle-in-cell (PIC) code MAGIC for a conventional magnetron based on the representative parameters of UM magnetron (300kV, 0.175T).

For comparison, profiles extracted from simulations performed using the electromagnetic finite-difference, time-domain PIC code MAGIC [55] will be presented as well. The MAGIC simulations use the same parameters as the analytic calculations. The voltage is slowly increased over 3ns to the final value, at which point the Brillouin flow is fully formed, such as in Figure 2.4 and Figure 2.5. In steady state, the E, B, and density profiles are averaged over 0.25ns. The electron velocity is taken from the phase space of (r, v_θ), so each point represents a macro particle.

The RPM-12a (the planar magnetron in Figure 2.2) has an AK gap of 3.9cm, a vane period of 3.84cm, of which the vanes occupy half, and a cavity height of 6.31cm. For the following profiles, it is assumed to be a smooth-bore magnetron (no vanes), operated at 300kV, with a magnetic field of 0.06T. These parameters result in a hub height of 1.95cm, half of the AK gap, shown in the MAGIC simulation in Figure 2.4. The planar profiles are shown in Figure 2.6. The planar plots show that $\beta(x_b)$ is ~0.5, so the system is somewhat relativistic. The velocity and electric field are roughly linear in x, starting from the zero value at the cathode ($x = 0$). The slope of the density plot and the slope of the magnetic field plot are the same, from their definitions, and as a result of Eqs. (2.16) and (2.20).

The 6-vane UM/L-3 relativistic magnetron (the cylindrical magnetron in Figure 2.3) has 6 vanes, a cathode radius of 1.27cm, an anode radius of 3.175cm, and a cavity wall outer radius of 8.26cm. This magnetron (like the planar magnetron) is assumed to be smooth-bore when generating the profiles. It has parameters of 300kV and 0.175T, which result in a hub radius of 2.225cm. The cylindrical profiles are shown in Figure 2.7. In addition to the profiles for the cylindrical magnetron operated in its conventional configuration, profiles for the inverted configuration are also calculated. The operating parameters for the inverted configuration are 300kV and 0.083T, with r_c = 3.175cm and r_a = 1.27cm (ignoring the vanes). The profiles for the inverted configuration are shown in Figure 2.8. The voltage is applied in the opposite direction to that of the conventional magnetron, so the sign of the electric field is opposite that of the conventional magnetron. The magnetic field is also reversed, in order to keep electron velocity in the same direction.

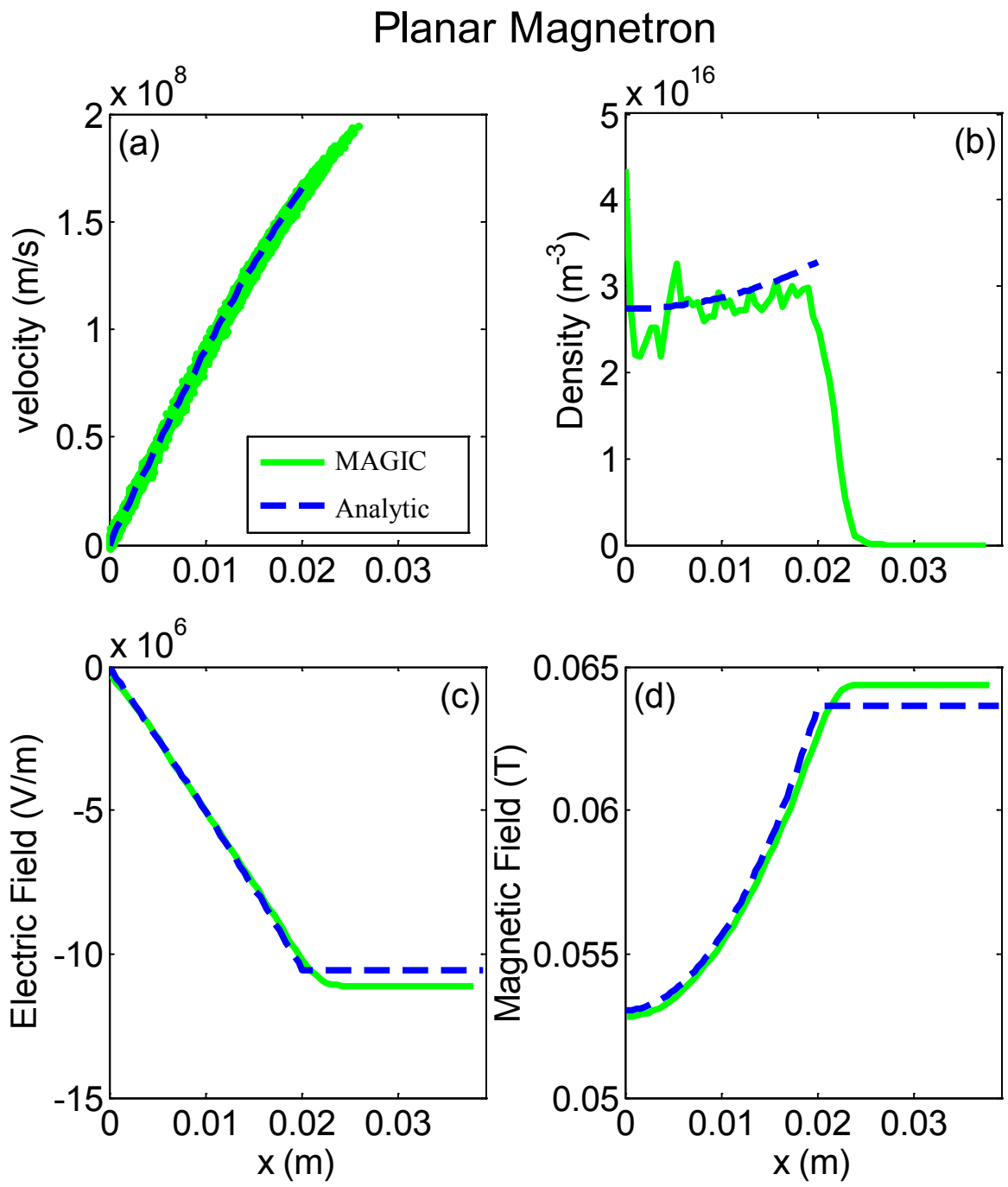

Figure 2.6: The equilibrium velocity (a), density (b), electric field (c), and magnetic field (d) for both the analytic Brillouin flow model and MAGIC PIC simulations for the RPM-12a operated at 300kV and 0.06T.

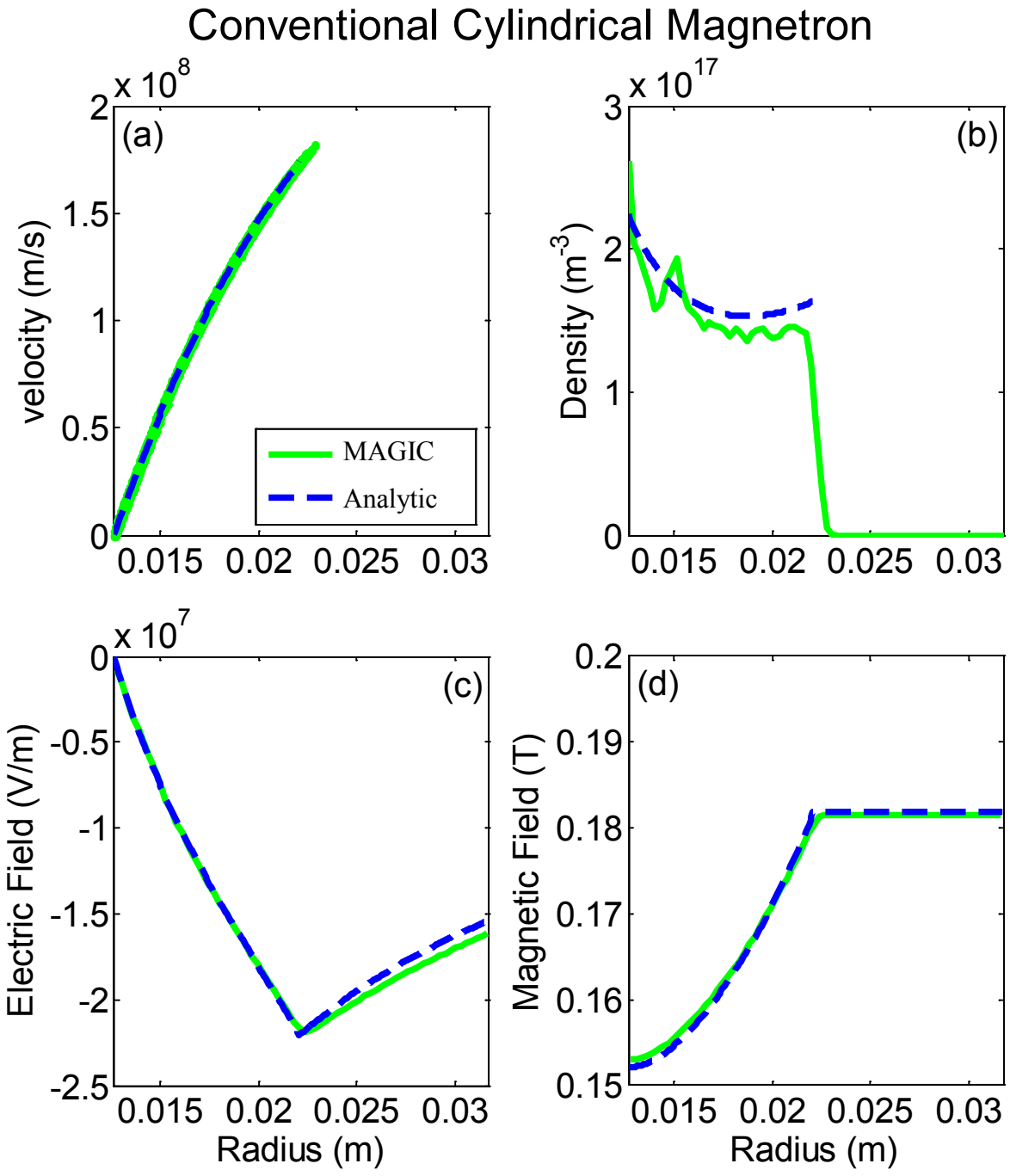

Figure 2.7: The equilibrium velocity (a), density (b), electric field (c), and magnetic field (d) for both the analytic Brillouin flow model and MAGIC PIC simulations for the 6 vane UM relativistic magnetron operated conventionally at 300kV and 0.175 T.

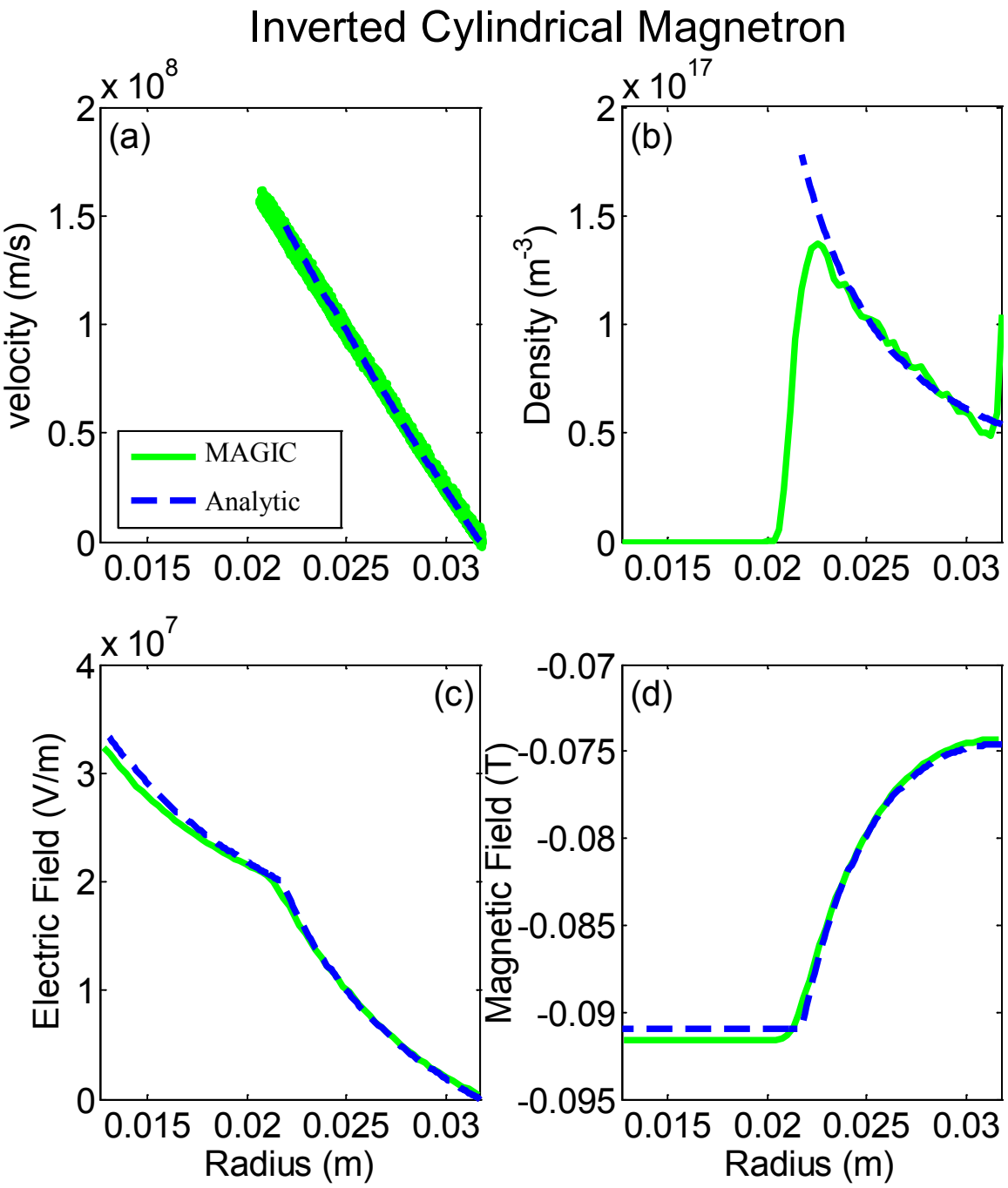

Figure 2.8: The equilibrium velocity (a), density (b), electric field (c), and magnetic field (d) for both the analytic Brillouin flow model and MAGIC PIC simulations for the 6 vane UM relativistic magnetron operated in the inverted configuration at -300kV and -0.083 T.

The cylindrical systems also show a maximum β around 0.5, and their velocity, electric field, and magnetic field trends are very similar to the planar case. The biggest influence of the cylindrical geometry can be seen in the density plots. For the inverted magnetron (Figure 2.8b), the density increases by more than a factor of two over the width of the hub, significantly more than the roughly 20% increase in the planar geometry. The electron density in the conventional magnetron (Figure 2.7b) initially decreases away from the cathode, but increases slightly near the edge of the hub. One factor for these behaviors is that the density increases with magnetic field, which grows in strength away from the cathode. Another factor is that in the inverted case, the radius decreases away from the cathode, so the overall area for the electrons is smaller, resulting in greatly increased density [c.f. Eq. (2.13)]. The conventional case is the opposite, the electrons have more room to spread out as they approach the hub, so density decreases. However, density is also increasing with magnetic field and these competing effects cause the slope of the density profile to change signs in Figure 2.7b. The density profile for the single particle cycloidal orbit model is substantially different than the simulation and the Brillouin flow model. The electrons have zero velocity normal to the cathode at the top of their orbit (the edge of the Brillouin flow), so by current conservation, the density must be infinite at that point. Under the assumption that the electrons have no initial velocity, the density must also be infinite at the cathode surface. Palevski's simulations showed the fairly constant density profile associated with the Brillouin flow, instead (Figure 1.9).

In Figure 2.6 through Figure 2.8, the solid green lines and the dashed blue lines show comparison between MAGIC simulations with the idealized analytic formulation of Brillouin flow. For all three geometries, the electric and magnetic fields agree quite well with the numeric results obtained from the analytic theory. The velocity also shows good agreement, although the line extends past the Brillouin hub in the MAGIC simulation. The reason for this is that the simulation electron velocity is plotted at every location in which there are electrons, which includes the trailing region after the hub height. The electron density in the simulations drops off rapidly at the hub, but does not go to zero immediately. It also includes significantly more noise than the other plots, due to a combination of resolution (particle number and cell size) and continuous emission of electrons from the cathode. Once a threshold electric field is reached at the cathode, electrons are emitted, even if the field drops below the threshold later in time. In addition, there is a microsheath at the cathode, which is also due to the continuous electron emission [21] and may

be responsible for the pattern seen in Figure 2.6b. Despite these differences, the slope and magnitude of the simulation density is very similar to that of the analytic formulation. The idealized Brillouin flow can be derived analytically and in a transparent manner. It illustrates the physics and scaling, whereas simulation is closer to reality because of the statistical fluctuations. This clearly manifests in the sharp discontinuity in density at the Brillouin hub height for the analytical results, while the simulation results show a steep drop-off. Davidson studied the effect of this slope in Ch. 8 of [26], but that will not be covered here except to say that the question is complex and requires additional study in light of what is presented in this thesis. Despite these differences, there is very good agreement between the analytical results and the simulations for all the geometries tested here.

2.5 Application of the Cylindrical Buneman-Hartree (BH) Condition to Relativistic Magnetrons

The B-H condition for Brillouin flow requires a matching of $\beta(\bar{r}_b)$ of the electrons and RF wave at the Brillouin hub height $\bar{r}_b$. Thus, we may fix the velocity of the electrons at the top of the hub which fixes the value of $\bar{\chi}(\bar{r}_b)$ according to Eq. (2.35). We next vary $\bar{\kappa}$ from which we obtain the $\bar{V}$ vs. $\bar{B}$ curve from Eqs. (2.48) and (2.49) for the mode under consideration, which is the Buneman-Hartree condition shown in Figure 2.9 and Figure 2.10. For a cylindrical magnetron, the synchronism condition between the mode's phase velocity and the electron flow velocity, both evaluated at the top of the Brillouin hub, does not yield the same B-H condition as the single particle model [25]. The operating regime of magnetrons lies between the Hull cutoff and the Buneman-Hartree conditions in Figure 2.9 and Figure 2.10.

Experimental and simulation results support the Brillouin flow derivation of the B-H condition. For the conventional magnetrons, MELBA shows operation outside the range of the single particle prediction, as shown in Figure 2.9. Many of the π-mode shots, and all of the 2π/3-mode shots can only be explained by the Brillouin flow model which predicts a much wider range of operation. For the inverted configuration, the paper by Flemming et. al. [56] shows simulation results for an inverted magnetron. Figure 2.10 overlays the Brillouin flow model onto those results. There are two single particle B-H lines. The one in black is from the original paper and was derived by the method outlined in the paper and the one in green is found from Eq. (1.11) and overlaid on top of the black line as a check. We can see that simulations failed to oscillate despite being within

the single particle B-H line. The Brillouin B-H condition, on the other hand, shows a much more restricted range of operation in Figure 2.10. The simulation results that failed to oscillate and are below the Hull cutoff (the last four triangles in the figure) indeed lie outside the region of oscillation according to Brillouin flow B-H condition. Overall, both figures support the idea that the Brillouin flow B-H condition is needed to explain magnetron operation, which lends support to the idea that the Brillouin flow represents the dominant equilibrium electron motion.

There are two reasons for the difference between the single particle and Brillouin flow model for the B-H condition. First, in a cylindrical magnetron, the Brillouin flow velocity is no longer the E×B drift, as the centrifugal force needs to be accounted for in Eq. (2.25). Second, if the mode's phase velocity *at the anode* is v_{ph}, its phase velocity *at the top of the Brillouin hub* is modified to $v_{ph}(r_b/r_a)$ because of the cylindrical geometry. For these two reasons, setting $\beta_0 = \beta_{ph}(\bar{r}_b)$ in Eq. (2.40) does not make it equivalent to the conventional B-H condition. *Thus, the B-H condition is very different between the Brillouin flow model and the single particle model for a cylindrical magnetron.*

The B-H condition for Brillouin flow for conventional magnetrons (Figure 2.9) allows for a much greater range of operations than the single particle prediction. The reduced phase velocity in a conventional magnetron means that the required electron velocity at the top of the Brillouin hub is also reduced. The electron velocity is still fairly proportional to E/B, so a reduction means that the voltage can decrease at a given magnetic field and still satisfy the synchronism condition. Inverted magnetrons see a higher phase velocity, since $r_b > r_a$. This leads to a *reduced range* of operations, not just when compared to conventional Brillouin flow, but also compared to the single particle orbit model.

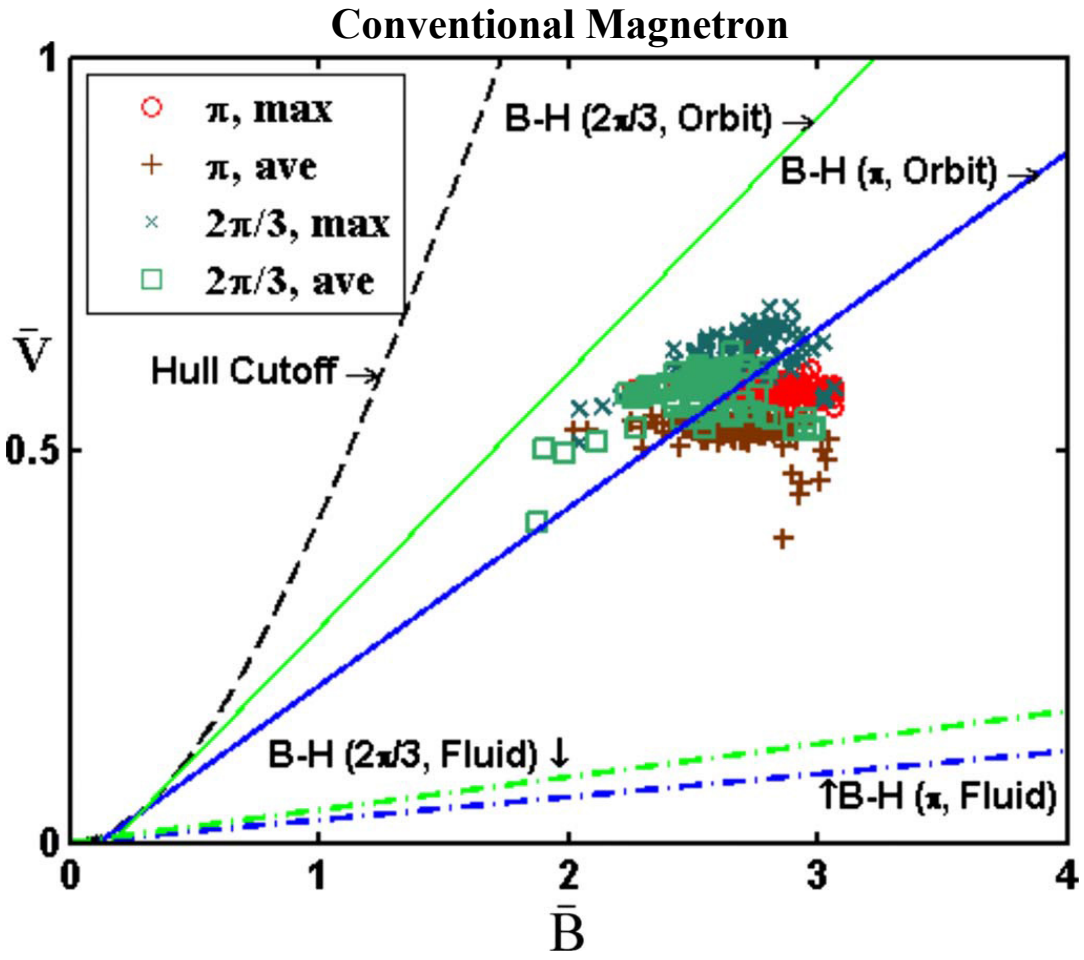

Figure 2.9: A normalized operational curve for MELBA, showing the Hull cutoff and the B-H conditions for both single particle (labeled "orbit") and Brillouin flow (labeled "fluid") for π and 2π/3 modes superimposed on the scatter data representing shots that produced microwaves. The data show the maximum and average values for normalized voltage and magnetic field strength recorded during magnetron operation.

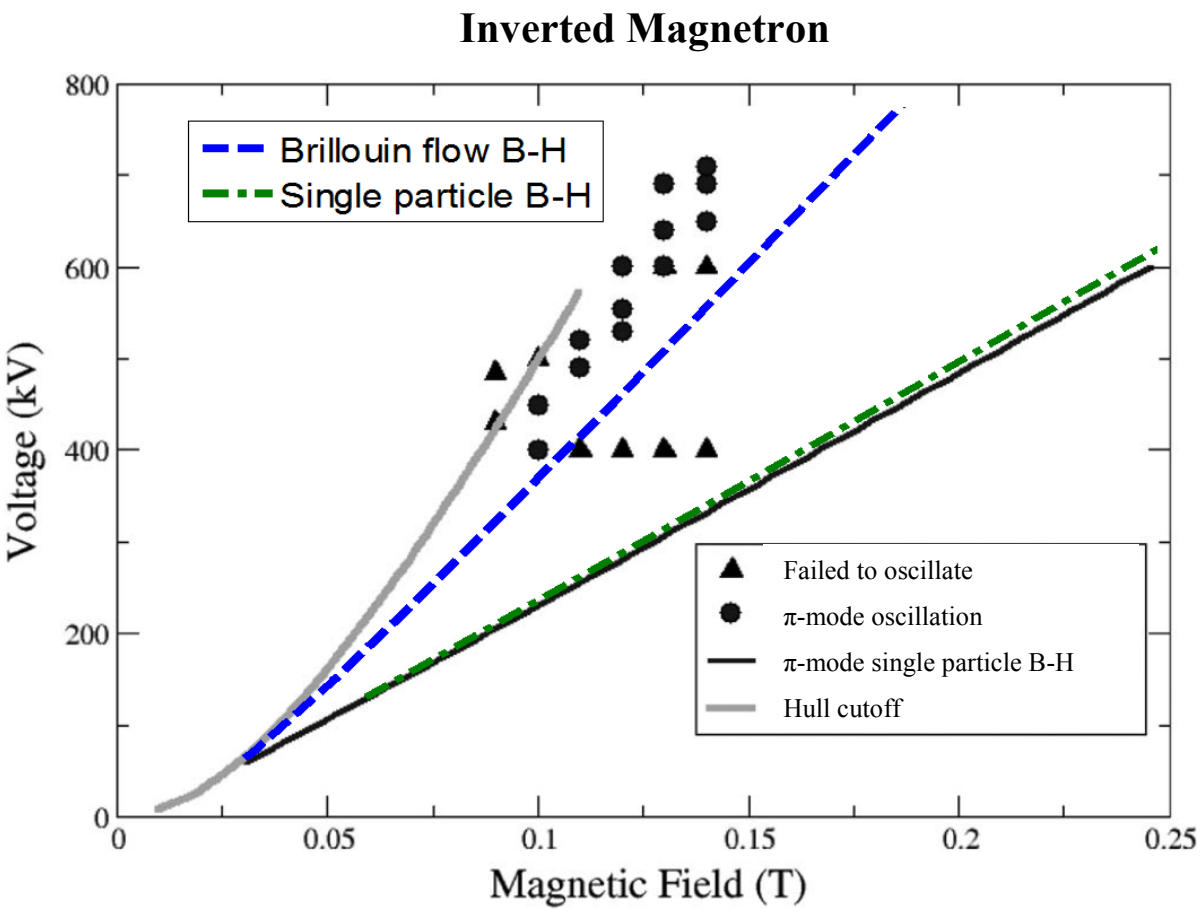

Figure 2.10: Figure 12 from ref [56] with the Brillouin flow B-H condition for π mode superimposed. The discrete points are PIC simulations. Triangles represent a simulation that failed to oscillate, circles represent simulations that oscillate in π mode.

2.6 Concluding Remarks

In this chapter, properties required to perform the stability analysis in later chapters were obtained for planar and cylindrical Brillouin flow. They were derived from very simple conditions, requiring that each electron in the Brillouin flow has a zero total energy [Eq. (2.24)] and starts on the cathode with zero initial velocity. The cycloidal orbits of such an electron, *under the space charge limited condition*, are known as the Slater orbits [17]. The Brillouin flow solution then corresponds to the N^{th} order Slater orbit with N approaching infinity (N designates the number of cycloidal "hops" an electron undergoes, from its birthplace on the cathode to its maximum excursion in the diode, before returning to the cathode, see Section 1.2.2). In this scenario, the Hull cutoff like condition, Eq. (2.39), and the Buneman-Hartree like condition, Eq. (2.40), simply state conservation of energy and of canonical momentum for these electrons.

If every electron released from the cathode has a zero initial velocity and if these electrons eventually establish a concentric laminar flow, then such a flow *necessarily* satisfies the space-charge-limited condition (SLC), E = 0, on the cathode surface according to Eq. (2.25). This laminar flow, of course, is the Brillouin flow. Thus, strictly laminar, concentric electron flows of electrons originating from the cathode must satisfy SLC. Careful numerical simulations have shown, however, that SLC is never *strictly* achieved in a magnetically insulated crossed-field gap, whether the voltage is relativistic [57] or nonrelativistic [18], [21], [22]. Thus, the Brillouin flow model provides only an approximation of the natural state of crossed-field flows [17]–[19], [58]. Cycloidal orbits resembling lower order Slater orbits have also been reported in simulation studies [59], [60]. The adequacy of the cycloidal orbit model [61] vs the Brillouin flow model [51] has also been raised in the study of ion beam diodes. Here we show that the Buneman-Hartree condition based on the Brillouin flow model provides a more adequate interpretation than that based on the single particle model for the interpretation of relativistic magnetron experiments and simulation.

Equations (2.39) and (2.40) only give the constraint on the Brillouin flow's scalar and vector potentials, which still need to be solved. Given the AK gap voltage, the total magnetic flux within the gap, the cathode and anode radius r_c and r_a, the Brillouin flow solution is completely determined, including the complete solution v(r), and the Brillouin hub height r_b. This solution, covered in detail in section 2.3.2, was given in Davidson *et al.* [50] and in Appendix B of Lau *et al.* [25]. Davidson *et al.* [50] did not consider the Buneman-Hartree condition according to the Brillouin flow model.

The governing equations (2.24)–(2.28) are independent of the surface electric field. They are valid even in the presence of background ions whose distribution is axisymmetric. This means that the Hull cutoff depends only on the end conditions, and does not depend on the details of the charge distribution within the gap as long as the distribution is strictly one-dimensional. Deviation from one-dimensional distribution can defeat magnetic insulation. The Buneman-Hartree-like condition (2.40) and the Hull cutoff-like condition (2.39), derived solely from Eqs. (2.24)–(2.28) (or in dimensionless form from Eqs. (2.31)–(2.34)), then seem to be applicable even if there is an arbitrary, axisymmetric distribution of ions. However, the presence of axisymmetric ion distribution would prevent the establishment of the Brillouin flow [62], even in the approximate sense described two paragraphs above. To see this, consider the extreme case where there is a sheet

of positive ions with significant charge lying just above the cathode. An electron released from the cathode with a zero initial velocity will be accelerated by this ion sheet, and this electron would exit the ion sheet with a large positive radial velocity [62]. This large radial velocity rules out the establishment of the Brillouin flow (or Brillouin-like flow). Note further that this ion sheet invalidates the *local* relation, Eq. (2.39), in particular at the location of the ion sheet.

CHAPTER 3

Stability of Smooth-bore Planar, Conventional, and Inverted Magnetrons

3.1 Introduction

Inverted magnetrons [63] have traditionally shown faster startup than their conventional counterparts. In particular, simulations of the recirculating planar magnetron [11]–[14] show bunching occurred quickly in the recirculating bends if the device was in an inverted configuration. In the inverted magnetron configuration, a rotating electron is subject to the negative mass effect (covered in section 1.3.2), so that a *thin* axis-encircling electron layer is subject to the negative mass instability [38], [39]. In such a thin electron layer, the negative mass instability is the dominant instability, and the diocotron instability is the residual instability which becomes dominant in the planar limit, in which case the negative mass effect is absent [38].

Unanswered is the negative mass effect in a rotating Brillouin flow, whose electron hub is not "thin" as shown in Figure 2.4 and Figure 2.5. Moreover, the very significant velocity shear in the Brillouin flow intrinsically represents a large velocity spread, which tends to stabilize the negative mass instability on a thin electron beam. Since the Brillouin flow is the prevalent state in a crossed-field geometry [17], [18], as is evident in Figure 1.9 and Figure 2.4 though Figure 2.8, we systematically study its stability in conventional, planar, and inverted magnetron configurations. To investigate the intrinsic negative mass effects in Brillouin flows, we consider only the smooth-bore magnetron in this chapter. Much of the emphasis is on the electrostatic modes, while fully electromagnetic and relativistic treatments are considered in Section 3.4.

As indicated in Figure 1.11, negative mass instability on a thin electron beam occurs when $h > -\beta_0^2/2$ [5], [38], [39] where $h = erE_0/mv_0^2\gamma_0^3$, E_0 is the radial electric field, $v_0 = \omega_0 r$ is the angular velocity of the rotating electron, $\beta_0 = v_0/c$ and $\gamma_0 = (1-\beta_0^2)^{-1/2}$. As presented in Eq. (1.16), $\gamma_0^2 h$ is the fraction of the electric force that provides the centripetal acceleration for the

rotation of the electrons. Thus negative mass instability always occurs if the radial electric field E_0 is positive, as in an inverted magnetron configuration (see Figure 1.11). An electron in the conventional magnetron configuration would exhibit a positive mass behavior in general. Since Brillouin flow has a substantial thickness (relative to the AK gap), and has very significant velocity shear within the flow as indicated above, it is unclear if the notion of negative mass instability applies. It should be stressed that the Brillouin flow, because of its strong velocity shear, is itself subjected to a diocotron-like instability, which is the same instability mechanism as the diocotron instability applied to a thick beam instead of a thin beam. The stability of Brillouin flow in the planar magnetron and the conventional magnetron configuration has been studied extensively by Buneman [34], Swegle [64], Antonsen [35], Davidson [26], [43], [65], [66], and Tsang [67]. There are even experiments testing microwave production of smooth-bore magnetrons [68]. The geometries they consider exclude negative mass behavior. They include only positive mass behavior.

In order to isolate the effects of the negative mass instability from the velocity shear which is always present in the Brillouin flow, the planar case, which is known to exclude negative mass effects, is briefly revisited first. A comparison between the growth rates of planar, conventional, and inverted magnetrons in the non-relativistic regime then illustrates the positive or negative mass effects on the shear flow instability. We will show that the inverted magnetron has a higher instability growth rate than the planar magnetron, while the conventional magnetron has the lowest growth rate.

In Section 3.2, we summarize the results for the stability of the planar Brillouin flow. In Section 3.3, we compare the Brillouin flow stability in the planar, conventional and inverted magnetron configurations. We also consider the azimuthal modes that would sequentially be excited as the gap voltage is ramped up. In Section 3.4, we include the results on relativistic and electromagnetic effects (still for the smooth-bore configuration).

3.2 Stability of Planar Brillouin Flow

The equilibrium planar Brillouin flow was covered in Chapter 2, with geometry shown in figure 2.1b (redrawn here as Figure 3.1 for convenience). In equilibrium, a voltage V is imposed across the anode-cathode (AK) gap with gap separation D. The Brillouin flow region is $0 < x < x_b$. The vacuum region has a width $W = D - x_b$.

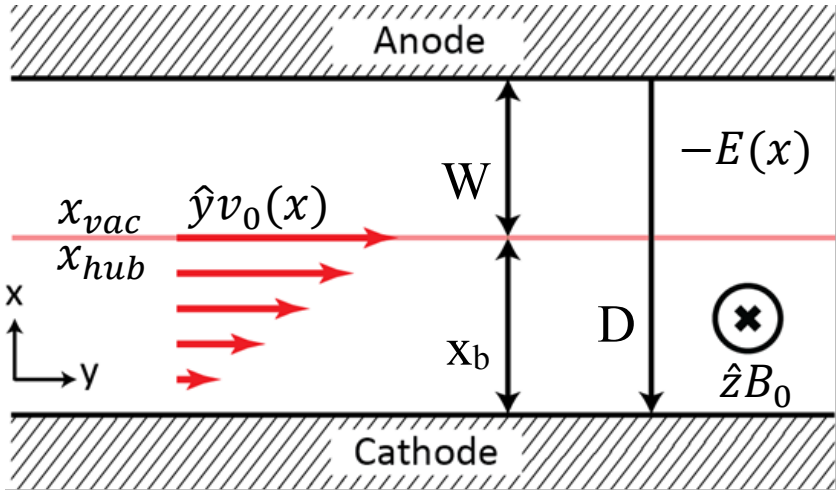

Figure 3.1: Planar Brillouin flow, including the location of x_{vac} and x_{hub}, which are on the vacuum edge and electron edge of the Brillouin hub, respectivly.

The stability of planar Brillouin flow under the electrostatic assumption is well documented [26]. For the solutions presented in this section, all quantities are assumed to be of the form $\psi(x,y,t) = \psi_0(x) + \psi_1(x)e^{j(\omega t - k_y y)}$ where a subscript 0 is the equilibrium quantity and subscript 1 denotes the perturbation quantity. Subscripts x and y denote the direction of the perturbation quantity; for example, v_{1y} is the perturbation velocity in the ŷ direction. Prime variables are derivatives with respect to x (e.g. $\psi' = \partial\psi/\partial x$). The linearized equations are the force equation within the Brillouin hub, $0 < x < x_b$, (broken into x̂ and ŷ components),

$$j\Omega v_{1y} + (v_0' - \omega_c)v_{1x} = -\frac{e}{m}E_{1y}, \qquad j\Omega v_{1x} + \omega_c v_{1y} = -\frac{e}{m}E_{1x}, \tag{3.1}$$

the continuity equation,

$$n_1 = \frac{n_0}{\Omega}\left(k_y v_{1y} + j\frac{\partial v_{1x}}{\partial x}\right) + j\frac{v_{1x}}{\Omega}\frac{\partial n_0}{\partial x}, \tag{3.2}$$

and the Poisson's equation,

$$\nabla^2\phi_1 = \frac{en_1}{\epsilon_0}, \tag{3.3}$$

where $\Omega = \omega - k_y v_0$, and

$$E_{1y} = jk_y\phi_1, \qquad E_{1x} = -\frac{\partial\phi_1}{\partial x}. \tag{3.4}$$

The result is a governing equation for the electrostatic potential ϕ_1 based on the equilibrium flow properties,

$$\phi_1'' - k_y^2\phi_1 = \frac{\omega_p^2}{D\Omega}\left[\Omega\phi_1'' - k_y^2\Omega\phi_1 - \frac{D'}{D}\left(\Omega\phi_1 + k_y\omega_c\phi_1\right) + \frac{n_0'}{n_0}\left(\Omega\phi_1' + k_y\omega_c\phi_1\right)\right], \tag{3.5}$$

where $D = \Omega^2 + \omega_c(v_0' - \omega_c)$. The eigenvalue, ω, is determined from the boundary condition $\phi_1 = 0$ at the cathode ($x = 0$) and the anode ($x = D$).

The form of the equilibrium Brillouin flow, given in Chapter 2, can be used to greatly simplify Eq. (3.5). In particular, within the Brillouin flow, [c.f. Eqs. (1.8a,b)]

$$v_0' = \omega_c, \qquad n_0' = 0, \qquad \omega_c^2 = \omega_p^2. \tag{3.6}$$

The final form of the governing equation, along with the vacuum boundary equation and jump condition will be presented next in dimensionless form using the following variables,

$$\bar{x} = xk_y, \qquad \bar{\omega} = \frac{\omega}{|\omega_c|} \equiv \bar{\omega}_r - i\bar{\omega}_i, \qquad \bar{\Omega} = \bar{\omega} - \bar{x}, \tag{3.7}$$

so that $\bar{\omega}_i$ is the normalized growth rate. The governing equation, with the planar equilibrium profiles applied, becomes

$$\frac{\partial^2\phi_1}{\partial\bar{x}^2} = \phi_1 + \frac{2}{\bar{\Omega}^3 - \bar{\Omega}}\left(\frac{\partial\phi_1}{\partial\bar{x}} + \frac{\phi_1}{\bar{\Omega}}\right). \tag{3.8}$$

The vacuum boundary condition at the Brillouin hub is derived from Poisson's equation in the vacuum region, along with the boundary condition that ϕ_1 is zero at the anode. This boundary condition is simply the requirement that there is no tangential electric field at a conductor. Since according to Eq. (3.4), $\phi_1 \propto E_{1y}$, we have $\phi_1 = C\sinh\left[k_y(x - D)\right]$, and $x = x_{vac}$ (the x position just outside the Brillouin hub, x_b^+),

$$\left.\frac{1}{\phi_1}\frac{\partial\phi_1}{\partial\bar{x}}\right|_{x_{vac}} = -\coth(\bar{W}). \tag{3.9}$$

The jump condition is an integration of Eq. (3.5) across the edge of the Brillouin hub. The velocity and ϕ_1 are continuous across the hub, but the density and ϕ_1' are not. The jump condition is

$$\left.\frac{1}{\phi_1}\frac{\partial\phi_1}{\partial\bar{x}}\right|_{x_{vac}} = \left.\frac{1}{\phi_1}\frac{\partial\phi_1}{\partial\bar{x}}\right|_{x_{hub}} - \left.\frac{1}{\bar{\Omega}^2}\left(\frac{1}{\phi_1}\frac{\partial\phi_1}{\partial\bar{x}} + \frac{1}{\bar{\Omega}}\right)\right|_{x_{hub}}, \tag{3.10}$$

where x_{hub} denotes the x position just inside the Brillouin hub, x_b^-. The process for finding the eigenvalue solution to Eqs. (3.8) - (3.10) uses a root-finding scheme based on an initial estimate. It is possible to determine how many (if any) roots are in a given complex frequency range by

using a Nyquist diagram (also known as a Nyquist plot). The principle behind the Nyquist diagram is that it is possible to map a contour in the complex plane to a function (by Cauchy's argument principle) and that function will enclose the origin, (0,0), a number of times equal to the zeros of the function minus the poles of the function [69]. Nyquist diagrams have been used in this thesis to ensure that the unstable eigenvalue solutions that are presented are the only solutions within a given frequency range, typically extending from the root an order of magnitude in either direction for the real part of the frequency ($0.1\omega_r - 10\omega_r$) and 2 orders of magnitude for the imaginary part ($0.01\omega_i - 100\omega_i$).[1]

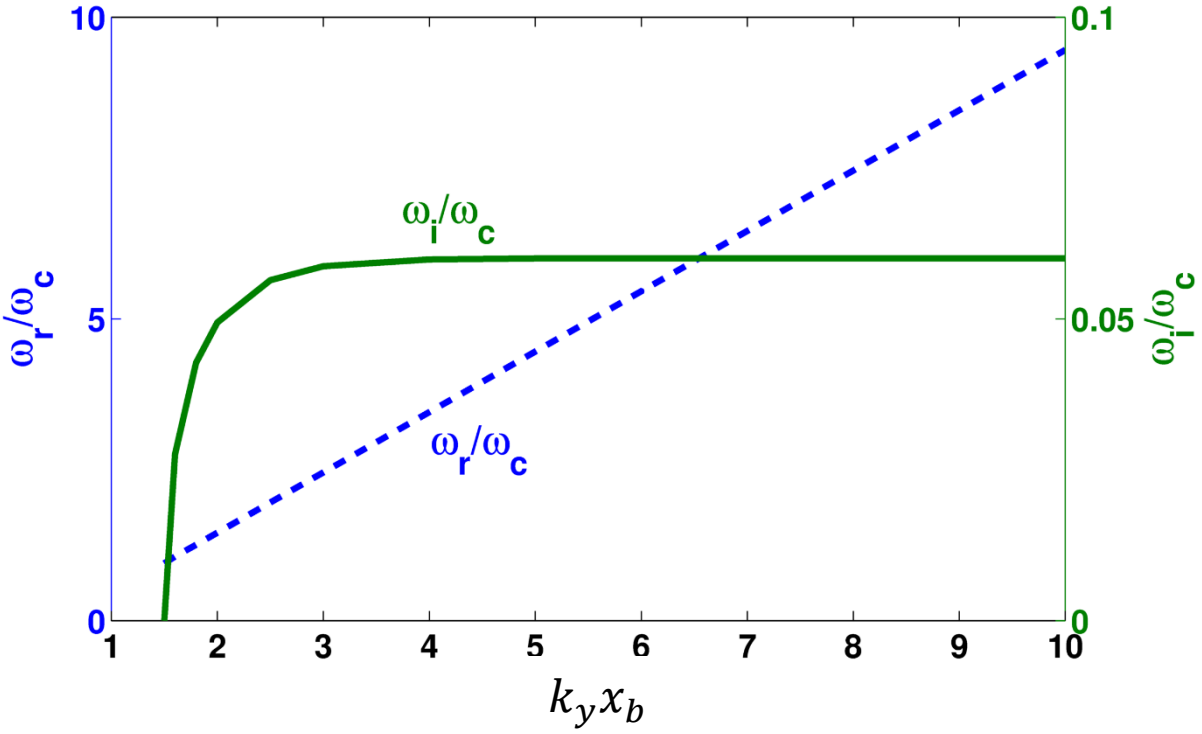

Figure 3.2: Planar magnetron eigenvalue solutions for the case where $\bar{x}_b$ = $\bar{W}$. This condition completely defines the normalized variables in the eigenvalue problem.

The eigenvalue solution to the above set of equations is shown in Figure 3.2 for different wave numbers (through $\bar{x}_b = k_y x_b$) for the case where $\bar{x}_b = \bar{W}$. This case of 50% fill represents intermediate magnetic insulation, and is also common for relativistic magnetrons. The distance between the hub and the anode, $\bar{W}$, enters only in the vacuum boundary condition Eq. (3.9) as $coth(\bar{W})$ which is roughly a constant (=1) over the entire range of $\bar{W}$ for the chosen parameters.

[1] If $\omega_i \to 0$, the method for determining validity of an eigenfrequency is to produce a contour plot of the absolute value of the function for a grid of values for ω_r and ω_i. A visual check can then determine if a root exists.

The eigenvalue solution results in a complex frequency. The real part of the frequency is the oscillation frequency. The imaginary part of the frequency is the growth rate. If there is no imaginary part, then the system is stable and initial perturbations will not form bunches. The real part of the frequency increases linearly with k_y (i.e., with $\bar{x}_b$). We found that, for large values of $\bar{x}_b$, $\bar{x}_b - \bar{\omega}_r = 0.55$ and $\bar{\omega}_i = 0.06$, a result proven by Buneman, Levy, and Linson [34] and cited in Eq. (1.15). The real part of the frequency corresponds to a synchronous layer within the Brillouin hub. The system is stable below a certain threshold, namely, there is no instability if the real part of the frequency is less than the electron cyclotron frequency [64]. In this case, the diocotron-like instability would likely not be responsible for magnetron startup.

3.3 Stability of Cylindrical Brillouin Flow in Conventional and Inverted Magnetrons

We use r_a, r_b and r_c to designate, respectively, the anode radius, the Brillouin hub radius, and the cathode radius in both conventional magnetron and inverted magnetron configurations, consistent with the previous chapter. Figure 2.1b shows the conventional geometry, redrawn here as Figure 3.3. The equilibrium profiles for the density and velocity are given in Eqs. (2.11) - (2.13).

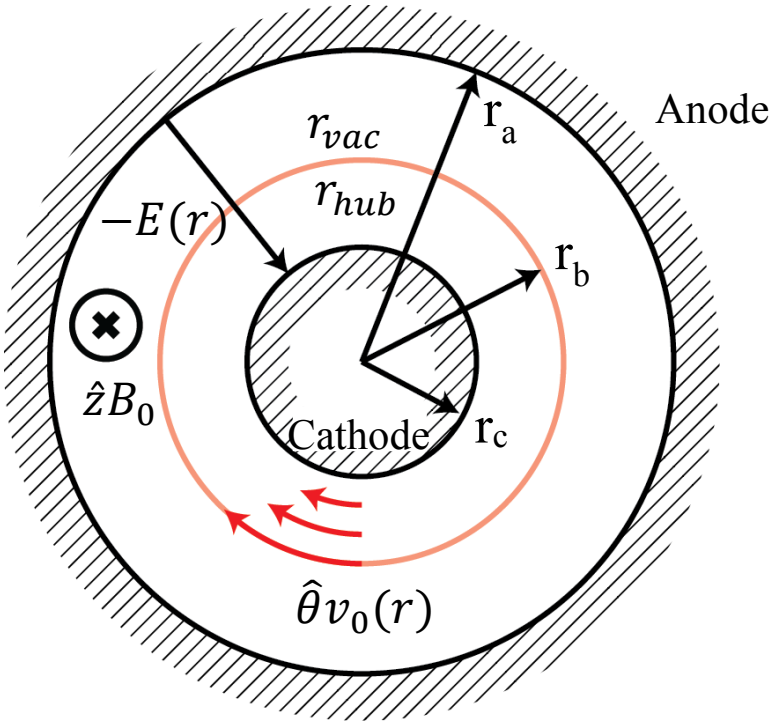

Figure 3.3: Conventional cylindrical Brillouin flow, including the location of r_{vac} and r_{hub}, which are on the vacuum edge and electron edge of the Brillouin hub, respectively.

Cylindrical Brillouin flow, like the planar version, has the property $\omega_p^2 = \omega_c^2$ at the cathode, though since the density varies radially, this does not hold true for the rest of the Brillouin hub. The following dimensionless equations are applicable to both the conventional and inverted magnetron configurations, where $+\bar{\omega}$ $(-\bar{\omega})$ is used in the equation for $\bar{\Omega}$ in the conventional (inverted) magnetron configuration, and l (l>0) is the azimuthal mode number,

$$\bar{r} = \frac{r}{r_c}, \qquad \bar{\omega} = \frac{\omega}{|\omega_c|} \equiv \bar{\omega}_r - i\bar{\omega}_i, \qquad \bar{\Omega} = \pm\bar{\omega} - \frac{1}{2}l\left(1 - \frac{1}{\bar{r}^2}\right), \tag{3.11}$$

$$\bar{\omega}_p^2 = \frac{1}{2}\left(1 + \frac{1}{\bar{r}^4}\right).$$

Note that $\Omega = \omega - lv_\theta(r)/r$ is the dimensional Dopplar shifted frequency, and $\bar{\Omega} = \Omega/|\omega_c|$.

As with the planar derivation in Section 3.2, the linearized force law, continuity equations, and Poisson's equation are used to find the governing equation within the hub. Similar to the derivation for the planar Brillouin flow given in Section 3.2 , the governing equation reads [26], [70],

$$\phi_1'' = \frac{l^2}{\bar{r}^2}\phi_1 - \frac{\phi_1'}{\bar{r}} + \frac{2l\bar{\omega}_p^2}{\bar{\Omega}\left(\bar{\Omega}^2 - \bar{\omega}_p^2\right)}\left[\frac{\phi_1'}{\bar{r}^3} + \left(\frac{l}{\bar{r}^6\bar{\Omega}} - \frac{1}{\bar{r}^4}\right)\phi_1\right] \tag{3.12}$$

$$-\frac{2}{\left(\bar{\Omega}^2 - \bar{\omega}_p^2\right)}\left(\frac{\phi_1'}{\bar{r}^5} + \frac{l\phi_1}{\bar{r}^8\bar{\Omega}}\right).$$

The boundary condition in the vacuum region outside the Brillouin hub is,

$$\left.\frac{\phi_1'}{\phi_1}\right|_{r_{vac}} = \frac{l}{\bar{r}}\frac{\left[\frac{\bar{r}_b^{\,l}}{\bar{r}_a^{\,l}} + \frac{\bar{r}_a^{\,l}}{\bar{r}_b^{\,l}}\right]}{\left[\frac{\bar{r}_b^{\,l}}{\bar{r}_a^{\,l}} - \frac{\bar{r}_a^{\,l}}{\bar{r}_b^{\,l}}\right]}, \tag{3.13}$$

and the jump condition is,

$$\left.\frac{\phi_1'}{\phi_1}\right|_{r_{vac}} = \left.\frac{\phi_1'}{\phi_1}\right|_{r_{hub}} - \left.\frac{\bar{\omega}_p^2}{\bar{\Omega}^2}\left(\frac{\phi_1'}{\phi_1} + \frac{l}{\bar{r}^3\bar{\Omega}}\right)\right|_{r_{hub}}. \tag{3.14}$$

where r_{vac} denotes the radius of the vacuum region just outside the Brillouin hub and r_{hub} denotes the radius just inside the Brillouin hub (Figure 3.3).

Since Eqs. (3.11) - (3.14) are non-dimensional, we set the inner radius at 1m, Brillouin hub at 1.5m, and the outer radius at 2m in the numerical examples. The ratio between the radii is the important factor. The real part of the frequency shown in Figure 3.4 for both conventional and inverted magnetron scales fairly linearly with the mode number (l), as was the case for the planar

magnetron (Figure 3.2). Additionally, the threshold for system stability also occurs at about the point the real frequency is equal to the cyclotron frequency. The imaginary part of the frequency shows a similar trend to the planar system, except that it decreases after reaching a peak instead of approaching an asymptote. Note the large contrast in the growth rate between the conventional magnetron (Figure 3.4a) and the inverted magnetron (Figure 3.4b) in this example. Figure 3.5 further shows this contrast.

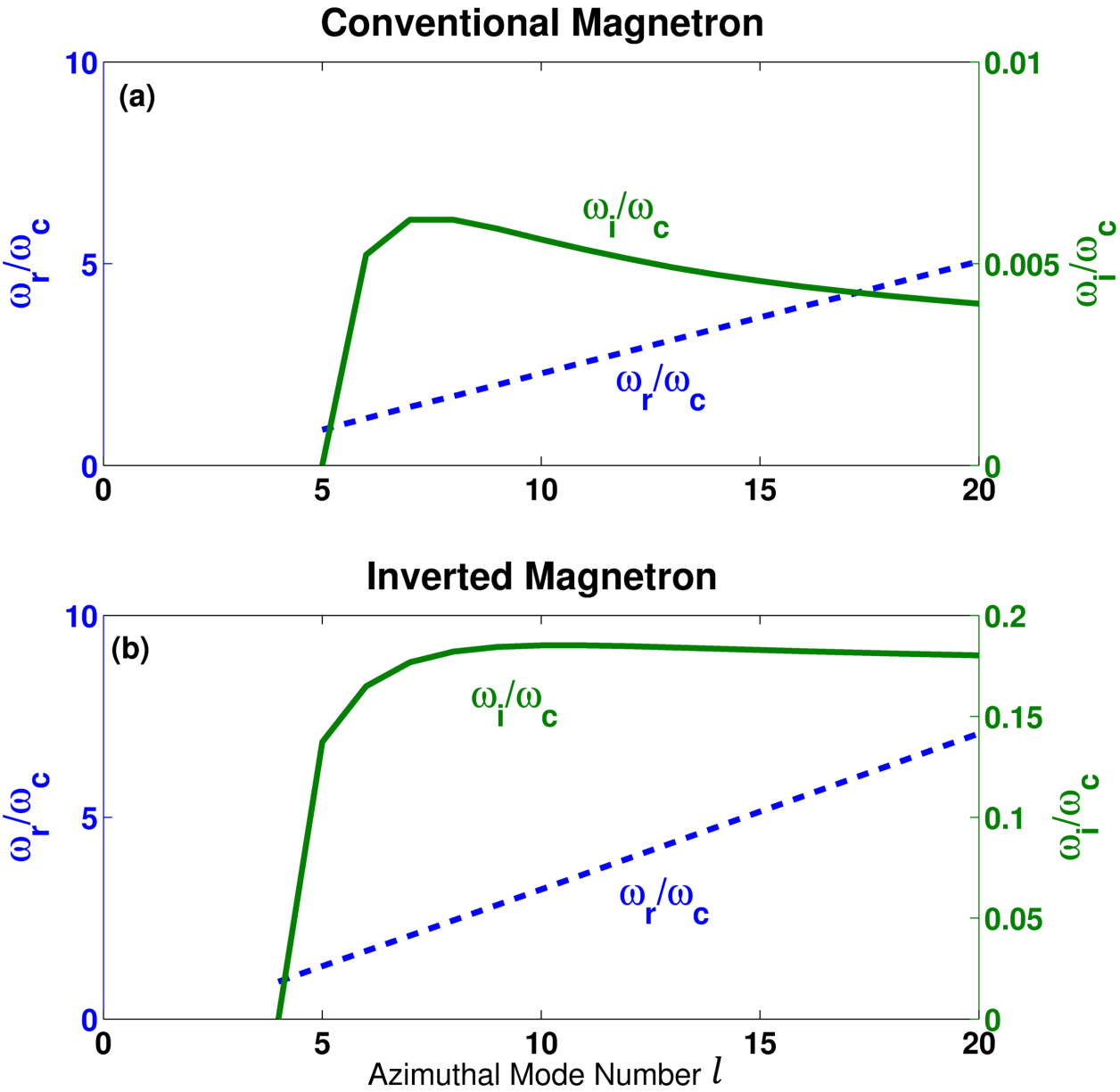

Figure 3.4: The eigenvalue solutions for the conventional (a) and inverted (b) magnetrons. The inner radius is 1m, the Brillouin hub radius is 1.5m, and the outer radius is 2m [70].

The normalized growth rates shown in Figure 3.5 are found from solving the eigenvalue equation for the planar and cylindrical governing equations at different cathode to anode radii ratios [70]. The planar geometry is the limit where cathode radius and anode radius go to infinity, so the ratio is 1. The AK gap separation is held at a constant of 1m, the Brillouin hub is at a constant 50% fill (0.5m from the anode and cathode), and the "bunch frequency" at the top of the hub (defined as lv_0/r_b for cylindrical and $k_y v_0$ for planar, where v_0 is the linear velocity of electrons at the top of the Brillouin hub) is held constant at $2*\omega_c$ while the anode and cathode radii are varied.

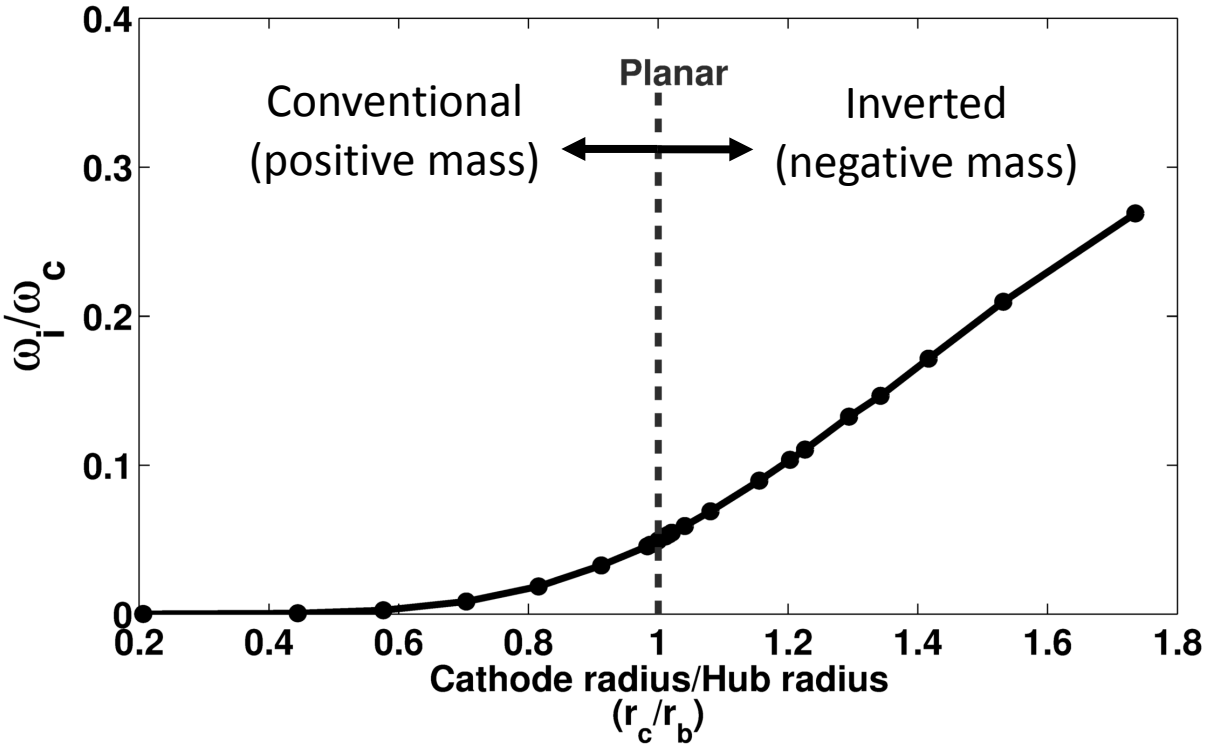

Figure 3.5: Normalized growth rate as a function of cathode radius to hub height for a constant AK gap width, hub height, and bunch frequency. The conventional, planar, and inverted magnetron corresponds to, respectively, $r_c/r_b < 1$, $r_c/r_b = 1$, $r_c/r_b > 1$ [70].

The inverted geometry shows an increase in instability strength as the ratio of r_c/r_b increases, starting from the planar ratio of 1. The conventional geometry stabilizes as r_c/r_b decreases from the planar ratio of 1 (Figure 3.5). The increase in r_c/r_b for the inverted geometry and decrease in r_c/r_b for the conventional geometry both correspond to a decrease in inner and outer radii for the magnetrons. This indicates that the inverted magnetron configuration destabilizes the intrinsic instability in the planar system, while the conventional magnetron

configuration stabilizes it. This is consistent with Figure 1.11, where the inverted magnetron shows negative mass behavior, whereas the conventional magnetron shows positive mass behavior.

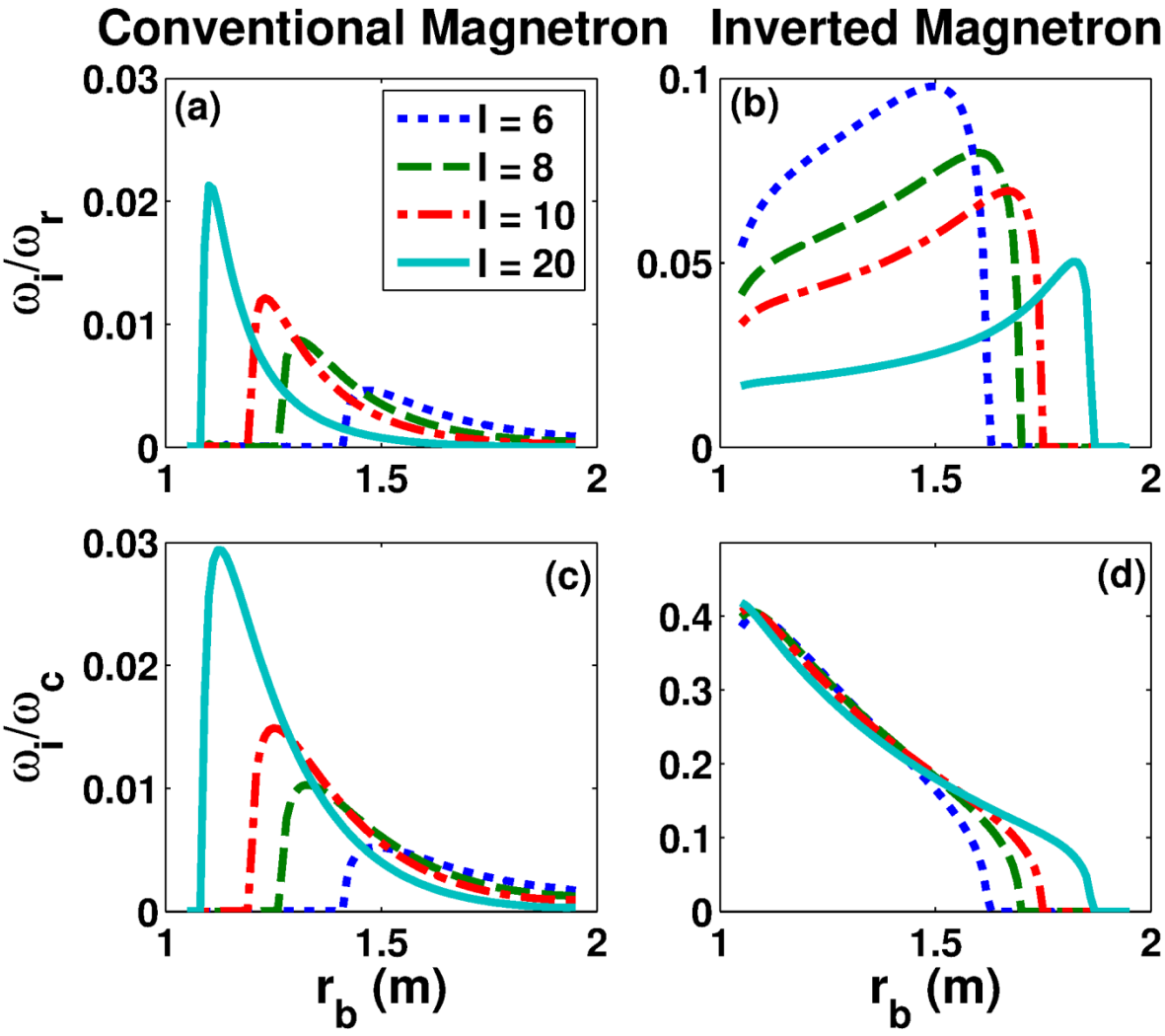

Figure 3.6: The ratio of ω_i/ω_r as a function of r_b for (a) conventional and (b) inverted magnetron. The ratio of ω_i/ω_c as a function of r_b for (c) conventional and (d) inverted magnetron. In all cases the inner and outer radii are held constant at 1m and 2m respectively. r_b increases as the gap voltage increases for (a) and (c), and decreases for (b) and (d) [70].

Having shown that that inverted magnetron is inherently more unstable than conventional magnetron, we now explore which modes start up first as the AK gap voltage of the smooth-bore magnetron is turned on, while the magnetic field remains constant. The turn-on is assumed to be sufficiently slow that the system is in a quasi-static equilibrium. As the voltage is ramped up, the Brillouin hub radius r_b increases in the conventional magnetron shown in Figure 3.6 (a) and (c), but decreases in the inverted magnetron configuration shown in Figure 3.6 (b) and (d). The growth

rate is normalized to the real part of the mode frequency in Figure 3.6 (a) and (b) and to the electron cyclotron frequency in Figure 3.6 (c) and (d). In the conventional magnetrons in Figure 3.6 (a) and (c), the higher order modes start up first, and with a higher growth rate than lower order modes. All of the modes lose strength rapidly as the Brillouin hub increases. For the inverted magnetrons in Figure 3.6 (b) and (d), the higher order modes also start up sooner than lower order modes, but they are weaker in that ω_i/ω_r is lower for high l. Additionally, all of the modes show an increase in $\bar{\omega}_i$ as the Brillouin hub increases.

3.4 Electromagnetic and Relativistic Effects

Including relativistic effects in a fully electromagnetic formulation, the perturbed fields are governed by the differential equation, Eq. (14) of Chernin and Lau [38], with the equilibrium profiles for $n_0(r), v_0(r), E_0(r)$, and $B_0(r)$ provided by the electromagnetic Brillouin hub equilibrium solution covered in Chapter 2. The governing equation, for $\phi = rE_{1\theta}$, is

$$r\frac{d}{dr}\left(r\tilde{A}\frac{d\phi}{dr}\right) + \tilde{C}\phi = 0, \tag{3.15}$$

where

$$\tilde{A} = \left[1 + \frac{\xi}{D\gamma_0^2}\right]/\Delta, \tag{3.16}$$

$$\tilde{C} = \frac{\omega}{\Omega}\left[\left(\frac{\Omega}{\omega} - \frac{1}{\gamma_0^2}\right)\frac{r}{\omega_0}\frac{\partial}{\partial r}\left[\frac{\omega_0\xi(1+h)}{\Delta D}\right] + \frac{2\beta_0^2\xi(1+h)}{\Delta D}\right] + \frac{\xi}{\Delta D\gamma_0^2}\left(\frac{\omega^2 r^2}{c^2} - l^2 - \xi\beta_0^2\right) + 1, \tag{3.17}$$

$$\Delta = \frac{\omega^2 r^2}{c^2} - l^2 + \frac{\xi}{D}\left(\frac{\Omega^2 r^2}{c^2}\right), \tag{3.18}$$

$$D = 1 - \frac{\xi}{\gamma_0^2} + \gamma_0^2 h^2 - \frac{\Omega^2}{\omega_0^2}, \tag{3.19}$$

and $\omega_0 = v_0/r$, $\Omega = \omega - l\omega_0$, $h = erE_0/mv_0^2\gamma_0^3$, $\xi = \omega_p^2/\omega_0^2\gamma_0$, and ω_p is the non-relativistic plasma frequency. We note that the value for h can approach infinity at the cathode, because the velocity and electric field go to zero when using L'Hôpital's rule. Based on the equilibrium profile definitions and rearranging variables, the vacuum boundary is

$$\left.\frac{\phi'}{\phi}\right|_{r_{vac}} = -\frac{p^2 r_b^2 - l^2}{pr_b^2}\left(\frac{CJ_l(pr_b) + Y_l(pr_b)}{CJ_l'(pr_b) + Y_l'(pr_b)}\right), \tag{3.20}$$

where $p = \omega/c$ and $C = -Y_l'(pr_a)/J_l'(pr_a)$. The electromagnetic eigenvalue solutions are found from matching the perturbed azimuthal electric fields in the vacuum region to those in the Brillouin hub. The jump condition across $r = r_b$, found from integrating Eq. (3.15), is

$$\left.\frac{\phi'}{\phi}\right|_{r_{vac}} = \frac{\tilde{A}(r_{hub})}{\tilde{A}(r_{vac})}\left.\frac{\phi'}{\phi}\right|_{r_{hub}} + \frac{1}{r_b\tilde{A}(r_{vac})}\frac{\omega}{\Omega}\left[\left(\frac{\Omega}{\omega} - \frac{1}{\gamma_0^2}\right)\frac{1}{\omega_0}\left[\frac{\omega_0\xi(1+h)}{D\Delta}\right]\right]_{r_{hub}}, \tag{3.21}$$

where r_{vac} (r_{hub}) denotes the radius just outside (inside) the Brillouin hub (Figure 3.3).

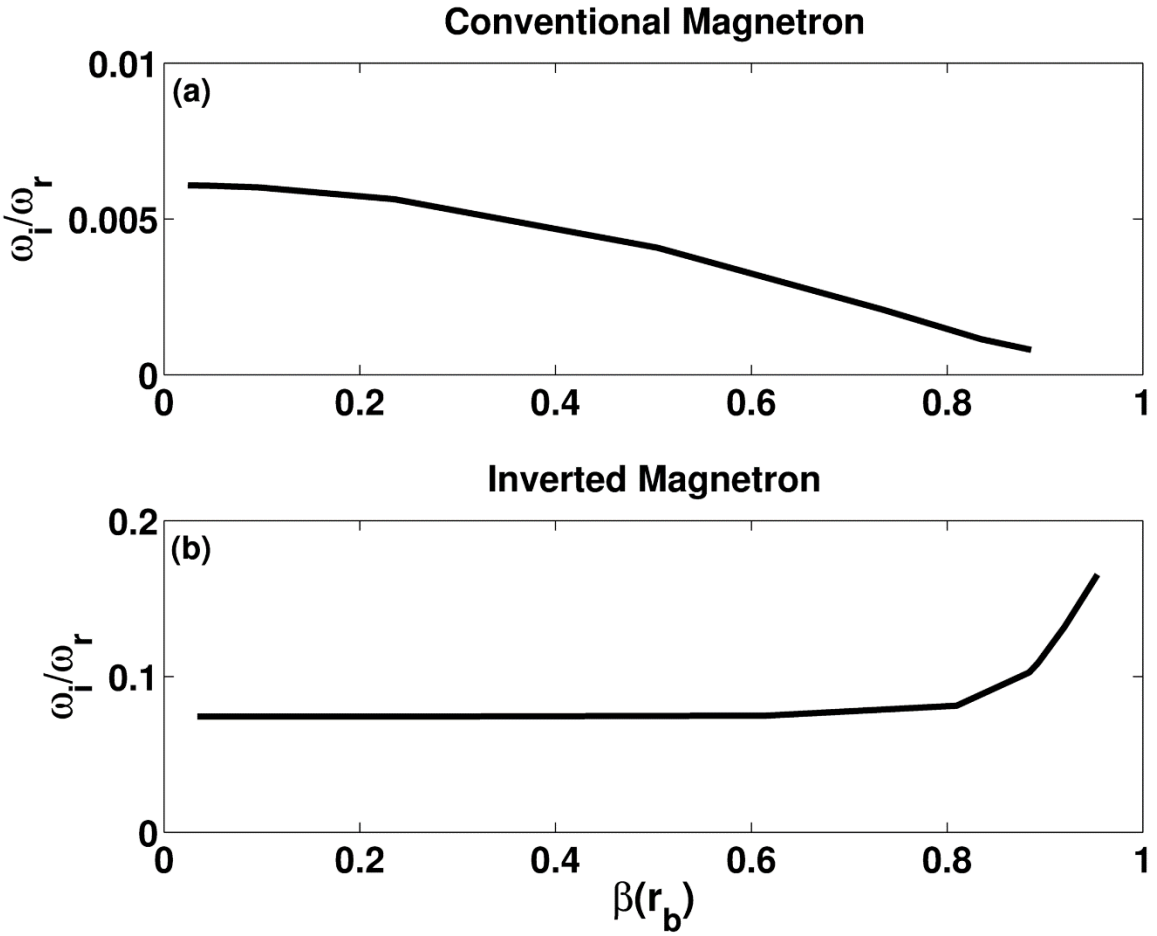

Figure 3.7: Normalized growth rate according to the fully electromagnetic and relativistic formulation as a function of electron velocity (normalized to the speed of light) at the top of the Brillouin hub for (a) conventional and (b) inverted magnetron. The geometry (1m inner radius and 2m outer radius) is held constant, the mode number *l* is set to 8, and the voltage and magnetic field are increased proportionally to achieve a constant hub radius of 1.5m while increasing the electron velocity at the hub [70].

The data presented below will show that the electrostatic results are not quantitatively different from the fully electromagnetic and relativistic treatment. Figure 3.7 shows the normalized growth rate for a cylindrical case as the particle's kinetic energy at the hub increases. The configuration used in both figures is a 1m inner radius, 2m outer radius, 50% Brillouin hub fill of the AK gap, and a mode number l = 8. Typical relativistic magnetron operate between $\beta(r_b)$ of 0.2 and 0.3. These two figures show that conventional magnetrons experience a decrease in growth rate as electrons become more relativistic, while inverted magnetrons have increased growth in the same situation. As with the aspect ratio studies in the previous section, it appears that relativistic effect in the inverted magnetron configuration leads to further destabilization while the conventional magnetron configuration is stabilized.

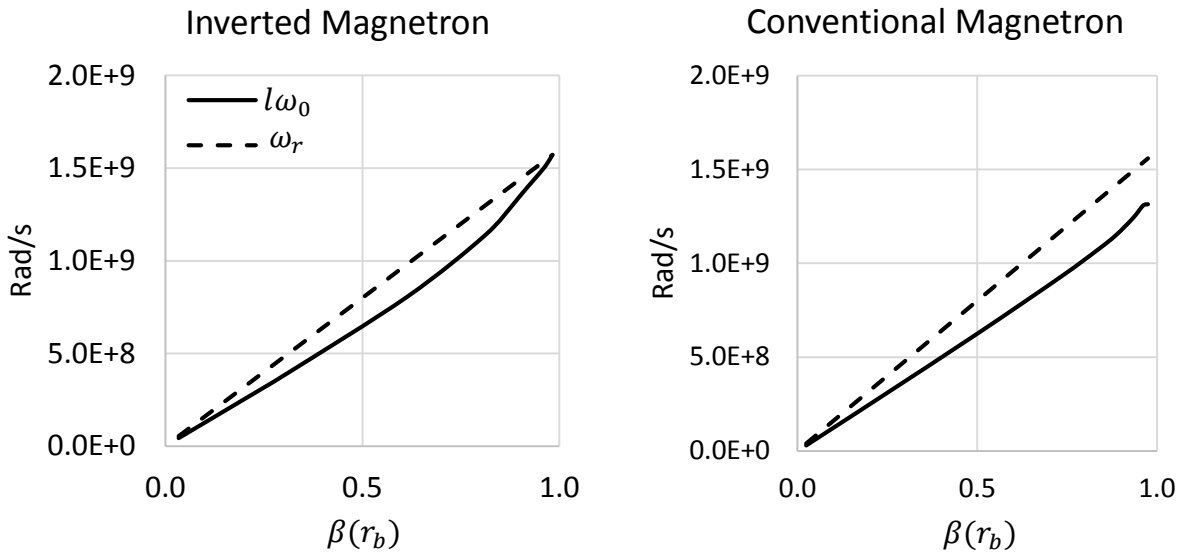

Figure 3.8: A comparison of the eigenvalue frequency (ω_r) to the electron frequency at the top of the Brillouin hub ($l\omega_0$) for inverted and conventional magnetrons. The Brillouin hub height is kept constant, so voltage and magnetic field increases with β.

The inverted configuration in Figure 3.7(b) has a fairly flat normalized growth rate until it experiences a rapid increase at $\beta(r_b)$ greater than about 0.8. This is the region in which the increase in ω_r starts to diminish with the increase in electron energy, and ω_r approaches a limit when the synchronous electrons are reaching the speed of light (since $\omega_r < lv(r_b)/r_b$ for synchronism between the wave and the electrons within the Brillouin hub, and the maximum velocity of $v(r_b)$ is c). The increase in ω_i with electron energy slows down in this region as well, but doesn't approach a limit. The spike in ω_i/ω_r is caused by this behavior, where ω_i increases with increasing electron energy, but ω_r is limited by the electron velocity. This implies that the instability in the

inverted configuration can still exist even as the relativistic mass of the electrons increases greatly. The conventional magnetron's growth rate (Figure 3.7(a)), by contrast, starts to decrease almost immediately with relativistic effects. This difference in behavior is at least partially due to a difference in the behavior of ω_r at highly relativistic values of electron velocity at the top of the Brillouin hub ($\beta(r_b)$), where ω_r approaches $l\omega_0$ for the inverted magnetron, but not for the conventional magnetron as shown in Figure 3.8.

Figure 3.8 is a plot of ω_r and $l\omega_0$ as a function of $\beta(r_b)$ for a constant Brillouin hub height (increasing velocity is due to increasing voltage and magnetic field). In the conventional configuration, the upper limit for electron velocities in the hub is c, however, the synchronous electrons (traveling at $\beta(r) = \omega_r r/c$) have a velocity that is a fraction of c. The synchronous layer is pushed toward the cathode surface as $v(r_b)$ approaches c (In contrast, in the inverted magnetron, the synchronous layer is pushed toward the Brillouin hub radius r_b as $v(r_b)$ approaches c). The proximity of this synchronous layer and the cathode tends to short out the tangential RF electric field at the synchronous layer, thereby reducing the normalized growth rate in the case of conventional magnetron [Figure 3.7a]. For comparison purposes, it has been shown that increasing the particle velocity into the relativistic range slightly reduces the normalized instability growth rate for planar geometries [35], [64].

3.5 Summary

Dimensionless equations are presented for electrostatic Brillouin flow, in both planar and cylindrical magnetrons. The electrostatic eigenvalue solutions for these equations show that the shear flow instability in the planar geometry is reduced in the conventional cylindrical configuration, but enhanced in the inverted configuration. The amount of reduction or enhancement increases as the radii in the system decrease, i.e., as the departure from planar geometry increases. This correlation is consistent with the negative mass instability, which is a cylindrical effect based on the ratio of electric force to centripetal force.

The electrostatic startup condition with constant magnetic field is compared between conventional and inverted smooth-bore magnetrons. Both geometries show that the higher order modes start up first as the voltage is ramped up. In the conventional case the growth rate for any given mode peaks soon after it starts, and then decreases rapidly. On an absolute time scale (normalized to ω_c, Figure 3.6c) the instability strength of each mode is only slightly different than

its nearest neighbors and it decreases as hub height increases. Modes in the inverted case also increase rapidly after starting, but show a very slow decrease in normalized growth rate ω_i/ω_r. This translates into an almost linear increase in ω_i/ω_r with hub height. All modes that enter this regime have roughly equal growth rates (Figure 3.6d), with lower order modes being slightly favored.

The electrostatic results are transitioned smoothly into the electromagnetic regime. The normalized growth rate of the conventional configuration decreases as the electrons at the hub increase in relativistic energy. The normalized growth rate of the inverted magnetron increases as the kinetic energy in the outer hub electrons increases. The planar case shows a decrease in growth rate with an increase in hub electron kinetic energy.

The shear flow instability, or the diocotron-like instability, in a crossed-field geometry has long been conjectured to cause the startup of a magnetron. Here we showed that the Brillouin flow in the inverted magnetron is intrinsically more unstable than the Brillouin flow in the conventional magnetron, consistent with the simulation results of the recirculating planar magnetron that has smooth circular bends.

Finally, for the smooth-bore magnetron, whether it be conventional, planar, or inverted configuration, the azimuthal velocity of the vacuum eigenmode is typically faster than the highest electron flow velocity (because the Brillouin flow constrains zero flow velocity on the cathode), so the vacuum eigenmode cannot be in synchronous interaction with any electron within the Brillouin flow. This is in sharp contrast to the slow-wave structure which is treated in the next chapter, where we show the synchronous interaction with the vacuum eigenmode of the slow-wave structure is critical.

CHAPTER 4

Stability Analysis Including Slow-Wave Structure

4.1 Introduction

The stability of Brillouin flow inside a magnetron with a slow wave structure (SWS) anode has not been studied extensively analytically [71]. This work addresses SWS anodes analytically. First we consider a planar magnetron, we then focus on the π-mode for the inverted and conventional cylindrical magnetron.

Magnetron operation requires synchronicity between the electrons and the RF phase velocity. In practice, this is achieved by reducing the RF phase velocity below the speed of light, which is accomplished by adding a slow wave structure (SWS) to the anode. The SWS creates a path length for the RF that is longer than that of the electrons, effectively slowing down the wave (in the direction of electron motion [72]) so that synchronicity can occur. Figure 4.1 is an example of a planar magnetron with a SWS on the anode. The protrusions on the anode are referred to as vanes. The vane height, h, is the main determinate for the cold tube frequency, defined as the natural mode frequency of the SWS without any electrons. The periodicity, L, restricts the principal wavelength of the electron bunches.

This chapter will include fully relativistic and fully electromagnetic formulation of the eigenvalue solutions and results for both planar and cylindrical magnetrons. The periodic boundary conditions that result from the SWS mean that solutions must now include space harmonics [72]. Additionally, the microwave structure itself has a cold tube dispersion relation which exhibits the resonant cold tube frequencies at a given wavenumber. The addition of a SWS changes the behavior of the Brillouin flow instabilities dramatically. These resonant cold tube modes are absent in the electrostatic treatments of Chapter 3. As we shall see, resonance between the electrons within the Brillouin flow and the SWS is the dominant interaction.

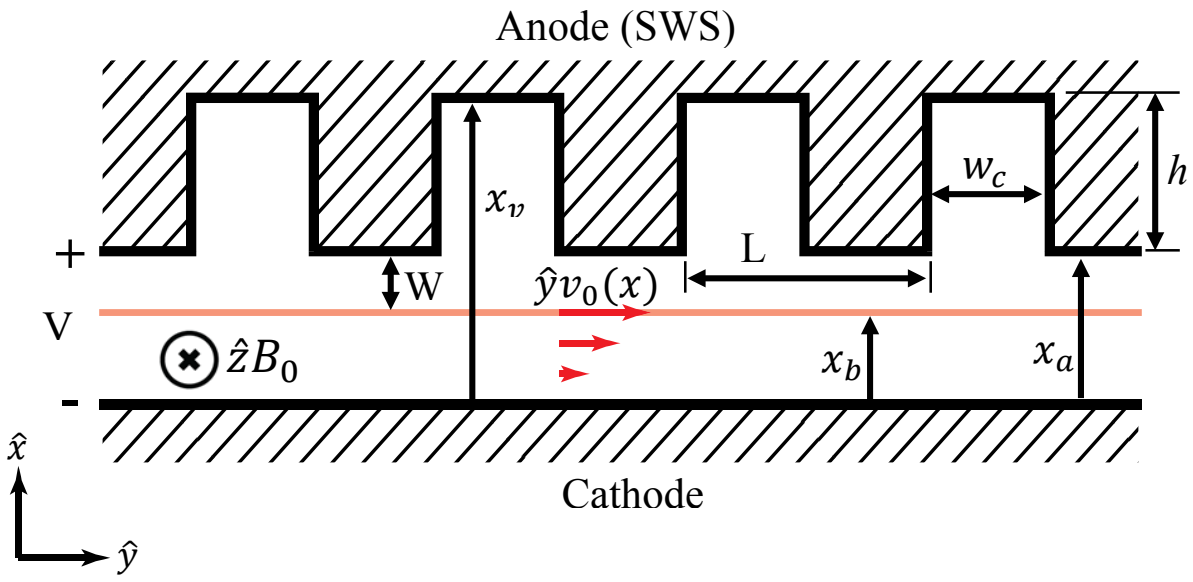

Figure 4.1: Diagram of a planar magnetron with a slow wave structure. The base case parameters for stability analysis are: $x_a = 3.9$cm, $x_b = 1.54$cm, $L = 3.84$cm, $w_c = 1.92$cm, $h = 6.31$cm, $B_0 = 0.0645$T, and $V = 300$kV.

4.2 Planar Brillouin Flow with SWS

The geometry for the system is shown in Figure 4.1. The Brillouin flow equilibrium is assumed to be the same as a smooth-bore anode. This assumption is justified by the boundary condition that requires the field to be normal to the cathode. Figure 4.2 is a contour plot of the strength of the y-component of the DC electric field due to the applied voltage, which demonstrates that the non-uniformity of E_y caused by the periodic SWS is greatly reduced some distance below the anode. We thus assume that the equilibrium Brillouin flow with the SWS is the same as the equilibrium Brillouin flow with a smooth-bore anode at $x = x_a$.

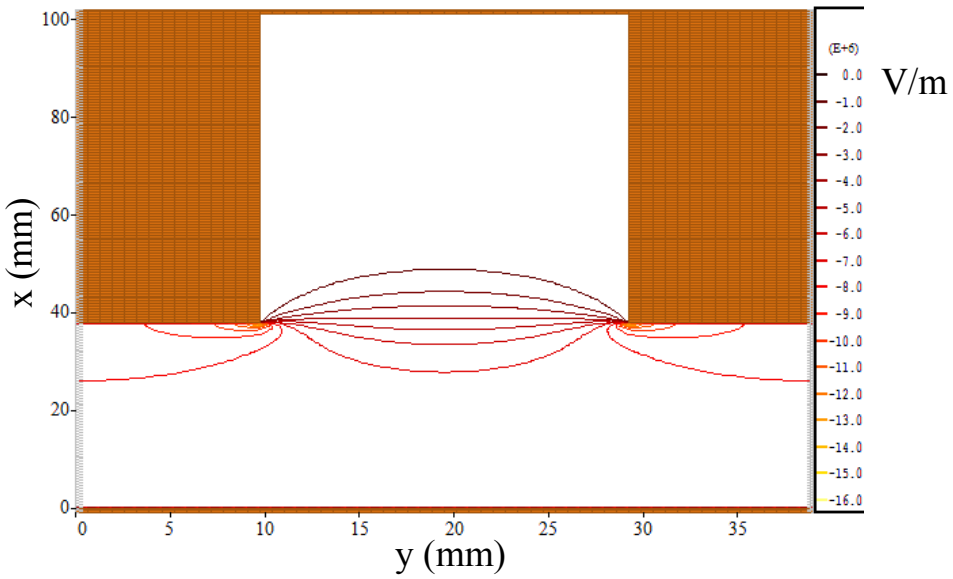

Figure 4.2: Contour of E_y for applied DC bias for one period of a planar magnetron, including the SWS.

The last assumption means that the governing equation for electron motion and the jump condition across the outermost layer of the Brillouin hub are the same as those presented in Chapter 3 for the smooth-bore anode, for each of the space harmonics of the RF field $\vec{E}$, which now contains space harmonics, both within the Brillouin flow and in the vacuum region. These space harmonics must be matched to perturbations within the Brillouin flow. The vacuum fields in these geometries have been derived in the literature [72], [73], so they will be presented with minimal derivation. The periodic vacuum fields have, according to the Floquet theorem [72], the form given below, for $x_b < x < x_a$, (Figure 4.1)

$$\boldsymbol{E} = \sum_{n=-\infty}^{\infty} \left(\hat{x}E_{xn}(x) + \hat{y}E_{yn}(x)\right) e^{j(\omega t - k_n y)}, \tag{4.1}$$

$$\boldsymbol{H} = \sum_{n=-\infty}^{\infty} \hat{z}H_{zn}(x)\, e^{j(\omega t - k_n y)}, \tag{4.2}$$

$$k_n = k_0 + 2\pi n/L, \tag{4.3}$$

where $n = 0, \pm 1, \pm 2, \ldots$. Each value of n corresponds to a space harmonic, and k_0 $(n = 0)$ is referred to as the fundamental wavenumber, or simply the wavenumber. Solving Maxwell's equations within the vacuum region $x_b < x < x_a$ gives the form of each of these fields,

$$H_{zn}(x) = B_n \cosh(\mathrm{s_n}(x - x_a)) + C_n \sinh(s_n(x - x_a)), \tag{4.4}$$

$$E_{xn}(x) = -\frac{k_n}{\omega\epsilon_0}[B_n \cosh(\mathrm{s_n}(x - x_a)) + C_n \sinh(s_n(x - x_a))], \tag{4.5}$$

$$E_{yn}(x) = -\frac{s_n}{j\omega\epsilon_0}\left[B_n \sinh\left(\mathrm{s_n}(x - x_a)\right) + C_n \cosh\left(s_n(x - x_a)\right)\right], \tag{4.6}$$

where $s_n = (k_n^2 - \omega^2/c^2)^{1/2}$ and C_n and B_n are constants.

We assume a TEM mode within the cavities, $x_a < x < x_v$, as was done in [72], [74], [75], so the field over one period (L) is given by

$$E_y(x, y) = \begin{cases} D \sin\left(\frac{\omega}{c}(x - x_v)\right), & -\frac{w_c}{2} < y < \frac{w_c}{2} \\ 0, & otherwise \end{cases} \tag{4.7}$$

$$E_x(x) = 0, \tag{4.8}$$

$$H_z(x) = j\left(\frac{\epsilon_0}{\mu_0}\right)^{1/2} D \cos\left(\frac{\omega}{c}(x - x_v)\right), \tag{4.9}$$

where D is a constant. The boundary condition that E_y be continuous at the cavity mouth ($x = x_a, -L/2 < y < L/2$) is then given by

$$\frac{1}{j\omega\epsilon_0}\sum_{n=-\infty}^{\infty} s_n C_n e^{-jk_n y} = \begin{cases} D \sin\left(\frac{\omega h}{c}\right), & \frac{-w_c}{2} < y < \frac{w_c}{2} \\ 0, & \frac{w_c}{2} < |y| < \frac{L}{2} \end{cases} \tag{4.10}$$

where $h = x_v - x_a$. This equation is a Fourier series, so solving for the coefficients produces

$$C_n = j\omega\epsilon_0 \frac{D}{s_n}\frac{w_C}{L}\sin\left(\frac{\omega h}{c}\right)\frac{\sin(\theta_n)}{\theta_n}, \tag{4.11}$$

where $\theta_n = k_n w_c/2$. The second boundary condition is that the average magnetic field over the cavity mouth is continuous. This boundary condition becomes

$$j\left(\frac{\epsilon_0}{\mu_0}\right)^{1/2} D \cos\left(\frac{\omega h}{c}\right) = \frac{1}{w_c}\int_{-w_c/2}^{w_c/2}\left(\sum_{n=-\infty}^{\infty} B_n e^{-jk_n y}\right) dy. \tag{4.12}$$

After performing the integration and moving the term D into the sum (since it is constant), Eq. (4.12) becomes

$$j\left(\frac{\epsilon_0}{\mu_0}\right)^{1/2} \cos\left(\frac{\omega h}{c}\right) = \sum_{n=-\infty}^{\infty}\frac{B_n}{D}\frac{\sin(\theta_n)}{\theta_n}. \tag{4.13}$$

Equation (4.11) can be solved for D, which is substituted into Eq. (4.13) to get the final vacuum boundary equation,

$$1 - \frac{\omega}{c}\tan\left(\frac{\omega h}{c}\right)\frac{w_c}{L}\sum_{n=-\infty}^{\infty}\frac{1}{s_n}\frac{B_n}{C_n}\left(\frac{\sin\theta_n}{\theta_n}\right)^2 = 0. \tag{4.14}$$

The ratio of B_n/C_n is still needed in order to solve Eq. (4.14). In order to find this value, we must make the assumption that each vacuum space harmonic creates a corresponding mode within the Brillouin hub. For each wavenumber k_n, the value for the ratio of $\phi_n'(x_b)/\phi_n(x_b)$ from the numerical solution (where ϕ_n is a perturbation quantity) within the Brillouin flow (taking into account the jump condition at $x = x_b$) is set equal to the ratio of $\phi_n'(x_b)/\phi_n(x_b)$ of the vacuum field at $x = x_b$. The hub potential, ϕ, is essentially the tangential electric field, E_y. This boundary condition was also used in the derivation of the dispersion relation for thin beams in SWS, in which each space harmonic creates a corresponding density and current perturbation [75], [74].

The hub potential for each space harmonic must be numerically integrated from the governing equation inside the Brillouin hub [50]. Together with the jump condition, the hub potential just outside the Brillouin hub is matched to the vacuum solution (Eq. (4.6)).

$$\frac{\phi_n'(x_b)}{\phi_n(x_b)} = s_n\frac{[B_n\cosh s_nW + C_n\sinh s_nW]}{[B_n\sinh s_nW + C_n\cosh s_nW]}, \tag{4.15}$$

where $W = x_b - x_a$ and the left side of the equation is known from integrating over the Brillouin flow, incorporating the jump condition as explained in the preceding paragraph. Equation (4.15) can be rearranged to find B_n/C_n,

$$\frac{B_n}{C_n} = \frac{\sinh(s_nW) - \frac{\phi_n'(x_b)}{s_n\phi_n(x_b)}\cosh(s_nW)}{\frac{\phi_n'(x_b)}{s_n\phi_n(x_b)}\sinh(s_nW) - \cosh(s_nW)}, \tag{4.16}$$

which can be used to solve Eq. (4.14). Equation (4.14) then becomes the hot tube dispersion relation. It contains an infinite sum, which has been tested empirically for different numbers of terms and shows almost no variation in solutions for $|n| \geq 4$ (9 terms). The results presented in the following sections will use up to $|n| = 5$.

In the limit that the Brillouin hub height approaches the cathode, ϕ_n approaches zero. In this limit B_n/C_n simply becomes $-\coth(s_nx_a)$, and Eq. (4.14) reduces to the cold-tube dispersion relation of the SWS [72].

4.2.1 Planar Base Case and Parameter Sweeps

Solutions to Eq. (4.14) for a range of parameter sweeps will be presented in this section. In addition, it will be argued that the diocotron-like instability found in the planar smooth-bore

magnetrons interacts with the resonant mode created by the SWS circuit, and that this interaction explains the shape of the parameter sweeps. More specifically, it will be shown that the maximum growth occurs when the real part of the frequency of the diocotron-like instability (in the corresponding smooth-bore geometry) and the SWS cold tube frequency are almost equal, and that the system stabilizes as these two frequencies diverge. To this end, the smooth-bore anode solutions to the same geometry (without the cavities) and operating parameters will be presented. The eigenvalue frequency solutions have the general form $\omega = \omega_r - i\omega_i$. The hot tube SWS eigenvalue solutions will be referred to as $\omega_{sws} = \omega_r^{sws} - i\omega_i^{sws}$, the hot tube smooth-bore eigenvalue as $\omega_{sb} = \omega_r^{sb} - i\omega_i^{sb}$, and the cold tube frequency of the SWS will be ω_{ct}. We shall show that instability occurs only when $\omega_r^{sws} \approx \omega_r^{sb} \approx \omega_{ct}$.

The base geometry has the dimensions of the planar section of the RPM 12a [13]: an AK gap width x_a = 3.9cm, a period L = 3.84cm, a vane width $w_c = L/2$, equal to half the period, and a vane height of h = 6.31cm. The operating conditions have been changed from those presented in Chapter 2 so that the eigenvalue solution to the base case has an imaginary component at the fixed π-mode ($k_0 = \pi/L$) which is the usual operating mode in a SWS magnetron, where the RF fields change sign in adjacent cavities. The new operating conditions are 0.0645T and 300keV, which puts the Brillouin hub height at $x_b = 1.54$cm, about half of the AK gap width x_a. The base case is operated in π-mode, which corresponds to $k_0 = 81.8$ rad/m. For this chapter, π-mode will refer to the wavenumber (or azimuthal mode number, for the cylindrical magnetrons) at which there is a π phase shift in the electric field between adjacent cavities, and not the cold tube frequency that corresponds to this shift. At these parameters, $\omega_i^{sws}/\omega_r^{sws}$ is ~3%, which is on the order of the peak value for the instability growth rate for the parameter sweeps that will be presented in this section. The cold tube dispersion relation is shown in black in Figure 4.3, along with the line representing the maximum electron frequency (in red) in the Brillouin hub (defined as $\omega_e(k) \equiv v_0(x_b) * k_0$) and the real part of the eigenvalue solution ($\omega_r^{sws} = 6.51 \times 10^9$ rad/s at the π-mode).

Figure 4.3 shows that at π-mode the cold tube frequency closely matches the eigenvalue solution, but ω_e does not. The Brillouin flow contains a continuum of electron velocities $v_0(x)$, so that the various "beam lines" $\omega_r = k_0 v_0(x)$ occupy all the space below the plotted beam line (ω_e) which corresponds to the maximum flow velocity. An electron traveling at ~60% of the

velocity of the electrons at the edge of the Brillouin hub would intersect the eigenvalue frequency at π-mode.

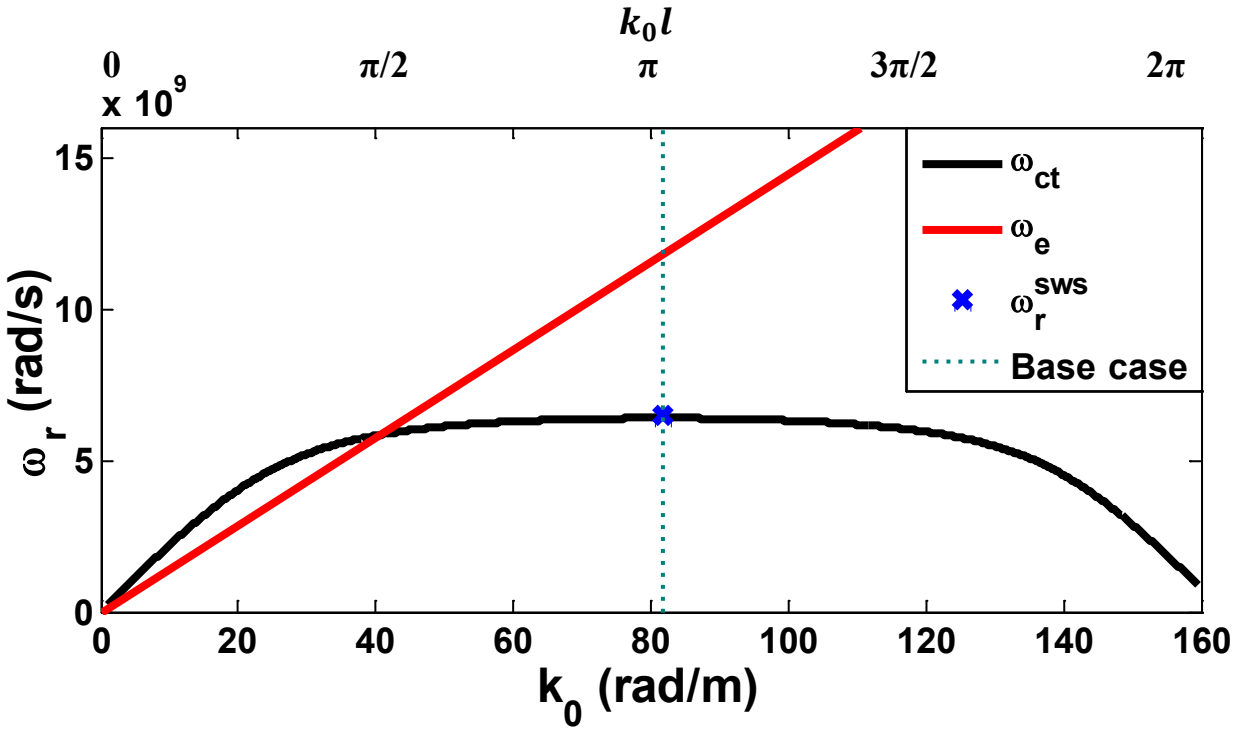

Figure 4.3: Base case ($k_0 = 81.8$ rad/m corresponding to π-mode) plot of cold tube dispersion relation (ω_{ct}), maximum velocity of the beam line (ω_e), and value for the real part of ω from the eigenvalue solution(ω_r^{sws}).

The first parameter to be varied is wavenumber. The base case has π-mode operation ($k_0 = 81.8\, rad/m$). The real part of the hot tube frequency is found to be linear with wavenumber, as shown in the solid blue line in Figure 4.4. The imaginary part (i.e., the growth rate) shows a symmetric profile around a central peak of 80 rad/s as shown in the solid green curve in Figure 4.4. It extends for 4% of the wavenumber at peak growth in either direction before stabilizing. Wavenumbers from 30 to 90 rad/m were tested; only those plotted in Figure 4.4 showed growth with the SWS anode. This includes the intersection of ω_e and ω_{ct} at $k = 38$ rad/m shown in Figure 4.3. The smooth-bore anode shows no growth in this region.

Figure 4.3 shows that there is always an electron layer within the Brillouin hub that is synchronous with the RF in the cold tube for all wavenumbers larger than the intersection point at 38 rad/m (Figure 4.3), and yet Figure 4.4 shows that synchronism only produces growth for the range of wavenumbers between 77 and 83 rad/m. A comparison of ω_r for the smooth-bore and ω_{ct} shows that very near the point at which they intersect each other ω_i for the SWS is at a

maximum. The true maximum peak for ω_i for the SWS occurs at 80 rad/m, while the intersection of ω_r for the smooth-bore and cold tube occurs at 80.2 rad/m. For the SWS ω_r^{sws} lies between the smooth-bore (ω_r^{sb}) and cold tube (ω_{ct}) values, and is very nearly the average value of two ($\omega_r(average) = \omega_{ct}/2 + \omega_r^{sb}/2$) as shown in Figure 4.4, and in greater detail in Figure 4.5. This relation, that ω_r^{sws} is the average of ω_{ct} and ω_r^{sb}, will hold true for π-mode results, but not for results at other modes, as will be shown in Figure 4.10 below. As ω_{ct} and ω_r^{sb} diverge, the hot tube growth rate in the SWS, ω_i^{sws}, decreases. When the difference between ω_{ct} and ω_r^{sb} exceeds about 8%, $\omega_i^{sws} \to 0$, and the system becomes stable. This strongly suggests that the SWS resonantly excites the diocotron instability in the Brillouin flow. This synchronous instability is absent in the corresponding smooth-bore magnetron under the electrostatic approximation. For the smooth-bore magnetron, there is no synchronous instability in a fully electromagnetic treatment either, because the phase velocity in the $\hat{y}$ direction, ω_{ct}/k_y, is always larger than c, whereas the electron speed is always less than c (c = light speed).

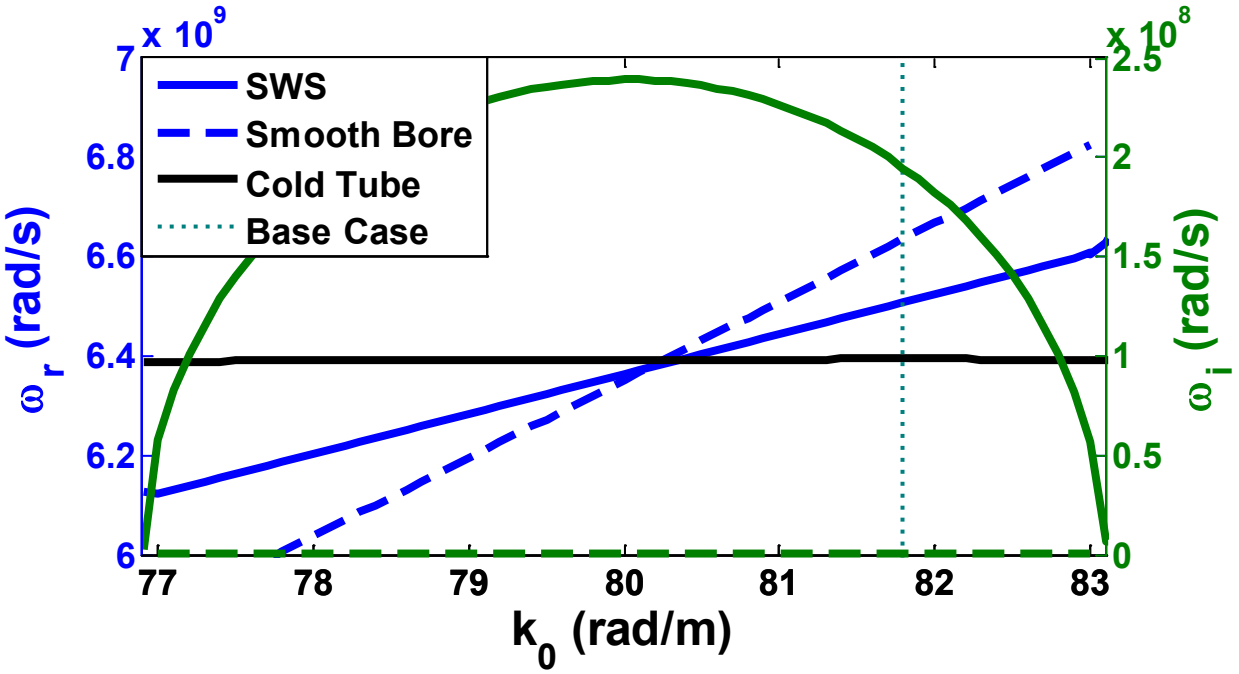

Figure 4.4: Eigenvalue solutions for ω_r and ω_i as a function of k_0, with all other parameters equal to the base case (shown as the vertical dotted line). Solid lines correspond to SWS, dashed lines to smooth-bore.

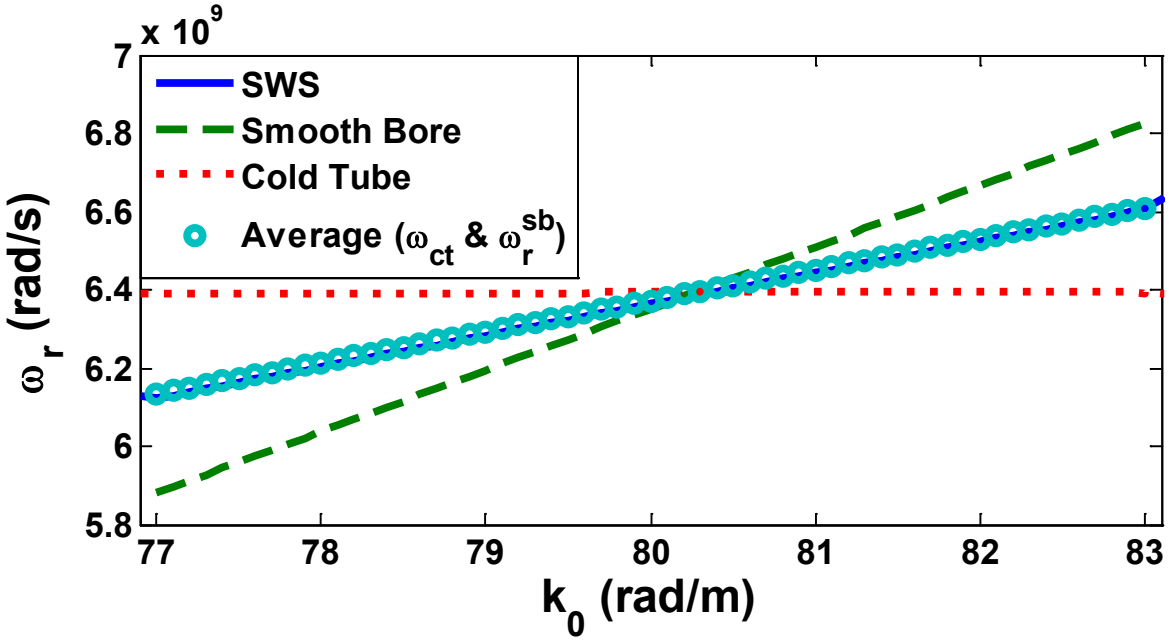

Figure 4.5: ω_r for the smooth-bore magnetron, cold tube dispersion, and SWS magnetron, plotted alongside the average of ω_r from the smooth-bore and cold tube.

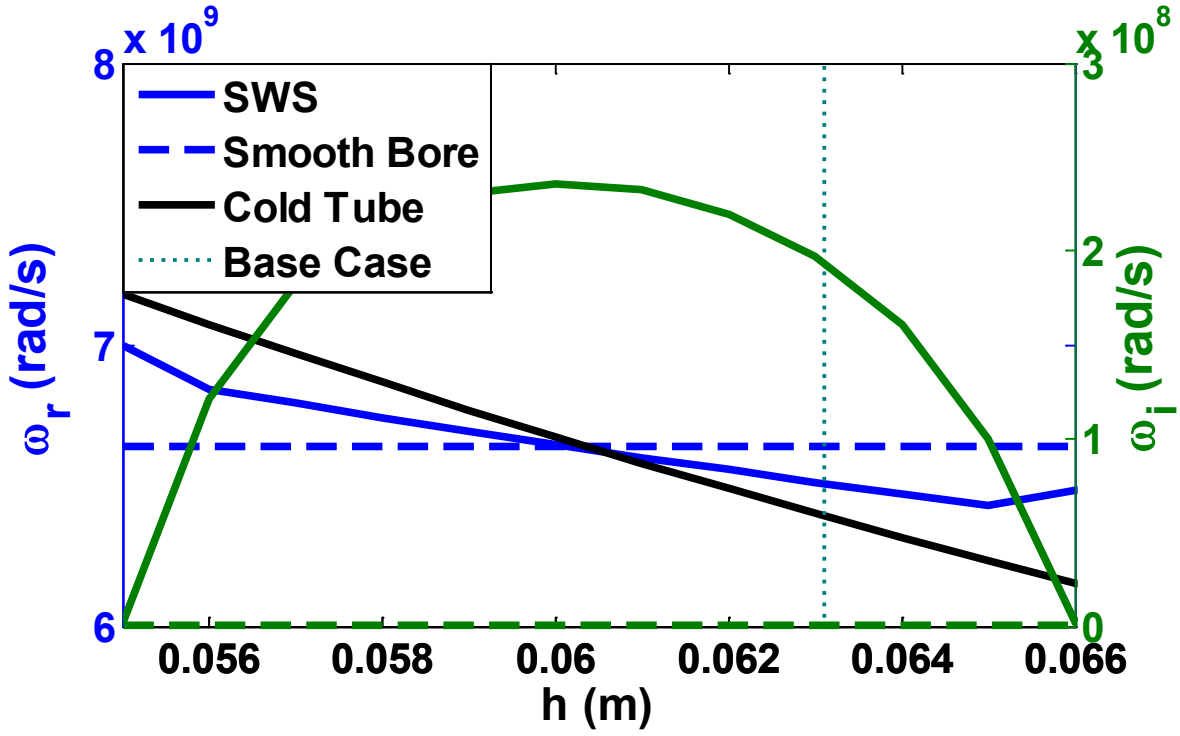

Figure 4.6: Eigenvalue solutions for ω_r and ω_i at π-mode (k_0 = 81.8rad/m) as a function of h, with all other parameters equal to the base case. Solid lines correspond to SWS, dashed lines to smooth-bore.

Figure 4.6 is a plot of the effect of varying vane height (h) at π-mode while keeping everything else constant at the base case values. The range of tested values for h is 3 to 10 cm, but only the region with instability growth is plotted in the Figure 4.6. As with the wavenumber, there is a narrow region of vane heights that allow for instability growth despite the presence of synchronous electron layers within the Brillouin hub over the entire tested range. The other trends identified in Figure 4.4 hold true here as well. The peak in ω_i^{sws} occurs close to, but not exactly at, the intersection of ω_r^{sb} and ω_{ct}, and the value for ω_r^{sws} is very nearly the average of ω_r^{sb} and ω_{ct}. The system also stabilizes when the difference between the cold tube and smooth-bore frequencies exceeds 8%, the same as the sweep over wavenumber.

Figure 4.7 is a sweep over the magnetic field (B), keeping the Brillouin hub height and the remainder of the base case parameters the same, except for the applied AK gap voltage (V). In order to keep the Brillouin hub height constant, the voltage V must roughly change with the square of the magnetic field B. (The reason is that the Poisson equation implies a scaling of $V \propto \omega_p^2$ whereas $\omega_p^2 \propto \omega_c^2$ for Brillouin flow, leading to $V \sim B^2$ roughly). The range of magnetic fields tested is from 0.01 – 0.1 T. The result is a change in the velocity profile of the Brillouin hub. Larger voltages and the associated higher magnetic fields lead to higher electron velocity at the edge of the hub and a larger velocity gradient within the hub. This sweep over the magnetic field, unlike the previous sweeps over wavenumber and cavity height (Figure 4.4 and Figure 4.6), changes the equilibrium Brillouin flow. Despite this change, we see the same trends identified in those plots. Specifically, the three main trends that are common to all three sweeps are (a) that the maximum growth rate occurs very close to (although not exactly at) the point at which ω_{ct} and ω_r^{sb} intersect, (b) that ω_r^{sws} is nearly the average of ω_{ct} and ω_r^{sb}, and (c) that a small difference (~8%) in ω_{ct} and ω_r^{sb} leads to stabilization of the system.

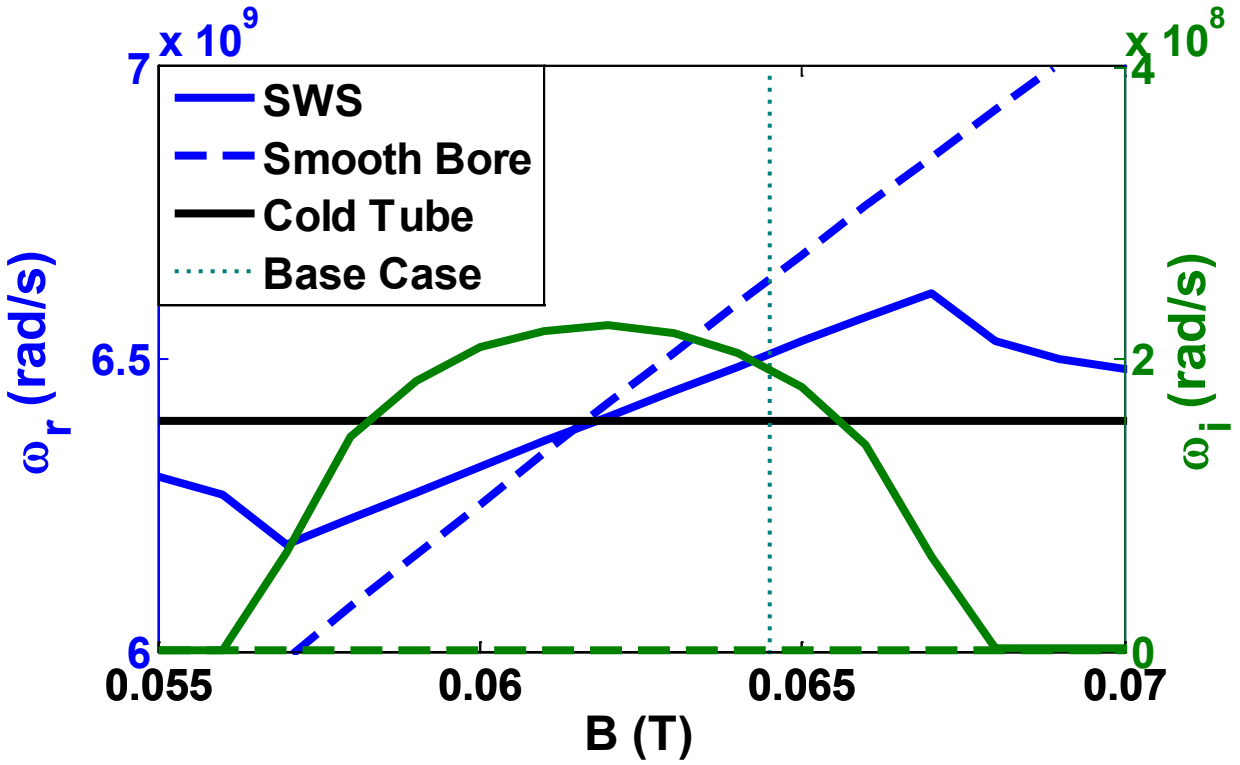

Figure 4.7: Eigenvalue solutions for ω_r and ω_i at π-mode (k_0 = 81.8 rad/m) as a function of magnetic field (B), with all other parameters equal to the base case. Solid lines correspond to SWS, dashed lines to smooth-bore.

Figure 4.4, Figure 4.6, and Figure 4.7 establish that instability occurs when ω_{ct} and ω_r^{sb} are close in value. The smooth-bore frequency varies with wavenumber k_0 and magnetic field, so multiple combinations of the two can result in a value of ω_r^{sb} that matches ω_{ct}, as shown in Figure 4.8. The larger magnetic field cases peak at smaller wavenumbers and have higher peak instability growth rates and a larger range of unstable wavenumbers than the smaller magnetic field cases.

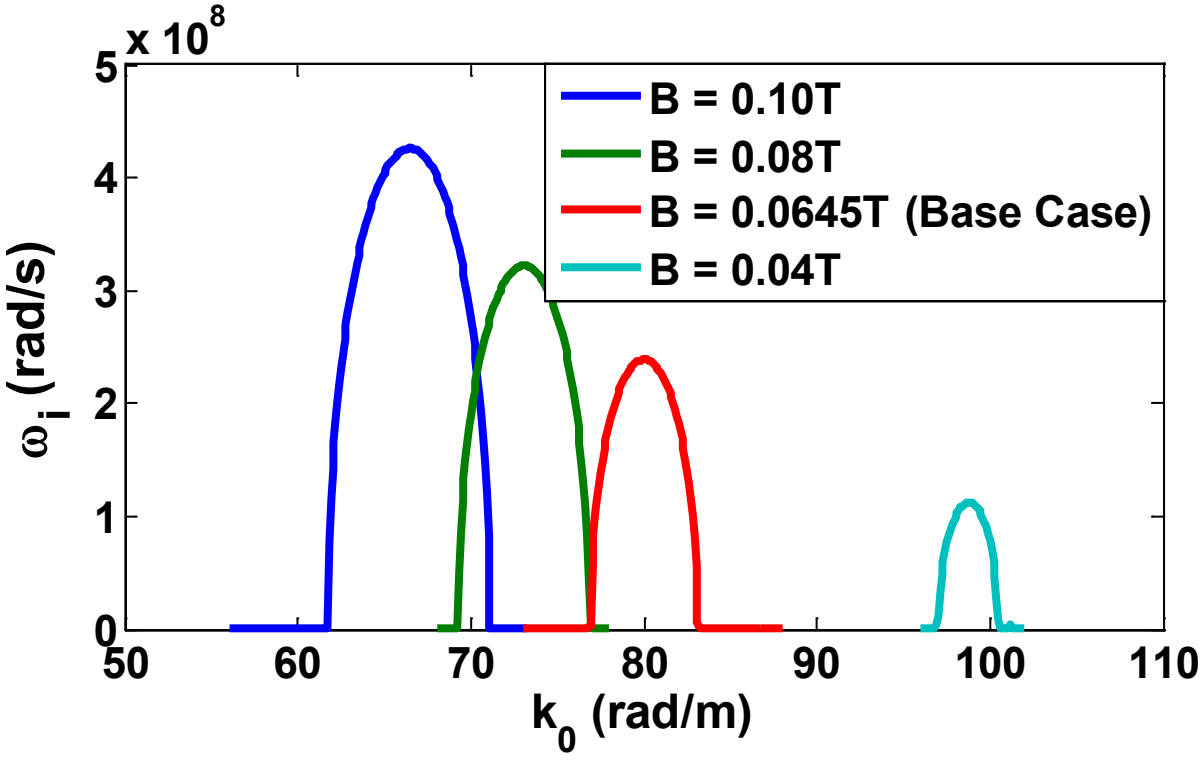

Figure 4.8: Eigenvalue solutions for ω_r and ω_i as a function of k_0 for different values of the magnetic field, with all other parameters equal to the base case.

Figure 4.9 is a sweep of the Brillouin hub height x_b, varying the voltage and keeping the magnetic field and all other parameters constant. In non-relativistic operation, this would be equivalent to changing the velocity ($v_0(x) = \omega_c x$) of the electrons at the top of the hub (which is expanding as voltage increases, see Eq. (1.8c)) without altering the velocity gradient of electrons within the hub. In the relativistic region that this test magnetron is operating in, the velocity gradient changes slightly with hub height, but is still fairly constant. Figure 4.9 is the equivalent of the startup plots from the previous chapter (cf. Figure 3.6a,c), focused only on π-mode operation. The smaller hub heights correspond to smaller voltages, so moving from left to right increases the voltage of a magnetron while keeping the magnetic field constant. Instability occurs when the hub height increases to 0.015m.

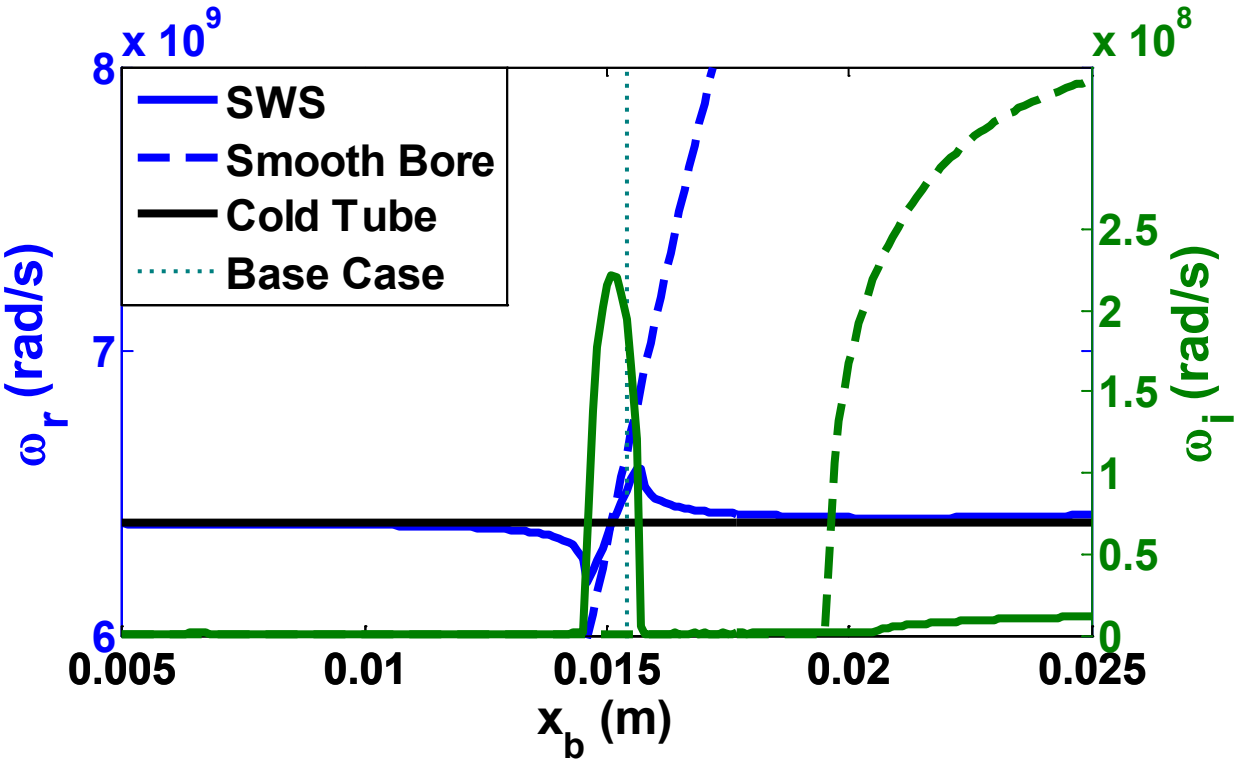

Figure 4.9: Eigenvalue solutions for ω_r and ω_i at π-mode (k_0 = 81.8rad/m) as a function of hub height (x_b) by changing the gap voltage, with all other parameters equal to the base case. Solid lines correspond to SWS, dashed lines to smooth-bore.

In Figure 4.9, the values for ω_r^{sb} (dashed blue line) are off the axis for the SWS trends to be clearly seen. The real part of the smooth-bore frequency (ω_r^{sb}) increases linearly to a maximum of 12.75e9 rad/s at x_b = 0.025m. The maximum normalized growth rate for the smooth-bore magnetron,$\omega_i^{sb}/\omega_r^{sb}$, occurs at x_b = 2.37cm and is 2.7%, which is comparable to the maximum normalized growth of the SWS magnetron: 3.45% at x_b = 1.51 cm.

Figure 4.9 shows two regions of instability. The first one, for $x_b < 2$cm, follows the same three trends as the sweeps of wavenumber, cavity height, and magnetic field. The second region of instability occurs when the Brillouin hub height exceeds 2.1cm. The start of this instability roughly coincides with the start of instability growth in the smooth-bore magnetron. The instability is an order of magnitude lower than the peak instability growth rate at x_b = 1.54cm and continues to the edge of the tested values, x_b = 2.5cm. The second instability differs from the first in a number of ways. The growth for the second instability occurs in a region in which ω_{ct} (black curve) and ω_r^{sb} (dashed blue curve) differ by a factor of ~2, whereas these frequencies are roughly equal for the first instability. In the first instability, ω_r^{sws} (solid blue curve) is nearly the average of ω_{ct}

(black curve) and ω_r^{sb} (dashed blue curve), while in the second instability ω_r^{sws} is just slightly higher than ω_{ct} and doesn't appear to be influenced by ω_r^{sb}. This suggests that the second instability represents a mild destabilization of the cold tube mode by the diocotron effect.

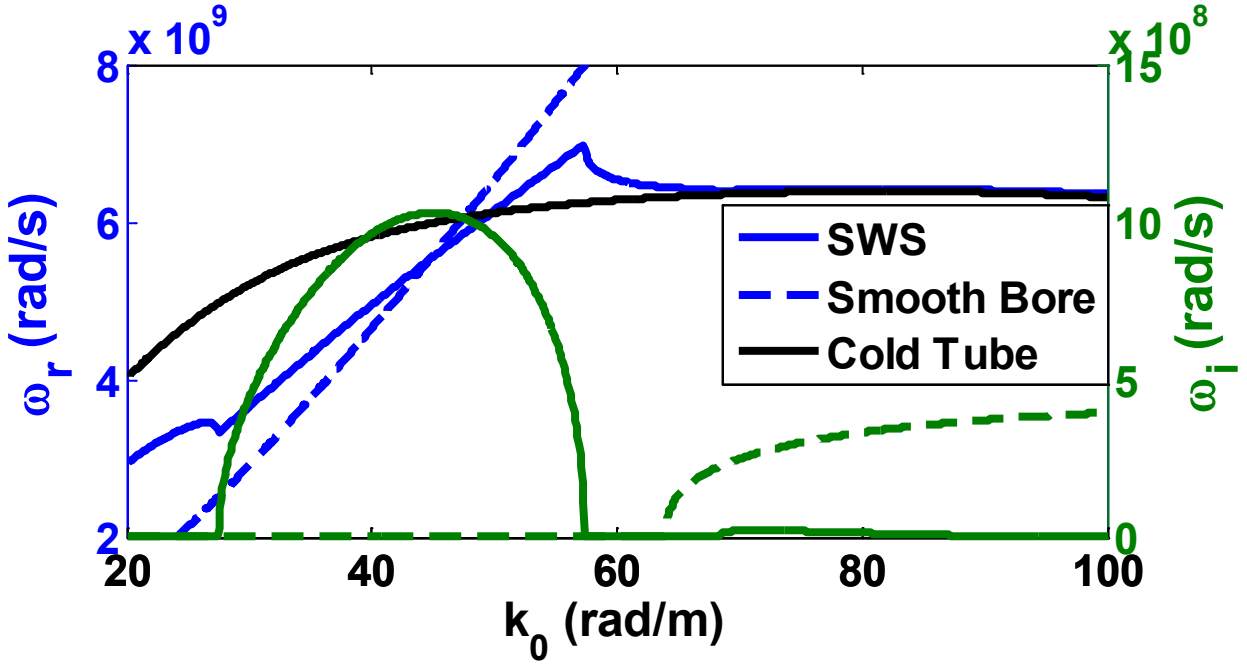

Figure 4.10: Eigenvalue solutions for ω_r and ω_i as a function of k_0 for x_b=0.025m, by raising the gap voltage, with all other parameters equal to the base case.

Figure 4.10 shows a sweep of wavenumber for x_b = 2.5cm, this hub height is obtained by raising the gap voltage, but fixing the magnetic field and all other parameters equal to the base case, as in Figure 4.9. The solid green line in Figure 4.10 again shows two regions of instability, a strong instability at lower wavenumbers, and a weak instability at high wavenumbers, just like the solid green line in Figure 4.9. Also in common with Figure 4.9 is that the very weak instability starts as the instability in the smooth-bore magnetron is starting, and that the real part of the frequency is very close to the cold tube frequency. Additionally, Figure 4.10 demonstrates that ω_r^{sws} is not always the average between ω_{ct} and ω_r^{sb} for modes other than π-mode, although it lies between them for the majority of the strongly unstable region. Note that at $k_0 \approx 45$ rad/m, $\omega_i^{sws}/\omega_r^{sws} \approx 11\%$, implying a very high growth rate. This high growth rate is probably due to much larger hub height x_b, making the fringing field at the vane more appreciable at the synchronous electron layer.

The previous figures have all had a separation of the strong instability in the SWS and the onset of instability in the smooth-bore magnetron. This separation is a result of the geometry

chosen, and it is instructive to change the geometry to such an extent that both the SWS and smooth-bore magnetrons are unstable at the same operating parameters and wavenumbers. Figure 4.11 shows a sweep of h at x_b = 0.025m and π-mode. The smooth-bore magnetron is unstable in this figure as shown by the dashed green line. The cold tube frequency of the SWS magnetron (black line) is changed as h is changed, leading to a region where the SWS magnetron experiences the strong instability ($h < 0.032$m). The weaker instability region (0.04m< h <0.08m) is also present here. There is no smooth transition of the weak instability region to the strong instability region, as shown in Figure 4.11. When ω_{ct} approaches ω_r^{sb}, the synchronous instability starts, and its growth rate is ~3 times larger than the diocotron-like only instability present in the smooth-bore magnetron.

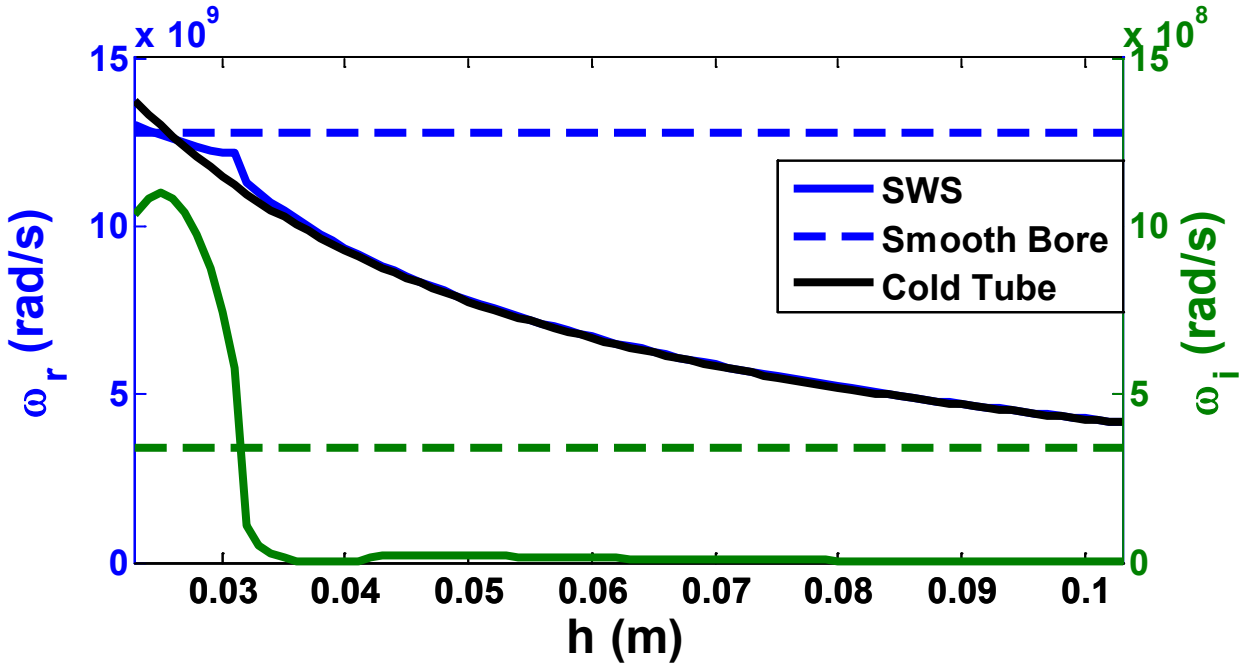

Figure 4.11: Eigenvalue solutions for ω_r and ω_i at π-mode as a function of h at x_b= 2.5cm, by raising the gap voltage, but fixing the magnetic field and all other parameters equal to the base case. Solid lines correspond to SWS, dashed lines to smooth-bore.

The results presented in this section support the argument made at the beginning, that the strong instability is a result of an interaction between the layer of electrons subject to the diocotron-like instability and the resonance caused by the SWS. The figures show close agreement between the cold tube and smooth-bore frequencies in the regions in which the SWS magnetron is unstable.

In general (although there is a small exception in Figure 4.10), the SWS unstable mode's frequency lies between the cold tube and smooth-bore frequencies.

The weak instability behaves differently. It appears to coincide with the start of the diocotron-like instability in the smooth-bore magnetron; however, it occurs very near the cold tube frequency, and quite far from the smooth-bore diocotron frequency. Also of interest is there is no smooth transition between this weak instability and the strong synchronous instability.

4.3 Cylindrical Brillouin Flow with SWS

The basic geometry of the cylindrical magnetron with SWS is shown in Figure 4.12 for the conventional (left) and inverted magnetron (right). The Brillouin flow region is marked in red. In the conventional (inverted) magnetron, the cathode is on the inside (outside) and the anode is on the outside (inside). The base geometry of the cylindrical magnetron is similar to the planar section of the RPM 12a that was presented in Section 4.2.1 and Figure 4.1. This design was chosen instead of the devices from Chapter 2 so that a comparison could be made between the planar, conventional, and inverted magnetrons. The parameters of the base geometry are listed in Table 4.1. The parameters that are common to the base case of all three geometries (planar, conventional, and inverted) are given in bold in Table 4.1.

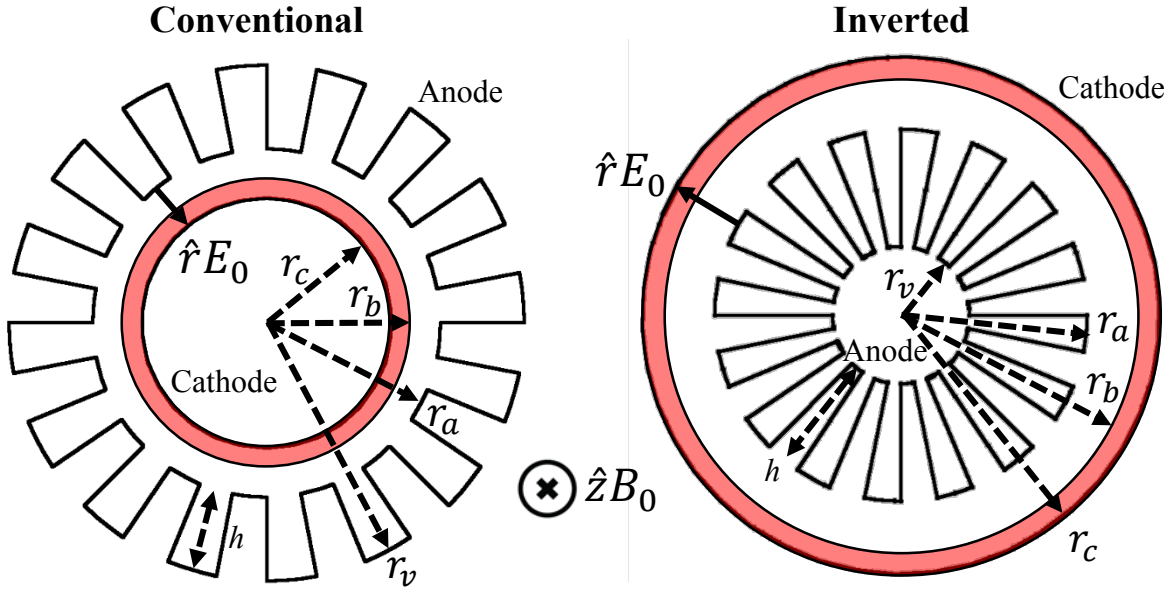

Figure 4.12: Geometry of conventional (left) and inverted (right) cylindrical magnetrons. Graphs are not drawn to scale, but are proportionally correct for the base case.

For the base case of the cylindrical magnetron, the inner radius (r_c for the conventional, r_a for the inverted) is 10cm and the outer radius is 13.9cm, resulting in an AK gap of 3.9cm which is the same as the planar geometry. The cavity height h is 6.31cm, so r_v is 20.21cm for the conventional magnetron and 3.69cm for the inverted. We assume that there are N = 16 cavities in both designs, and π-mode has an azimuthal mode number l = 8. The number of cavities is chosen to keep the distance traveled by an electron over one period roughly equal to the planar period of L = 3.84cm. The magnetic field is held constant at 0.0645T, which results in a voltage of 238kV for the conventional magnetron and 378kV for the inverted magnetron (Table 4.1).

Table 4.1: Operational parameters and geometry for the base case conventional and inverted magnetrons. Quantities that are the same between the two types and the planar magnetron are highlighted in **bold**.

Parameter	*Conventional*	*Inverted*
Cathode Radius: r_c	10cm	13.9cm
Anode Radius: r_a	13.9cm	10cm
AK Gap: $\lvert r_c - r_a \rvert$	**3.9cm**	**3.9cm**
Brillouin Hub: $\lvert r_b - r_c \rvert$	**1.54cm**	**1.54cm**
h: $\lvert r_v - r_a \rvert$	**6.31cm**	**6.31cm**
Magnetic Field: B_0	**0.0645T**	**0.0645T**
Applied Voltage: V	238kV	378kV
Number of Cavities: N	16	16

As in Section 4.2, the procedure for deriving the hot tube dispersion relation for the cylindrical magnetrons is the same as the planar geometry. For the cylindrical geometry (Figure 4.12). The small signal RF fields in between r_b and r_a are given by, assuming $e^{j\omega t - jn\theta}$ dependence,

$$H_{zn}(r,\theta) = B_n J_n(pr) + C_n Y_n(pr), \tag{4.17}$$

$$E_{rn}(r,\theta) = \left(-\frac{\omega\mu_0}{p^2}\frac{\mathrm{n}}{r}\right)[B_n J_n(pr) + C_n Y_n(pr)], \tag{4.18}$$

$$E_{\theta n}(r,\theta) = \left(\frac{j\omega\mu_0}{p}\right)[B_n J_n'(pr) + C_n Y_n'(pr)], \tag{4.19}$$

where $p = \omega/c$. The azimuthal electric field in each vane entrance ($r = r_a$) is assumed to be constant, D, so that the RF fields within the vane (r between r_a and r_v) are given by,

$$E_\theta(r,\theta) \tag{4.20}$$
$$= \begin{cases} D\left[\dfrac{J_0'(pr)Y_0'(pr_v) - J_0'(pr_v)Y_0'(pr)}{J_0'(pr_a)Y_0'(pr_v) - J_0'(pr_v)Y_0'(pr_a)}\right] e^{-j2ql\pi/N}, & \dfrac{2q\pi}{N} - \theta_0 < \theta < \dfrac{2q\pi}{N} + \theta_0 \\ 0, \quad otherwise \end{cases}$$

$$E_r(r,\theta) = 0, \tag{4.21}$$

$$H_z(r,\theta) = \frac{pD}{j\omega\mu_0}\left[\frac{J_0(pr)Y_0'(pr_v) - J_0'(pr_v)Y_0(pr)}{J_0'(pr_a)Y_0'(pr_v) - J_0'(pr_v)Y_0'(pr_a)}\right] e^{-j2ql\pi/N}, \tag{4.22}$$

where Eq. (4.20) applies to the q[th] cavity entrance which subtended an azimuthal angle θ_0 [75], $q = 1,2,\ldots N$, and N is the number of cavities. The boundary conditions at the vane entrance are that the azimuthal electric field is matched exactly, and that only the average magnetic field is matched. As with the planar case, the first boundary condition leads to a set of Fourier coefficients,

$$D\left(\frac{N\theta_0}{\pi}\right)\left(\frac{\sin(n\theta_0)}{n\theta_0}\right) = \left(\frac{j\omega\mu_0}{p}\right)[B_nJ_n'(pr_a) + C_nY_n'(pr_a)], \tag{4.23}$$

where the periodicity of the electric field in the vanes means that the values of n can be restricted to $n = l + mN$, where $l = 0, 1, 2, \ldots, N-1$, and m can be any integer including zero. The $l = 0$ mode is called the zero-mode (or 2π-mode), meaning that there is no (or 2π) phase shift between neighboring cavities in the RF fields. The $l = N/2$ mode is called the π-mode. For each l, the $m = 0$ mode is called the fundamental mode, and other values of m are known as the m^{th} space harmonic. The average magnetic field boundary condition leads to [75]

$$\frac{pDe^{-\frac{jq2l\pi}{N}}}{j\omega\mu_0}F = \frac{1}{2\theta_0}\sum_{\mathrm{m}=-\infty}^{\infty}[B_nJ_n(pr_a) + C_nY_n(pr_a)]\frac{2\sin(n\theta_0)}{n}e^{-\frac{j2q\pi n}{\mathrm{N}}}, \tag{4.24}$$

where

$$F = \frac{J_0(pr_a)Y_0'(pr_v) - J_0'(pr_v)Y_0(pr_a)}{J_0'(pr_a)Y_0'(pr_v) - J_0'(pr_v)Y_0'(pr_a)}. \tag{4.25}$$

The exponents on both sides of Eq. (4.24) cancel exactly because they differ by $e^{-j2qm\pi}$, which is unity, as q and m are integers. Dividing Eq. (4.24) by D, and using Eq. (4.23) for D, results in a final equation,

$$F - \frac{N\theta_0}{\pi}\sum_{\mathrm{m}=-\infty}^{\infty}\frac{\left[J_n(pr_a) + \frac{C_n}{B_n}Y_n(pr_a)\right]}{\left[J_n'(pr_a) + \frac{C_n}{B_n}Y_n'(pr_a)\right]}\left(\frac{\sin(n\theta_0)}{n\theta_0}\right)^2 = 0. \tag{4.26}$$

We use Eq. (3.15) to numerically integrate the solution $\phi'_{n1}(r_b)/\phi_{n1}(r_b)$ within the Brillouin flow for each space harmonic. We apply the jump condition across the top of the Brillouin hub, $r = r_b$, (Figure 4.12, see also Eq. (3.21)). We may define a normalized impedance, b_n, in terms of this numerically integrated value of $\phi'_{n1}(r_b)/\phi_{n1}(r_b)$ (plus the jump condition (3.21)) as

$$b_n = \frac{iE_{rn}}{E_{\theta r}}\bigg|_{r_{vac}} = -\frac{nr_b}{p^2 r_b^2 - n^2}\frac{\phi'_{n1}(r_b)}{\phi_{n1}(r_b)}\bigg|_{r_{vac}}, \tag{4.27}$$

which must be equated to the normalized impedance obtained from the vacuum field solution at $r = r_b$, for each space harmonic,

$$b_n = -\frac{n}{pr_b}\left(\frac{B_n J_n(pr_b) + C_n Y_n(pr_b)}{B_n J'_n(pr_b) + C_n Y'_n(pr_b)}\right), \tag{4.28}$$

From Eq. (4.28), the ratio C_n/B_n is given by

$$\frac{C_n}{B_n} = -\frac{\frac{b_n r_b p}{n} J'_n(pr_b) + J_n(pr_b)}{\frac{b_n r_b p}{n} Y'_n(pr_b) + Y_n(pr_b)}. \tag{4.29}$$

Upon substituting Eq. (4.29) into (4.26), with the understanding that b_n in Eq. (4.29) is now given in term of the numerically integrated value of $\phi'_{n1}(r_b)/\phi_{n1}(r_b)$ (plus the jump condition) defined in (4.27), Eq. (4.26) is the hot tube dispersion relation. As with the planar case, in the limit that the Brillouin hub approaches the cathode, $r_b \to r_c$, $E_\theta \to 0$, and $b_n \to \infty$ by Eq. (4.27). Thus, $C_n/B_n \to -J'_n(pr_b)/Y'_n(pr_b) \cong -J'_n(pr_c)/Y'_n(pr_c)$ by Eq. (4.29), and the hot tube dispersion relation Eq. (4.26) then reduces to the traditional cold tube dispersion relation for the cylindrical magnetron [73], [75].

4.3.1 Parameter Sweeps

This section will cover the solutions to Eq. (4.26) for both the conventional and inverted magnetrons. The parameter sweeps will include the azimuthal mode number l, magnetic field B, Brillouin hub height $|r_b - r_c|$, and vane height $h = |r_v - r_a|$, analogous to parameters covered for the planar magnetron in Section 4.2.1 (i.e. k_0, B, x_b, h). In addition, the effect of curvature on the magnetic field sweep will be explored by changing the inner and outer radii and cavity number while keeping the AK gap and the distance traveled by an electron over one period (L = 3.84cm) approximately constant.

In this section, it will be argued that the cylindrical Brillouin flow in a magnetron with a SWS is unstable when $\omega_r^{sws} \approx \omega_r^{sb} \approx \omega_{ct}$. This is the same instability condition as the Brillouin flow in a planar SWS magnetron. Furthermore, the peak normalized growth rate (ω_i/ω_r) does not appear to be influenced by the negative mass effect, as it is similar for both the conventional and inverted magnetrons (with the conventional magnetron showing slightly larger growth). The synchronous instability appears to be the dominant cause of instability growth, although curvature does have an effect on the range of unstable parameters and the overall magnitude of their instability.

Figure 4.13 shows the dispersion relation for the conventional (a) and inverted (b) magnetrons along with the base case beam lines and the eigenvalue solutions for each mode at the base case parameters (Table 4.1). The maximum electron frequency within the Brillouin hub is now defined as $\omega_e(l) \equiv v_0(r_b) * l/r_b$. The inverted magnetron operates at a higher frequency for a given mode number. The cavities conform to the cylindrical coordinate system, as shown in Figure 4.12, so the conventional magnetron has a greater RF path length for the same *h* value than the inverted magnetron.

The eigenvalue solutions in Figure 4.13 are at discrete points, since the azimuthal mode number, l, must be an integer. The hollow circular points represent the hot tube SWS solutions, while the plus signs represent the hot tube smooth-bore solutions. The solid circles are the result of the solutions overlapping. Both the conventional and inverted magnetrons show instability at the mode number where ω_r^{sb} is closest to ω_{ct}. This instability has a normalized growth rate (ω_i/ω_r) of 3.6% for the conventional magnetron and 2.2% for the inverted magnetron. In contrast, the peak ω_i/ω_r values for the smooth-bore magnetrons are 2.1% and 7.7% respectively. Also of note, ω_r^{sb} is approximately 5×10^9 rad/s below ω_e, which is quite similar to the non-relativistic planar asymptotic formulation that predicts a difference of $0.55 * \omega_c$ (cf. (1.15)). Here, $\omega_c(r) \equiv eB(r)/m\gamma(r)$, which is a constant 1.03×10^{10} rad/s for relativistic planar Brillouin flow, and varies by less than 2% over the Brillion hub in the cylindrical base cases.

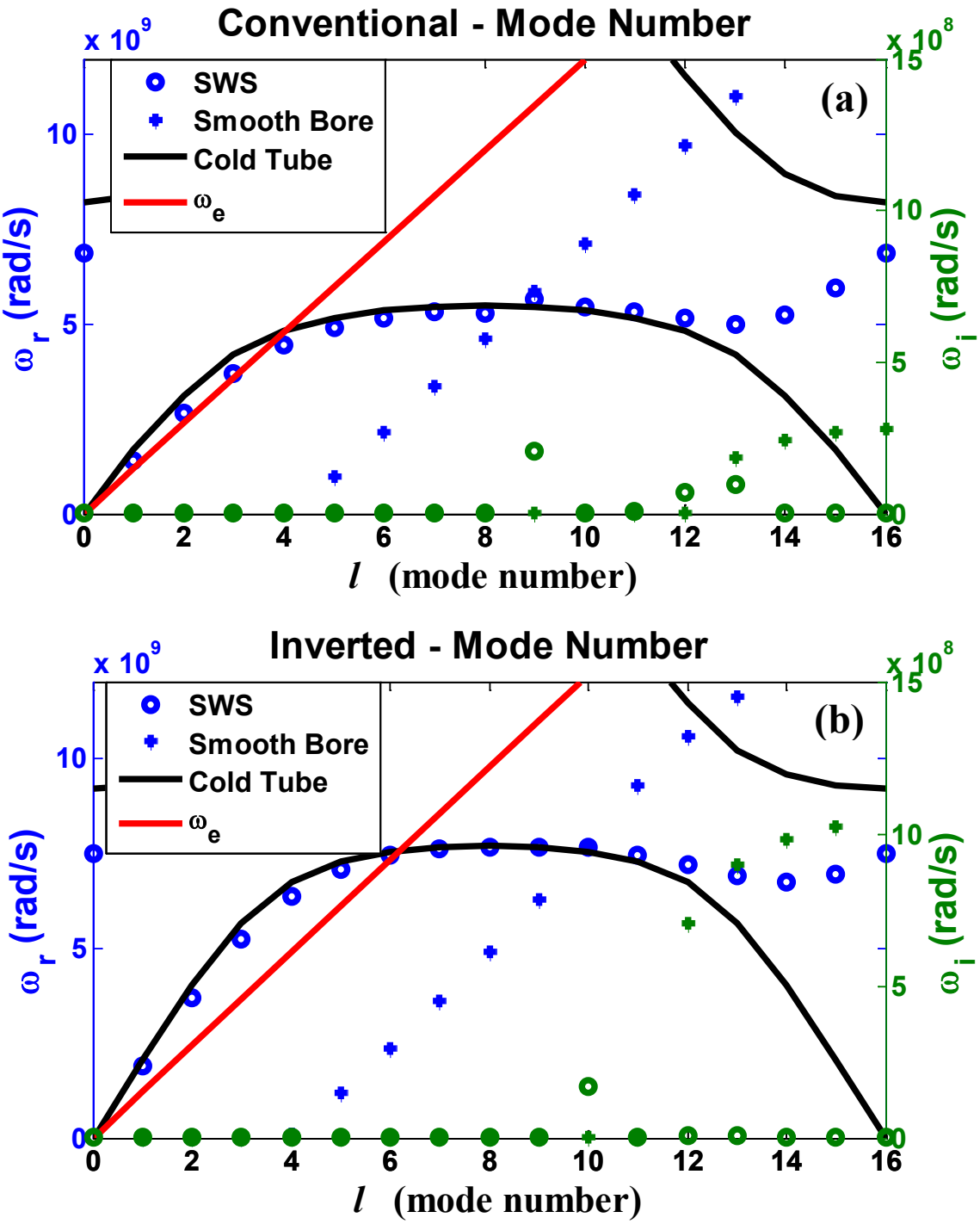

Figure 4.13: Eigenvalue and cold tube solutions, along with the beam line ω_e, for (a) conventional and (b) inverted cylindrical magnetron for ω_r and ω_i as a function of l, with all other parameters equal to the base case. Circular markers correspond to SWS, plus sign markers to smooth-bore.

The conventional magnetron (a), has a few l modes with lower growth rate at the point at which ω_r^{sb} intersects the second frequency band of the cold tube around $l = 12, 13$, although the inverted magnetron (b) shows no such growth at that point. At high mode numbers (l > 11), both magnetrons show a transition in ω_r^{sws} from the first frequency band of the cold tube to the second. This is coincident with the onset of instability in the smooth-bore magnetron, although it does not appear to cause additional instability growth for either SWS magnetron. One possible explanation for this behavior is that if ω_r^{sws} were to follow ω_{ct} in the high mode number region as ω_{ct} returns to 0 ($11 < l \leq 16$), then the synchronous layer would approach the cathode and be shielded from the interaction region by the bulk of the Brillouin flow.

Figure 4.14 is a parameter sweep of magnetic field for the conventional (a) and inverted (b) magnetrons. In both cases, the peak instability occurs very near to the intersection of ω_{ct} and ω_r^{sb} and the Brillouin flow stabilizes if the two frequencies diverge by ~10%. The general behavior follows the three main trends identified for the planar geometry and featured in the analogous planar B field sweep in Figure 4.7. Figure 4.15, which is a sweep over Brillouin hub height r_b, also exhibits these trends. Note that in both Figure 4.15a and Figure 4.15b, moving the horizontal axis from left to right is equivalent to turning up the gap voltage quasi-statically, at the fixed magnetic field.

An examination of the maximum normalized growth rates between the conventional and inverted magnetrons in Figure 4.13 - Figure 4.15 suggests that the conventional magnetron has a slightly higher normalized maximum growth rate (not shown). The values of ω_i^{sws} for the conventional and inverted magnetrons are actually closer than the normalized growth rates. With the data presented here, it is not possible to determine if the inverted SWS magnetrons are inherently more stable than their conventional counterparts. However, it is clear that the negative mass effect, which is held responsible for the peak $\omega_i^{sb}/\omega_r^{sb}$ (green crosses/green circles in Figure 4.13a,b) for the inverted magnetron being over three times larger than the conventional magnetron in Figure 4.13, is not having the same effect in the presence of a SWS.

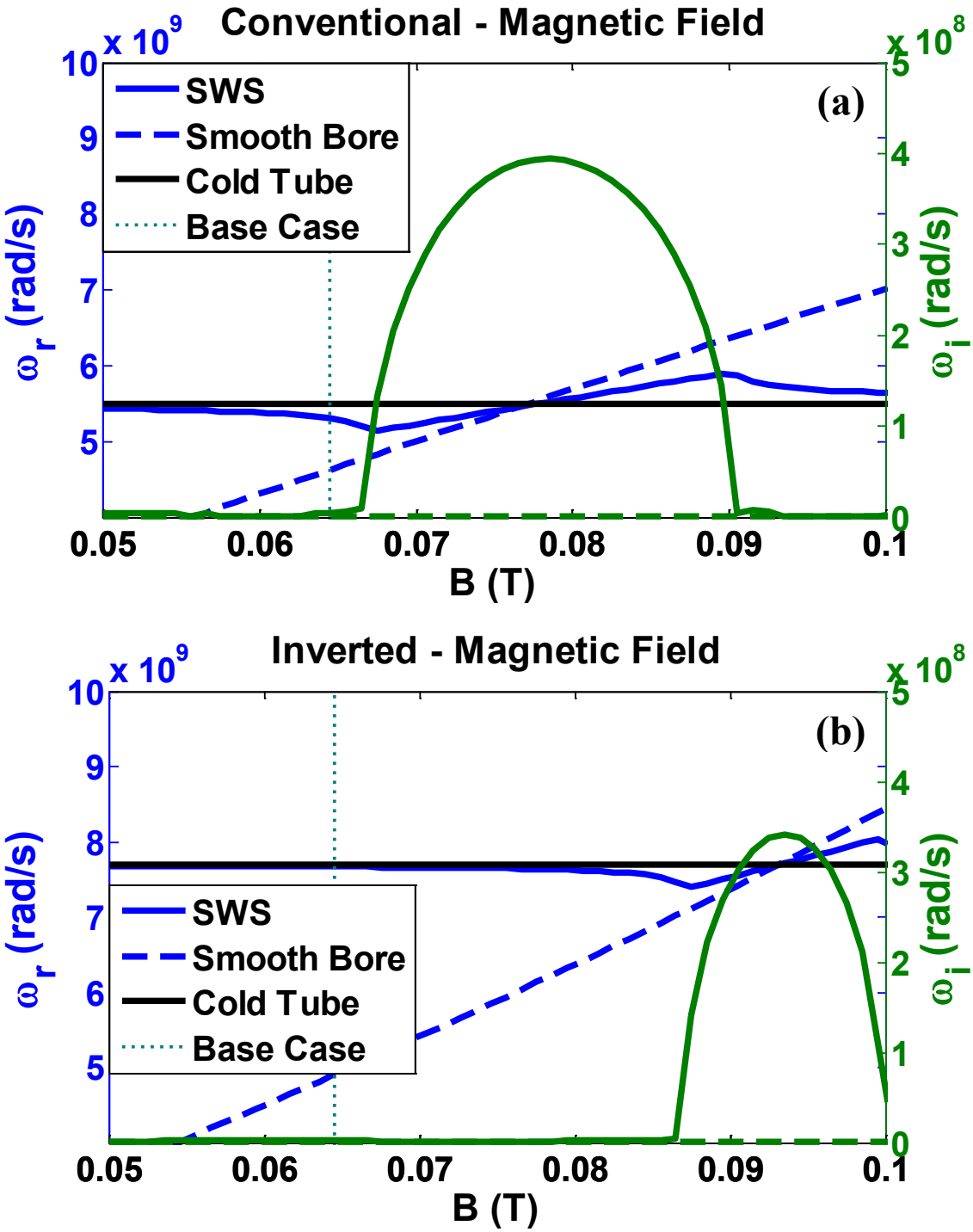

Figure 4.14: Eigenvalue and cold tube solutions for (a) conventional and (b) inverted cylindrical magnetron for ω_r and ω_i as a function of B, adjusting the voltage to keep a constant Brillouin hub height $|r_b - r_c|$, with all other parameters equal to the base case.

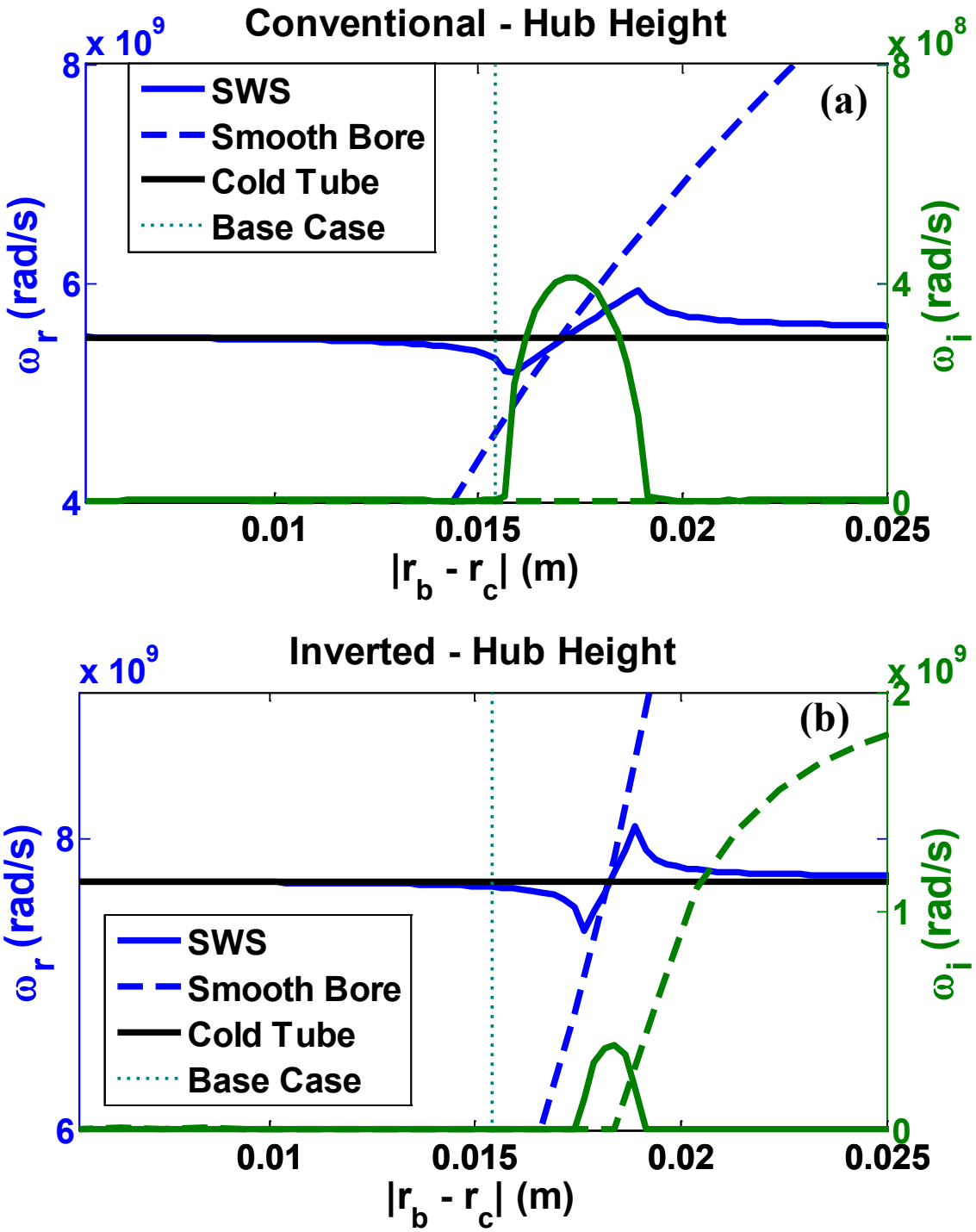

Figure 4.15: Eigenvalue and cold tube solutions for (a) conventional and (b) inverted cylindrical magnetron for ω_r and ω_i as a function of r_b, adjusting the voltage to keep a constant B, with all other parameters equal to the base case.

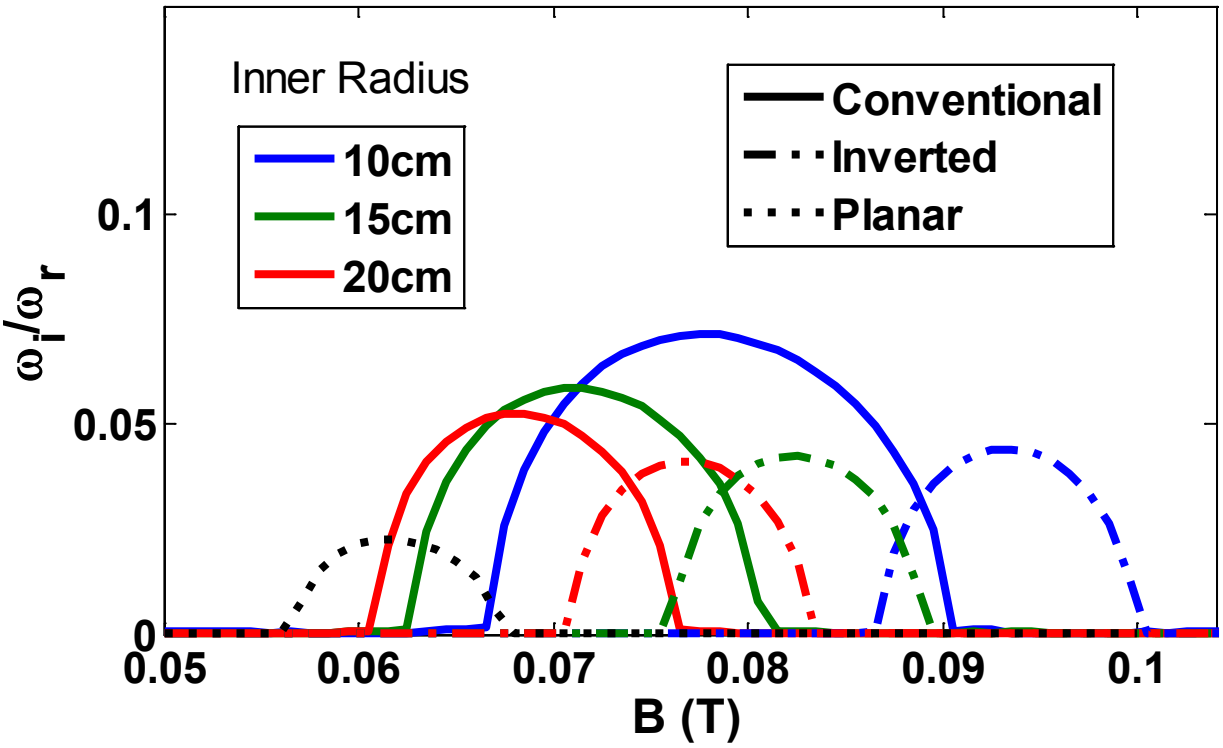

Figure 4.16: Eigenvalue solutions for conventional cylindrical (solid), inverted cylindrical (dash-dot), and planar (dot) cylindrical magnetrons for ω_i/ω_r as a function of B at π-mode, adjusting the voltage to keep a constant $|r_b - r_c|$. The inner and outer radii are changed, keeping the AK gap constant. The number of cavities changes to keep the electron path length per period constant.

Figure 4.16 shows the final sweep of magnetic field for different inner radii of the AK gap. The inner and outer radii of the AK gap (the anode and cathode) are changed in tandem, keeping the AK gap separation constant. The gap voltage is also changed so that the Brillouin hub height $|r_b - r_c|$ is constant. In addition, the number of cavities scales with the inner radius, to keep the electron path length over one period roughly a constant (for $r_{inner} = 10, 15, 20\ cm$, $N = 16, 24, 32$). Both the conventional and inverted magnetrons show a trend toward smaller normalized growth rate peaks at lower magnetic fields as the inner radius is increased. The planar data from Figure 4.7 is included here for comparison. The cylindrical magnetrons show a clear trend toward the planar magnetron as the inner radius increases, bringing the geometry closer to planar.

4.4 Concluding remarks

The governing equations for linearized perturbations on an equilibrium Brillouin flow in a magnetron with a SWS anode are presented here for the first time. Analysis of the planar magnetron shows instability growth is at its strongest when the real part of the frequency of the diocotron instability in the corresponding smooth-bore magnetron and the cold tube resonant frequency of the SWS have almost the same value. The instability vanishes as these two frequencies diverge, which means that the range of instabilities is relatively narrow. At the π-mode, most parameters can only be varied ± 8% from their value at the peak of instability growth before the system stabilizes.

The cylindrical magnetrons are investigated next, and they show the same trends as the planar magnetron, although they exhibit a larger normalized growth rate for similar operational parameters. A comparison between the conventional and inverted cylindrical magnetrons shows that the conventional magnetron has a higher normalized growth rate. In contrast, the negative mass instability that was shown in Chapter 3 led to a significantly larger growth in the inverted geometry, but only for the smooth-bore magnetrons.

It appears that the dynamical behavior, which includes the negative/positive mass effects due to cylindrical geometries, and the intrinsic diocotron effects associated with the shear flow, are strongly affected by the presence of SWS. Smooth-bore magnetrons are unlikely to achieve synchronism because of the constraint of $v(r_c) = 0$. This severely limits the velocity in the $E \times B$ drift.

CHAPTER 5

Summary and Future Work

5.1 Summary

This thesis focuses on the equilibrium and stability of Brillouin flow. The equilibrium governs the operating conditions of magnetron. The stability is related to magnetron startup, and is treated on the same footing for planar, conventional cylindrical, and inverted cylindrical magnetrons, for the first time. Each of these geometries is investigated with both a smooth-bore anode and an anode with a slow-wave structure (SWS). A goal of this investigation is to answer the outstanding question on how, or if, the negative mass instability affects Brillouin flow. The Brillouin flow is the prevalent state in crossed-field devices operating in the space-charge limited regime. Simulations of the inverted Recirculating Planar Magnetron (RPM) did show faster electron bunching in the cylindrical bends compared to the conventional RPM, suggesting the negative mass effect at the circular bend. These circular bends do not have a SWS.

Chapter 2 presents the complete solutions for equilibrium Brillouin flow for conventional and inverted magnetrons and our simulation confirms that the Brillouin flow model describes electron behavior within a magnetron more accurately than the traditional single particle orbit model. Our analytical solutions of the Brillouin flow are given in both non-relativistic and fully relativistic forms for the planar, conventional and inverted cylindrical geometries. For each geometry, a test case was chosen based on experimental configurations that have been analyzed on the Michigan Electron Long Beam Accelerator (MELBA). The velocity, electron density, electric field, and magnetic field profiles were derived from the analytical equations and compared to PIC simulations performed using MAGIC. The analytical results and simulation results show close agreement, supporting the assertion that Brillouin flow more properly represents the equilibrium electron motion in a magnetron than the traditional single particle model.

We discovered that the cylindrical Brillouin flow equations result in two simple relations between the electrostatic scalar potential, magnetic vector potential, and the electron velocity that hold true locally everywhere within the Brillouin flow. These relations have the same form as the global relations, the Hull cutoff and Buneman-Hartree (B-H) conditions that were obtained from the traditional single particle orbit theory [49]. However, for cylindrical magnetrons, our newly discovered B-H condition according to the Brillouin flow model differs from the traditional B-H condition obtained from the single particle model. Our Brillouin B-H condition allows a wider range of magnetic fields and voltages than the single particle B-H for a conventional magnetron [25], but a narrower range for an inverted magnetron as shown in this thesis. These new results help explain the anomalies in both experimental data on MELBA-driven conventional relativistic magnetron, and in the simulation results obtained at Air Force Research Laboratory for the inverted relativistic magnetron. These anomalies could not be explained from the traditional, single particle B-H condition. In contrast, the Hull cutoff condition is identical for both Brillouin flow model and single particle model.

The stability of the Brillouin flow in a smooth-bore magnetron is analyzed in Chapter 3, with a focus on the negative mass instability and its effect on magnetron startup. A perturbation analysis is applied to the equilibrium Brillouin flow profiles from Chapter 2 and the resulting perturbation in the electric field is matched to the field in the vacuum region of the magnetron. The planar geometry, which has been extensively analyzed, has an intrinsic diocotron-like instability. This instability is enhanced in inverted magnetrons and suppressed in conventional magnetrons as the system becomes more cylindrical, consistent with the negative mass effect on a thin beam, which exhibits enhanced bunching in the inverted configuration and de-bunching in the conventional configuration [38], [39]. The behavior of the Brillouin flow in the smooth-bore magnetron is thus consistent with the presence of the negative mass effect.

Smooth-bore magnetron startup is analyzed assuming that voltage across the AK gap is increased slowly that the electrons remain in the Brillouin flow state. Both conventional and inverted cylindrical magnetrons showed modes with high azimuthal mode number (l) start up first. In the conventional magnetron, the high l modes showed the largest normalized (ω_i/ω_r) peak growth rates, but decayed rapidly after the voltage was increased past the peak growth value. The inverted magnetrons showed that low l modes had higher peak normalized growth, but a slower

drop-off of growth rate than the conventional magnetron after the peak growth rate was reached [70].

Fully relativistic and fully electromagnetic formulations are shown to produce equivalent results on stability for low voltage diodes, for which the much simpler nonrelativistic Brillouin flow and electrostatic assumptions were adopted. Increased electron velocities, for relativistic diode voltages, lead to lower normalized growth in the conventional magnetron and higher growth in the inverted magnetron. This behavior is also expected from the negative mass instability, initiating the notion that the Brillouin flow in a smooth-bore magnetron is experiencing the negative mass instability.

Chapter 4 extends the analysis of instabilities to magnetrons with a slow-wave structure (SWS) anode, for the first time. The addition of the SWS necessitates the inclusion of space harmonics in the electromagnetic fields, both in the vacuum region and in the Brillouin flow region. Each of these space harmonics are matched at the vacuum-Brillouin flow interface. For a planar magnetron based on the linear section of the RPM-12a, instabilities occur only in a narrow region for a given mode (as specified by the wavenumber in the direction of the flow) around the wavenumber at which the cold tube frequency and the real part of the eigenfrequency solved for the corresponding smooth-bore anode are close in value. This means that the diocotron-like instability inherent to the planar Brillouin flow, and the synchronous instability created by the interaction of electrons with the SWS must occur simultaneously at nearly the same frequency for the excitation of an instability. That is, the SWS substantially restricts the range of wavenumber for instability growth that is found for smooth-bore planar magnetron.

The cylindrical base cases for the conventional and inverted magnetrons were chosen to keep many parameters equal to the planar geometry to facilitate comparison. As with the planar magnetron with the SWS anode, the cylindrical SWS magnetrons show growth only when the smooth-bore hot tube eigenfrequency and the SWS cold tube frequency are similar. Increasing the anode and cathode radii while keeping the AK gap constant (as was done in Chapter 3) causes the eigenvalue solutions for both the conventional and inverted magnetrons to approach the planar solutions. Unlike the smooth-bore anode, the conventional magnetron has higher normalized growth than the inverted magnetron. The addition of a SWS to the anode appears to reduce the negative mass instability for the inverted magnetron, as the growth rates for the conventional magnetron appear larger than those of the inverted magnetron. The underlying reason is unknown

as of this writing. However, this finding does not contradict early simulations of the recirculating planar magnetron that showed enhanced bunching in the cylindrical bends of the inverted magnetron configuration because the circular bends did not have a SWS, and therefore enhanced bunching due to the negative mass effect was observed.

5.2 Suggested Future Work

While this thesis provides a comprehensive stability analysis of the Brillouin flow in the planar magnetron with a SWS, the vast parameter space for both the cylindrical conventional and cylindrical inverted magnetron with a SWS has prevented a similarly detailed study. This is compounded by the negative mass effect which naturally occurs in the cylindrical geometry, as convincingly shown in this study of the smooth-bore magnetron. But this negative mass effect seems to be diminished in a cylindrical magnetron with a slow-wave structure in the limited study of this thesis. Our study of the cylindrical magnetrons seemed to suggest that the resonance introduced by the SWS is more important than the intrinsic negative mass effect, in sharp contrast to the cylindrical smooth-bore magnetron. Whether this seemingly important observation is valid in general needs to be studied. It is tantalizing to recall that the conventional magnetron with SWS do have a fast startup despite its intrinsic positive mass behavior of the electrons. Perhaps PIC simulations of the configurations examined in this thesis would shed light on this issue. It should be mentioned, however, that it is not easy to extract small signal growth rates from PIC simulations of the Brillouin flow because there is overmoding and nonlinear behavior of SWS magnetrons, compounded by electrons generated and removed in the code, making growth of density perturbations in a single mode uncertain.

Another possible future study concerns dual-frequency operation of the recirculating planar magnetron, which has a SWS for one frequency on one planar section, and one for twice that frequency on the other. These planar sections are joint by an annular smooth-bore drift tube. Harmonic generation, together with the stability analysis of both planar sections, are of interest.

To increase the coupling between the two planar sections of the Recirculating Planar Magnetron, the cathode between the two sections may be segmented to allow electromagnetic coupling between the two sections. These segmented cathodes are called mode controlled cathodes and have been successfully adopted in experiments [76]. Its stability analysis will probably defy

analytic formulation, but the cold tube dispersion relation may still be obtained and would be useful in a design study.

APPENDIX

Derivation of Non-Relativistic Cylindrical Brillouin Flow Profiles

Equations (2.11) through (2.13) give the electron velocity $v_\theta(r)$, electric field $E_0(r)$, and plasma frequency $\omega_p^2(r)$. Equation (2.14) gives the Brillouin hub height in terms of the AK gap voltage V and the magnetic field B_0. This Appendix will derive the equations for conventional magnetrons, although the final results will also be applicable to inverted magnetrons. Davidson's book [26] has a derivation for the conventional geometry, which produces identical results if the inner radius "a" is replaced by the general cathode radius r_c.

The Brillouin flow is space-charge limited, so the electric field on the cathode is zero,

$$E_0(r_c) = 0. \tag{A.1}$$

The electrons are assumed to have been emitted with no velocity, so

$$v_\theta(r_c) = 0. \tag{A.2}$$

Under the assumption that all electrons in the Brillouin flow have zero total energy, we have

$$\frac{1}{2}mv_\theta^2(r) - e\phi(r) = 0, \tag{A.3}$$

where $\phi(r)$ is the electrostatic potential, which is also zero at the cathode. The derivative of Eq. (A.3) with respect to *r* gives

$$mv_\theta(r)\frac{\partial v_\theta(r)}{\partial r} + eE_0(r) = 0. \tag{A.4}$$

The force balance equation ($\vec{B}_0 = -\hat{z}B_0$ is in the negative $\hat{z}$ direction),

$$\frac{mv_\theta^2(r)}{r} = e[E_0(r) + v_\theta(r)B_0] \tag{A.5}$$

can be solved for electric field, which is used in (A.4) to obtain the differential equation

$$\frac{\partial v_\theta(r)}{\partial r} = -\frac{v_\theta(r)}{r} + \omega_c, \tag{A.6}$$

where $\omega_c = eB_0/m$ $(e, B_0 > 0)$. The solution to this equation is

$$v_\theta(r) = \frac{C_1}{r} + \frac{\omega_c r}{2}, \tag{A.7}$$

where C_1 is solved for using Eq. (A.2) to find $C_1 = -\omega_c r_c^2/2$. The velocity as a function of radius is obtained:

$$v_\theta(r) = \frac{1}{2}\omega_c \frac{r^2 - r_c^2}{r}. \tag{A.8}$$

A substitution of Eq. (A.8) and its derivative into Eq. (A.4) results in

$$E_0(r) = -B_0\omega_c \frac{r^4 - r_c^4}{4r^3}. \tag{A.9}$$

Poisson's equation directly relates the electron density to the derivative of the electric field,

$$\frac{1}{r}\frac{\partial}{\partial r}\big(rE_0(r)\big) = -\frac{en_0(r)}{\epsilon_0}, \tag{A.10}$$

where $n_0(r)$ is the electron density. Using the derivative of Eq. (A.9) in Eq. (A.10) results in an equation for $\omega_p^2(r) \equiv e^2 n_0(r)/\epsilon_0 m$:

$$\omega_p^2(r) = \omega_c^2\left[1 - \frac{1}{2}\frac{r^4 - r_c^4}{r^4}\right]. \tag{A.11}$$

Finally, the voltage drop across the AK gap can be found by examining the voltage drop over the Brillouin hub and the voltage drop over the vacuum region. The voltage drop over the Brillouin hub is obtained by integrating the electric field, Eq. (A.9), over the hub,

$$\phi(r) = \frac{1}{2}B_0\omega_c\left(\frac{r^2 - r_c^2}{2r}\right)^2, \qquad |r_b - r_c| \geq |r - r_c|. \tag{A.12}$$

The voltage drop over the vacuum region can be found from Poisson's equation, $\nabla^2\phi(r) = 0$, using the continuity of $\phi(r)$ and $\partial\phi(r)/\partial r$ at r_b from Eq. (A.12) and its derivative,

$$\phi(r) = \frac{1}{2}B_0\omega_c\left[\left(\frac{r_b^2 - r_c^2}{2r_b}\right)^2 + \frac{1}{2}\frac{r_b^4 - r_c^4}{r_b^2}\ln\frac{r}{r_b}\right], \qquad |r_b - r_c| \leq |r - r_c|. \tag{A.13}$$

The overall voltage drop at the anode is:

$$\phi(r_a) = V = \frac{1}{2}B_0\omega_c\left[\left(\frac{r_b^2 - r_c^2}{2r_b}\right)^2 + \frac{1}{2}\frac{r_b^4 - r_c^4}{r_b^2}\ln\frac{r_a}{r_b}\right]. \tag{A.14}$$

In terms of the voltage V, magnetic field B, cathode radius r_c, and anode radius r_a, the Brillouin hub radius r_b needs to be solved numerically from Eq. (A.14). Equations (A.8), (A.9), (A.11), , and (A.14) are, respectively, Equations (2.11), (2.12), (2.13), and (2.14) of the main text.

BIBLIOGRAPHY

[1] IEEE-Rutgers Center for the History of Electrical Engineering, *Tracking the History of Radar*. Piscataway, NJ: Institute of Electrical Engineers, 1994.

[2] H. A. H. Boot and J. T. Randall, "Historical notes on the cavity magnetron," *IEEE Trans. Electron Devices*, vol. 23, no. 7, pp. 724–729, Jul. 1976.

[3] K. Posthumus, "Magnetron Oscillations of a New Type," *Nature*, vol. 134, p. 179, Aug. 1934.

[4] E. C. S. Megaw, "Magnetron Oscillations," *Nature*, vol. 134, pp. 324–325, Sep. 1934.

[5] Y. Y. Lau, "Theory of Crossed-Field Devices and a Comparative Study of Other Radiation Sources," in *High-power Microwave Sources*, V. L. Granatstein and I. Alexeff, Eds. Norwood, MA: Artech House, 1987, pp. 309–351.

[6] J. E. Brittain, "The Magnetron and the Beginnings of the Microwave Age," *Phys. Today*, vol. 38, no. 7, pp. 60–67, Jan. 2008.

[7] A. S. Gilmour, *Klystrons, Traveling Wave Tubes, Magnetrons, Crossed-Field Amplifiers, and Gyrotrons*. Artech House, 2011.

[8] G. B. Collins, *Microwave magnetrons*. New York; Toronto; London: McGraw-Hill, 1948.

[9] V. B. Neculaes, M. C. Jones, R. M. Gilgenbach, Y. Y. Lau, J. W. Luginsland, B. W. Hoff, W. M. White, N. M. Jordan, P. Pengvanich, Y. Hidaka, and H. L. Bosman, "Magnetic priming effects on noise, startup, and mode competition in magnetrons," *IEEE Trans. Plasma Sci.*, vol. 33, no. 1, pp. 94–102, Feb. 2005.

[10] R. M. Gilgenbach, Y. Y. Lau, H. McDowell, K. L. Cartwright, and T. A. Spencer, "Crossed-Field Devices," in *Modern Microwave and Millimeter-Wave Power Electronics*, R. J. Barker, J. H. Booske, N. C. Luhmann Jr., and G. S. Nusinovich, Eds. Hoboken, N.J: Wiley-IEEE Press, 2005, Chapter 6.

[11] R. M. Gilgenbach, Y. Y. Lau, D. M. French, B. W. Hoff, J. Luginsland, and M. Franzi, "Crossed field device," US patent No. US8841867 B2, 23-Sep-2014.

[12] R. M. Gilgenbach, Y. Y. Lau, D. M. French, B. W. Hoff, M. Franzi, and J. Luginsland, "Recirculating Planar Magnetrons for High-Power High-Frequency Radiation Generation," *IEEE Trans. Plasma Sci.*, vol. 39, no. 4, pp. 980–987, Apr. 2011.

[13] M. A. Franzi, R. M. Gilgenbach, B. W. Hoff, D. A. Chalenski, D. Simon, Y. Y. Lau, and J. Luginsland, "Recirculating-Planar-Magnetron Simulations and Experiment," *IEEE Trans. Plasma Sci.*, vol. 41, no. 4, pp. 639–645, Apr. 2013.

[14] M. A. Franzi, G. B. Greening, N. M. Jordan, R. M. Gilgenbach, D. H. Simon, Y. Y. Lau, B. W. Hoff, and J. Luginsland, "Microwave Power and Phase Measurements on a Recirculating Planar Magnetron," *IEEE Trans. Plasma Sci.*, vol. 43, no. 5, pp. 1675–1682, May 2015.

[15] G. Greening, M. Franzi, R. Gilgenbach, Y. Y. Lau, and N. Jordan, "Multi-Frequency Recirculating Planar Magnetrons," in *Vacuum Electronics Conference, IEEE International*, 2014, pp. 407–408.

[16] G. B. Greening, N. M. Jordan, S. C. Exelby, R. M. Gilgenbach, D. Simon, and Y. Y. Lau, "Experimental microwave power extraction in the Multi-Frequency Recirculating Planar Magnetron," in *Vacuum Electronics Conference (IVEC), 2015 IEEE International*, 2015, pp. 1–2.

[17] J. C. Slater, *Microwave Electronics*. Princeton, NJ: Van Nostrand, 1950.

[18] P. J. Christenson, D. P. Chernin, A. L. Garner, and Y. Y. Lau, "Resistive destabilization of cycloidal electron flow and universality of (near-) Brillouin flow in a crossed-field gap," *Phys. Plasmas*, vol. 3, no. 12, pp. 4455–4462, Dec. 1996.

[19] A. Palevsky, "Generation of intense microwave radiation by the relativistic e-beam magnetron (experiment and numerical simulation)," Ph.D. Thesis, Massachusetts Institute of Technology, 1980.

[20] A. Palevsky, G. Bekefi, and A. T. Drobot, "Numerical simulation of oscillating magnetrons," *J. Appl. Phys.*, vol. 52, no. 8, pp. 4938–4941, Aug. 1981.

[21] P. J. Christenson, "Equilibrium, Stability, and Turbulence in Cycloidal Electron Flows in Crossed Electric and Magnetic Fields," Doctoral Dissertation, The University of Michigan, Ann Arbor, 1996.

[22] P. J. Christenson and Y. Y. Lau, "One-Dimensional Modulational Instability in a Crossed-Field Gap," *Phys. Rev. Lett.*, vol. 76, no. 18, pp. 3324–3327, Apr. 1996.

[23] A. W. Hull, "The Effect of A Uniform Magnetic Field on the Motion of Electrons Between Coaxial Cylinders.," *Phys. Rev.*, vol. 18, no. 1, pp. 31–57, Jul. 1921.

[24] R. V. Lovelace and T. F. T. Young, "Relativistic Hartree condition for magnetrons: Theory and comparison with experiments," *Phys. Fluids*, vol. 28, no. 8, pp. 2450–2452, Aug. 1985.

[25] Y. Y. Lau, J. W. Luginsland, K. L. Cartwright, D. H. Simon, W. Tang, B. W. Hoff, and R. M. Gilgenbach, "A re-examination of the Buneman–Hartree condition in a cylindrical smooth-bore relativistic magnetron," *Phys. Plasmas*, vol. 17, no. 3, p. 33102, 2010.

[26] R. C. Davidson, *Physics of Nonneutral Plasmas*. Imperial College Press, 2001.

[27] G. G. MacFarlane and H. G. Hay, “Wave Propagation in a Slipping Stream of Electrons: Small Amplitude Theory,” *Proc. Phys. Soc. Sect. B*, vol. 63, no. 6, p. 409, 1950.

[28] O. Buneman, “Ribbon Beams,” *J. Electron. Control*, vol. 3, no. 5, pp. 507–509, Nov. 1957.

[29] C. Nielsen, A. Sessler, and K. Symon, “Longitudinal instabilities in intense relativistic beams,” *Proc Int Conf High-Energy Accel. Instrum.*, 1959.

[30] A. A. Kolomenskii and A. N. Lebedev, *Proc Int Conf High-Energy Accel. Instrum.*, p. 115, 1959.

[31] Y. Y. Lau, “A Unified Theory of the Diocotron, Cyclotron Maser, and Negative-Mass Instabilities,” *IEEE Trans. Electron Devices*, vol. 31, no. 3, pp. 329–337, 1984.

[32] R. C. Davidson, K. Tsang, and J. A. Swegle, “Macroscopic extraordinary-mode stability properties of relativistic non-neutral electron flow in a planar diode with applied magnetic field,” *Phys. Fluids*, vol. 27, no. 9, pp. 2332–2345, Sep. 1984.

[33] P. G. Drazin and L. N. Howard, “Hydrodynamic Stability of Parallel Flow of Inviscid Fluid,” *Adv. Appl. Mech.*, vol. 9, p. 1, 1966.

[34] O. Buneman, R. Levy, and L. Linson, “Stability of Crossed-Field Electron Beams,” *J. Appl. Phys.*, vol. 37, no. 8, p. 3203-, 1966.

[35] T. M. Antonsen Jr, E. Ott, C. L. Chang, and A. T. Drobot, “Parametric scaling of the stability of relativistic laminar flow magnetic insulation,” *Phys. Fluids*, vol. 28, no. 9, pp. 2878–2881, Sep. 1985.

[36] J. C. Maxwell, “Abstract of Professor Maxwell’s paper on the Stability of Saturn’s Rings,” *Mon. Not. R. Astron. Soc.*, vol. 19, pp. 297–304, Jun. 1859.

[37] R. Fedele, “From Maxwell’s theory of Saturn’s rings to the negative mass instability,” *Philos. Trans. R. Soc. Lond. Math. Phys. Eng. Sci.*, vol. 366, no. 1871, pp. 1717–1733, May 2008.

[38] D. Chernin and Y. Y. Lau, “Stability of laminar electron layers,” *Phys. Fluids*, vol. 27, no. 9, pp. 2319–2331, Sep. 1984.

[39] D. M. French, B. W. Hoff, Y. Y. Lau, and R. M. Gilgenbach, “Negative, positive, and infinite mass properties of a rotating electron beam,” *Appl. Phys. Lett.*, vol. 97, no. 11, pp. 111501-111501–3, Sep. 2010.

[40] Y. Y. Lau and R. J. Briggs, “Effects of Cold Plasma on the Negative Mass Instability of a Relativistic Electron Layer,” *Phys. Fluids*, vol. 14, no. 5, pp. 967–976, May 1971.

[41] Y. Y. Lau and D. Chernin, “Stabilization of the Negative Mass Instability in a Rotating Relativistic Electron Beam,” *Phys. Rev. Lett.*, vol. 52, no. 16, pp. 1425–1428, Apr. 1984.

[42] R. C. Davidson, K. T. Tsang, and H. S. Uhm, "Stabilization of diocotron instability by relativistic and electromagnetic effects for intense nonneutral electron flow," *Phys. Lett. A*, vol. 125, no. 1, pp. 61–67, Oct. 1987.

[43] R. C. Davidson, K. T. Tsang, and H. S. Uhm, "Diocotron instability for intense relativistic non-neutral electron flow in planar diode geometry," *Phys. Fluids*, vol. 31, no. 6, pp. 1727–1737, Jun. 1988.

[44] L. Brillouin, "Theory of the Magnetron. I," *Phys. Rev.*, vol. 60, no. 5, pp. 385–396, Sep. 1941.

[45] L. Brillouin, "Theory of the Magnetron. III," *Phys. Rev.*, vol. 63, no. 3–4, pp. 127–136, Feb. 1943.

[46] A. L. Garner, Y. Y. Lau, and D. Chernin, "Collapse of cycloidal electron flows induced by misalignments in a magnetically insulated diode," *Phys. Plasmas*, vol. 5, no. 6, pp. 2447–2453, Jun. 1998.

[47] S. H. Gold and G. S. Nusinovich, "Review of high-power microwave source research," *Rev. Sci. Instrum.*, vol. 68, no. 11, pp. 3945–3974, Nov. 1997.

[48] J. Benford, J. A. Swegle, and E. Schamiloglu, *High Power Microwaves, Third Edition*. Boca Raton, FL: CRC Press, 2015.

[49] D. H. Simon, Y. Y. Lau, J. W. Luginsland, and R. M. Gilgenbach, "An unnoticed property of the cylindrical relativistic Brillouin flow," *Phys. Plasmas*, vol. 19, no. 4, pp. 43103-43103–5, Apr. 2012.

[50] R. C. Davidson, G. L. Johnston, K. T. Tsang, and A. T. Drobot, "Cylindrical Brillouin flow in relativistic smooth-bore magnetrons," in *Proc. SPIE*, 1989, vol. 1061, pp. 186–200.

[51] T. M. Antonsen and E. Ott, "Theory of intense ion beam acceleration," *Phys. Fluids*, vol. 19, no. 1, pp. 52–59, Jan. 1976.

[52] M. R. Lopez, R. M. Gilgenbach, D. W. Jordan, S. A. Anderson, M. D. Johnston, M. W. Keyser, H. Miyake, C. W. Peters, M. C. Jones, V. Bogdan Neculaes, Y. Y. Lau, T. A. Spencer, J. W. Luginsland, M. D. Haworth, R. W. Lemke, and D. Price, "Cathode effects on a relativistic magnetron driven by a microsecond e-beam accelerator," *IEEE Trans. Plasma Sci.*, vol. 30, no. 3, pp. 947–955, Jun. 2002.

[53] M. R. Lopez, R. M. Gilgenbach, M. C. Jones, W. M. White, D. W. Jordan, M. D. Johnston, T. S. Strickler, V. Bogdan Neculaes, Y. Y. Lau, T. A. Spencer, M. D. Haworth, K. L. Cartwright, P. J. Mardahl, J. W. Luginsland, and D. Price, "Relativistic magnetron driven by a microsecond E-beam accelerator with a ceramic insulator," *IEEE Trans. Plasma Sci.*, vol. 32, no. 3, pp. 1171–1180, Jun. 2004.

[54] B. W. Hoff, "Magnetic Priming of a Relativistic Magnetron," Doctoral Dissertation, The University of Michigan, Ann Arbor, 2009.

[55] B. Goplen, L. Ludeking, D. Smith, and G. Warren, "User-configurable MAGIC for electromagnetic PIC calculations," *Comput. Phys. Commun.*, vol. 87, no. 1–2, pp. 54–86, May 1995.

[56] T. P. Fleming, M. R. Lambrecht, and K. L. Cartwright, "Numerical Simulations of a Relativistic Inverted Magnetron," *IEEE Trans. Plasma Sci.*, vol. 38, no. 7, pp. 1563–1573, Jul. 2010.

[57] M. Lopez, Y. Y. Lau, J. W. Luginsland, D. W. Jordan, and R. M. Gilgenbach, "Limiting current in a relativistic diode under the condition of magnetic insulation," *Phys. Plasmas*, vol. 10, no. 11, pp. 4489–4493, Nov. 2003.

[58] O. Buneman, in *Crossed-field microwave devices*, E. C. Okress, Ed. New York: Academic Press, 1961.

[59] A. H. Falkner, "Double-stream flow in the smooth-bore magnetron," *Proc. Inst. Electr. Eng.*, vol. 120, no. 9, pp. 959–961, Sep. 1973.

[60] H. L. McDowell, "Smooth-bore magnetron simulations using a moving wavelength computer code," *IEEE Trans. Plasma Sci.*, vol. 30, no. 3, pp. 980–983, Jun. 2002.

[61] K. D. Bergeron, "One- and two-species equilibria for magnetic insulation in coaxial geometry," *Phys. Fluids*, vol. 20, no. 4, pp. 688–697, Apr. 1977.

[62] Y. Y. Lau, J. W. Luginsland, K. L. Cartwright, and M. D. Haworth, "Role of Ions in a Crossed-Field Diode," *Phys. Rev. Lett.*, vol. 98, no. 1, p. 15002, Jan. 2007.

[63] J. F. Hull, "Inverted Magnetron," *Proc. IRE*, vol. 40, no. 9, pp. 1038–1041, Sep. 1952.

[64] J. Swegle and E. Ott, "Instability of the Brillouin-Flow Equilibrium in Magnetically Insulated Structures," *Phys. Rev. Lett.*, vol. 46, no. 14, pp. 929–932, Apr. 1981.

[65] R. Davidson, H.-W. Chan, C. Chen, and S. Lund, "Equilibrium and stability properties of intense non-neutral electron flow," *Rev. Mod. Phys.*, vol. 63, no. 2, pp. 341–374, Apr. 1991.

[66] R. C. Davidson and K. T. Tsang, "Analysis of magnetron instability for relativistic nonneutral electron flow in cylindrical high-voltage diodes," *Laser Part. Beams*, vol. 6, no. 4, pp. 661–685, Nov. 1988.

[67] K. T. Tsang and R. C. Davidson, "Macroscopic cold-fluid equilibrium properties of relativistic non-neutral electron flow in a cylindrical diode," *Phys. Rev. A*, vol. 33, no. 6, pp. 4284–4292, Jun. 1986.

[68] T. J. Orzechowski and G. Bekefi, "Microwave emission from pulsed, relativistic e-beam diodes. I. The smooth-bore magnetron," *Phys. Fluids*, vol. 22, no. 5, p. 978, 1979.

[69] H. Nyquist, "Regeneration Theory," *Bell Syst. Tech. J.*, vol. 11, no. 1, pp. 126–147, Jan. 1932.

[70] D. H. Simon, Y. Y. Lau, G. Greening, P. Wong, B. W. Hoff, and R. M. Gilgenbach, "Stability of Brillouin flow in planar, conventional, and inverted magnetrons," *Phys. Plasmas*, vol. 22, no. 8, p. 82104, Aug. 2015.

[71] D. J. Kaup, "Theoretical modeling of an A6 relativistic magnetron," *Phys. Plasmas*, vol. 11, no. 6, pp. 3151–3164, Jun. 2004.

[72] J. W. Gewartowski and H. A. Watson, *Principles of electron tubes: including grid-controlled tubes, microwave tubes, and gas tubes*. Princeton, NJ: Van Nostrand, 1965.

[73] N. M. Kroll and W. E. L. Jr, "The Resonant Modes of the Rising Sun and Other Unstrapped Magnetron Anode Blocks," *J. Appl. Phys.*, vol. 19, no. 2, pp. 166–186, Feb. 1948.

[74] Y. Y. Lau and D. Chernin, "A review of the ac space-charge effect in electron–circuit interactions," *Phys. Fluids B Plasma Phys. 1989-1993*, vol. 4, no. 11, pp. 3473–3497, Nov. 1992.

[75] Y. Lau and L. Barnett, "A Low Magnetic-Field Gyrotron Gyro-Magnetron," *Int. J. Electron.*, vol. 53, no. 6, pp. 693–698, 1982.

[76] M. Franzi, R. Gilgenbach, Y. Y. Lau, B. Hoff, G. Greening, and P. Zhang, "Passive mode control in the recirculating planar magnetron," *Phys. Plasmas*, vol. 20, no. 3, p. 33108, Mar. 2013.